

Master's Thesis

Enhancing the signal-to-background ratio in the $t\bar{t}H$ channel through top quark spin correlations

Verbesserung des Signal-zu-Untergrund-Verhältnisses im $t\bar{t}H$ -Kanal durch Ausnutzung von Top-Quark-Spin-Korrelationen

prepared by

Paul Konstantin Krug

from Göttingen

at the II. Institute of Physics Göttingen

Thesis number: II.Physik-UniGö-MSc-2018/06

Working period: 16th April 2018 until 5th November 2018

Supervisor: Prof. Dr. Arnulf Quadt

Second referee: Prof. Dr. Stan Lai

Abstract

In this analysis, the effects of top quark spin correlations in $t\bar{t}$ production with an associated Higgs boson decaying into a $b\bar{b}$ pair are studied at a centre-of-mass energy of 13 TeV at the LHC with the ATLAS experiment. It is shown that one can construct observables from top or anti-top quark and/or Higgs boson decay products that are not only sensitive to $t\bar{t}$ spin polarisation effects, but also help to separate between the $t\bar{t}(H \rightarrow b\bar{b})$ signal and the irreducible $t\bar{t} + b\bar{b}$ background. Results are shown for the semi- and dileptonic final states, using Monte Carlo simulations. The most sensitive angular observables were used to improve existing multivariate techniques of the ATLAS $t\bar{t}(H \rightarrow b\bar{b})$ search.

Furthermore, it is shown that top quark spin analysers are sensitive to new physics scenarios, such as a $t\bar{t}H$ Yukawa coupling with a CP-odd component. Various angular observables were studied with regards to different Higgs boson CP scenarios and the most sensitive observables were joined as input variables into a multivariate algorithm that can be used to differentiate between the respective Higgs boson CP hypotheses.

Keywords: Top Quark, Higgs Boson, Angular Distributions, CP-Violation.

Zusammenfassung

In dieser Analyse werden die Auswirkungen von Top-Quark-Spin-Korrelationen auf die $t\bar{t}$ -Produktion in Assoziation mit einem Higgs-Boson und entsprechende Untergrundprozesse bei einer Schwerpunktsenergie von 13 TeV am LHC mit dem ATLAS-Experiment untersucht. Es wird gezeigt, dass sich Observablen finden lassen, die sich nicht nur sensitiv auf $t\bar{t}$ -Spinpolarisationseffekte verhalten, sondern auch bei der Trennung des $t\bar{t}(H \rightarrow b\bar{b})$ -Signals von dem irreduziblen $t\bar{t} + b\bar{b}$ -Untergrund helfen können. Ergebnisse der Analysen von Monte-Carlo-Simulationen für den semi- und dileptonischen Kanal werden präsentiert. Die sensitivsten Winkelverteilungen wurden genutzt um bestehende multivariate Analysemethoden der ATLAS $t\bar{t}(H \rightarrow b\bar{b})$ Suche zu verbessern.

Des Weiteren wird gezeigt, dass Variablen im Zusammenhang mit Top-Quark-Spin-Korrelationen hilfreich sind um Szenarien neuer Physik, wie etwa eine $t\bar{t}H$ -Yukawa-Kopplung mit CP-ungerader Komponente, zu untersuchen. In diesem Sinne wurden zahlreiche Winkelverteilungen studiert und die sensitivsten Variablen wurden in einen multivariaten Algorithmus integriert, welcher die Unterscheidung zwischen verschiedenen Higgs-Boson-CP-Hypothesen erlaubt.

Stichwörter: Top-Quark, Higgs-Boson, Winkelverteilungen, CP-Verletzung.

Contents

1. Preface	1
2. The Standard Model of Particle Physics	5
2.1. Elementary Particles of the Standard Model	6
2.2. Electroweak Symmetry Breaking and the Higgs Mechanism	10
2.3. The Top Quark	15
2.4. Top Quark Spin Correlations	19
2.5. Limits of the Standard Model	23
3. The Experimental Setup	27
3.1. The Large Hadron Collider	27
3.2. The ATLAS Detector	30
4. The $t\bar{t}H$ Process and the ATLAS $t\bar{t}(H \rightarrow b\bar{b})$ Search	35
4.1. The $t\bar{t}H$ Process and the $t\bar{t}(H \rightarrow b\bar{b})$ Process	35
4.2. Object Reconstruction	36
4.2.1. Leptons	36
4.2.2. Jets	38
4.2.3. Missing Transverse Energy	39
4.3. Monte Carlo Modelling	40
4.3.1. Signal	40
4.3.2. The $t\bar{t}$ Backgrounds	41
4.3.3. Other Backgrounds	42
4.4. Event Selection	42
4.4.1. Event Categorisation	43
4.5. Event Reconstruction	49
4.5.1. Reconstruction BDT	49
4.5.2. Likelihood Discriminant	51
4.5.3. Matrix Element Discriminant	51
4.6. Multivariate Event Classification	52

5. Analysis of Angular Distributions in the $t\bar{t}(H \rightarrow b\bar{b})$ Channel	53
5.1. Single Lepton Channel	55
5.1.1. Generator Level and Reconstruction Level Studies	58
5.1.2. Boosted Events	65
5.1.3. Multivariate Techniques on Reconstruction Level	65
5.1.4. Optimised Classification BDT	69
5.1.5. Modelling Uncertainties	71
5.2. Dilepton Channel	72
5.2.1. Generator Level Studies	74
5.2.2. Reconstruction Level Studies	76
5.2.3. Multivariate Techniques on Reconstruction Level	79
5.2.4. Optimised Classification BDT	82
6. The $t\bar{t}(H \rightarrow b\bar{b})$ Process with Modified CP-Odd and CP-Mixed $t\bar{t}H$ Yukawa Couplings	85
6.1. Bias towards Standard Model Expectation	86
6.1.1. Classification BDT	86
6.1.2. Reconstruction BDT	87
6.2. Determination of the Higgs Boson CP Quantum Number in $t\bar{t}H$ Interactions	89
6.2.1. CP Determination BDT	91
7. Results and Outlook	93
A. Appendix	95
A.1. Input Variables to the Reconstruction BDTs	96
A.2. Input Variables to the Classification BDTs	97
A.3. Input Variables to the Optimised BDTs	99
A.4. Input Variables to the CP Determination BDTs	103

1. Preface

Fire, air, water and earth. Four elements, that would describe the composition of the universe according to the *Classical-Element-Theory* established by the Greek philosopher EMPEDOCLES around 450 B.C., almost 2500 years ago. Nowadays the majority of scientists feel very certain about this theory being unable to describe nature. In the course of time, the corresponding aspects of metaphysics slowly turned into the science of particle physics. However, its original aspiration remains: satisfying the strong human desire of understanding the universe by its fundamental constituents and laws, manifested in a *theory of everything* (ToE). Although the works of EMPEDOCLES and other antique philosophers can be counted as first attempts to describe nature by elementary structures, only the beginning of the 19th century saw growing evidence for the real existence of atoms. For a long time atoms were believed to be the smallest, indivisible particles. However, subatomic structures became recognised in the end of the 19th century, which culminated in the discovery of the electron by EMIL WIECHERT and JOSEPH JOHN THOMSON and the first observation of radioactivity by ANTOINE HENRI BECQUEREL. The early 20th century saw the development of quantum mechanics, which gave rise to numerous different atomic models. All of these suffered either from theoretical problems or from lacking ability to describe recent observations. Finally, the *theory of atomic orbitals* was set up during the 1920s, providing the first satisfying description of atoms and molecules. As a consequence of the research on nuclear physics, a deeper understanding of nature was gained within the following years. However, only the 1950s saw the transition to modern particle physics. The technological progress made powerful particle accelerators become available and on the theoretical side, new quantum field theories (QFT) were developed. Eventually, nuclear substructures and previously unknown particles were observed. Further, one discovered two new fundamental forces, which were called the strong and the weak interaction. The works of SHELDON GLASHOW [1], STEVEN WEINBERG [2] and ABDUL SALAM [3] progressed into the so called *electroweak theory*, a unification of the weak and the electromagnetic force, which was set up in 1968. Within the 1970s [4], the strong force was also included and the theoretical framework eventually evolved into the *Standard Model of particle physics* (SM), a powerful unified field theory, that is used by

1. Preface

particle physicists until today in order to describe nature.

One of the most relevant predictions of the Standard Model is the existence of a Higgs boson, a particle that is related to the SM mechanism for elementary particles to acquire mass. In July 2012, the ATLAS- and CMS-Collaborations at the European Organization for Nuclear Research (CERN) announced the discovery of a Higgs-like resonance in the invariant mass spectrum of di-photon events [5, 6]. To this day, a lot of the particles' properties were already studied and it turned out to be a Higgs boson for certain. However, one has to make sure, whether the found particle is really the Standard Model Higgs boson, or a Higgs boson that points to new physics. Therefore, the Higgs boson properties, e.g. its quantum numbers and couplings, have to be measured as precisely as possible. As a consequence, important parts of experimental Higgs physics turned from searches into precision measurements.

A big mystery in modern particle physics regards the so called *hierarchy problem*. This issue deals with the question, why the observed Higgs mass of 125 GeV differs so much from its natural value, which is expected to be on the order of the PLANCK scale ($\sim 10^{19}$ GeV). Since the Higgs mass sets the order of the electroweak scale, the hierarchy problem is deeply connected to the question why the electroweak force is about 10^{24} times stronger than gravity. Some theorists try to solve these problems by introducing *supersymmetry* or *extra dimensions*. However, a full understanding of the *Yukawa coupling*, the interaction between a scalar and a Dirac field, is crucial. In particular, the coupling of the Higgs boson to the top quark is of prime interest and must be measured as precisely as possible, since this interaction is predicted to be the strongest Yukawa coupling within the Standard Model and therefore represents the dominating contribution to the Higgs mass correction terms. Furthermore, one of the most important Higgs production mechanisms at hadron colliders, the gluon-gluon-fusion, as well as one of the most important decay modes, the Higgs decay into two photons, run over a fermionic loop that is dominated by the virtual top quark contribution. However, studying the Yukawa coupling in these channels turns out to be only indirect and model dependent, since assumptions about the particle content within the loop must be made. Nonetheless, a direct, model independent measurement is desired. From some existing options, the production of top quark pairs with an associated Higgs boson is the most favourable, since the characteristic experimental signature of the top quarks allows a wide range of Higgs decay modes to be studied, especially those, that are usually hard to access at hadron colliders, such as the Higgs decay into two bottom quarks. This channel is of particular interest because it allows for both, the highest and second highest Yukawa coupling (within the Standard Model) to be studied at the same time.

Another topic of interest is connected to the observation of a large matter/antimatter-asymmetry in the universe. Even though theory predicts particles to be created in matter/antimatter-pairs, we do not observe the *baryonic* part of the universe¹ to be a composition of matter and antimatter with roughly equal portions. Instead, an almost exclusive formation of ordinary matter is observed. Mathematically, this matter/antimatter asymmetry is expressed as a violation of the *charge conjugation parity symmetry* (CP), which means a combination of charge conjugation symmetry (inversion of charge sign) and parity symmetry (inversion of spatial coordinates). Despite the fact that the Standard Model introduces CP violation via the weak interaction, many physicists expect different, additional beyond Standard Model (BSM) CP violating mechanisms, because the corresponding SM mechanism shows only a small effect and therefore cannot explain the observed magnitude of the asymmetry.

The Standard Model predicts the Higgs CP-quantum number to be CP-even ($CP = +1$). Further, the pure CP-odd case ($CP = -1$) could already be excluded by experiment [7]. However, quantum mechanics allows for mixed states and the discovered Higgs boson could still turn out to be a composition of CP-even and CP-odd components [8]. If this was indeed the case, a new form of CP violation could be observed in the Higgs-sector, which would manifest itself, inter alia, in angular distributions from Higgs decay products. Also, the top quark would not only show a scalar coupling to the Higgs but also a pseudo-scalar coupling, that would impact top quark spin correlations. Top quark spin correlations are found to be quite sensitive to new physics scenarios like this and these facts alone spell out the importance of studies on the coupling between Higgs bosons and top quarks.

Within the scope of this analysis, studies on various angular distributions of Higgs boson and top quark decay products are performed with the ATLAS experiment at the LHC. Thereby, Monte-Carlo-simulated (MC) events that include a full simulation of the ATLAS detector, are analysed in order to find angular observables with high sensitivity to a separation between signal and background. The most powerful angular observables are then used to enhance the performance of some multivariate techniques used in the ATLAS $t\bar{t}(H \rightarrow b\bar{b})$ search. Further, MC events with modified, non-Standard Model Higgs boson CP quantum numbers are studied in order to probe the sensitivity to a possible CP-violation in the $t\bar{t}H$ Yukawa coupling.

As usual in particle physics, natural units are used throughout this thesis. This means the speed of light in a vacuum c and the reduced PLANCK constant \hbar are set to $c = \hbar = 1$.

¹As also described later on, the universe consists only to 5% of baryonic matter. Baryons are particles, composed of three quarks, for example protons and neutrons.

2. The Standard Model of Particle Physics

The verbalisation “Standard Model of particle physics” represents a theory, which describes three of the four observed forces of nature in a unified way. Namely, the *electromagnetic*, the *weak* and the *strong force* are addressed within the Standard Model. Moreover, all known particles in the field of subatomic physics and their interactions, mediated by the mentioned forces, are characterised. In detail, the model describes a set of indivisible, elementary particles, which can be classified into so called *fermions* (particles with a half-integer spin quantum number) and *bosons* (particles with an integer spin value), see Chapter 2.1. In terms of theoretical physics, the Standard Model turns out to be a gauge quantum field theory, which respects the internal symmetries of the unitary product group $SU(3)_C \otimes SU(2)_I \otimes U(1)_Y$. Thereby, the group $SU(3)_C$ describes the gauge theory of the strong interaction, while the electroweak interaction is classified by the $SU(2)_I \otimes U(1)_Y$ product group [3]. According to *Noether’s theorem*, which states that every continuous symmetry of action also implies a corresponding conservation law, a conserved charge, such as the weak hypercharge Y , the weak isospin I or the colour charge C , can be assigned to each particle participating in a relevant interaction.

The Standard Model is mathematically self-consistent and renormalisable. Furthermore, its formulation is chosen to satisfy the laws of special relativity.

Almost all theoretical quantities predicted by the Standard Model have been experimentally studied and the corresponding results are in agreement with the theory. First of all, elementary particles, which were previously unknown but were predicted by the theory, eventually were observed, such as the top quark (1995) [9, 10], the tau neutrino (2000) [11] or, most recently, the Higgs boson (2012) [5, 6]. Up to now, there is no experimental observation that would conflict with the Standard Model explicitly up to a confidence level of $5\text{-}\sigma$. Such a confidence interval makes sure, that the chance of observing a “signal” within a background-only-hypothesis just due to a statistical fluctuation is very low: more than 99.9999 % of a normal distribution lies within an interval of five standard derivations ($5\text{-}\sigma$), making it a common requirement for claiming a discovery in particle physics.

2.1. Elementary Particles of the Standard Model

Fermions

The Standard Model knows twelve fundamental fermions, as well as their corresponding antiparticles. The spin quantum number of fermions is $1/2$. The fermions can be divided into six *leptons* and six *quarks*, which are further separated into three generations, see Figure 2.1. Each of these generations is made up by four fundamental particles, a pair of leptons and a pair of quarks. In detail, the generations are composed of left (right) handed weak isospin matter (antimatter) doublets (weak isospin $T = 1/2$) and right (left) handed matter (antimatter) weak isospin singlets ($T = 0$). The doublets contain an up-type quark (third component of the weak isospin $T_3 = +1/2$), that carries the electric charge $Q = +2/3$, a corresponding down-type ($T_3 = -1/2$) quark ($Q = -1/3$), as well as an up-type and a down-type lepton.

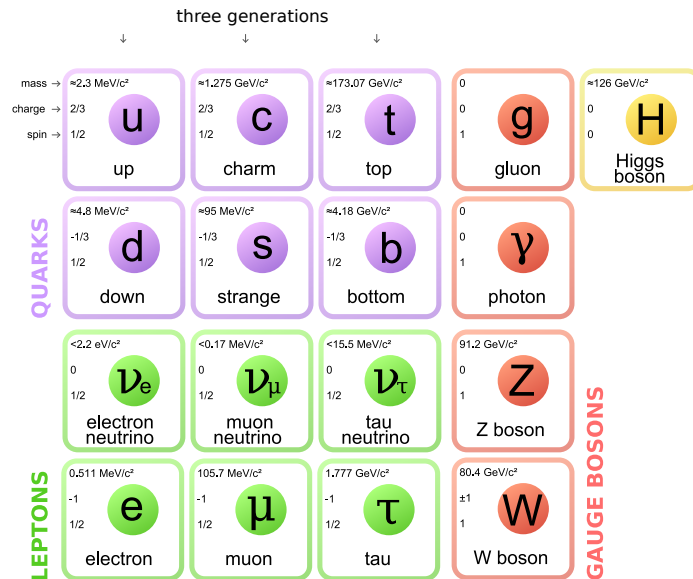


Figure 2.1.: The elementary particles and gauge bosons of the Standard Model.

Thereby the latter is electrically charged ($Q = -1$) and the respective lepton-neutrino does not carry electric charge ($Q = 0$) [1–3]. The singlets have $T_3 = 0$. The individual particles within one generation differ from each other by the different forces they interact with. While the quarks interact electromagnetically, weakly and strongly, the leptons only interact electroweakly or, depending on the corresponding charge, only weakly. Even though all particles with mass also underlie the gravitational force, this interaction is negligibly small and can be ignored, unless particle collisions happen at very high energies near the PLANCK scale, which is far from achievable with modern or even near future

technology. The main difference between the three generations manifests itself in the particles' masses. For example, the top quark is about 75000 times as heavy as the up quark and the tau lepton is still 3500 times as heavy as an electron. Due to convention, all elementary fermions and all other particles composed of these fermions are used to be called “matter”. In contrast, the term “antimatter” labels compositions of the fermions' antiparticles.

Vector Bosons

Several physical interactions (forces) are described by the Standard Model. These interactions happen via the exchange of vector bosons (spin-1 bosons), which are called gauge bosons. They can be considered as the field quantisations of the corresponding forces and the SM knows four of them. In terms of mathematics the gauge bosons are adjoint representations¹ of the corresponding symmetry group. The *photon* is the gauge boson of the $U(1)_Y$ group and it mediates the electromagnetic force. Because it does not carry electric charge, there is no photon self-interaction. This and the fact that the photon is a massless particle, make photons observable on a macroscopic scale. This means that the electromagnetic interaction acts fundamentally different compared to the strong force.

The quantum field theory that describes the strong force is called *quantum chromo dynamics* (QCD) and the corresponding gauge group is the $SU(3)_C$. The mediators of the strong force are called *gluons*. Eight different types of gluons exist because representations of $SU(N)$ groups are $N^2 - 1$ dimensional. These differ from each other by their colour wave functions. Here, colour means the charge of QCD, it has nothing to do with colour in a chromatic sense. Three different colours and their anti-colours exist. Without doubt, the most important feature of the strong interaction is the non-Abelian nature of QCD. Since the gluons carry a colour and an anti-colour charge (that do not cancel out), self-coupling between gluons will happen.

The strength of the strong interaction is given by the coupling constant α_s . However, this is actually not a constant but it depends on the energy scale Q^2 , whereby Q^2 means the absolute value of the squared four-momentum that is transferred at a vertex in a certain interaction of interest ($Q^2 = |q^2|$). Due to the increase of α_s at low energies and large distances (*confinement*), QCD processes can only be calculated perturbatively for high energies or short distances (*asymptotic freedom*), hence for $\alpha_s \ll 1$. In terms of physics, this behaviour of α_s leads to the following scenario: if two colour-charged particles are separated from each other, new colour-charged particles will be produced, once the en-

¹An adjoint representation is used to describe the elements of a Lie group as linear transformations of the underlying Lie algebra [12].

2. The Standard Model of Particle Physics

energy stored in the colour field exceeds the production energy threshold. As a consequence, free, colour-charged particles cannot be observed. Instead, if colour-charged particles are produced in a high energy collision, they will *hadronise* through QCD interactions and eventually end up in the detector as a *jet* containing many colourless hadrons. However, the top quark is an exception, since it has a lifetime ($\approx 5 \cdot 10^{-25}$ s) even shorter than the timescale of hadronisation ($\approx 10^{-23}$ s). This makes it possible to study “bare” properties of the top quark. In particular, the top quark spin correlations do not get distorted by QCD effects, which is *inter alia* an important requirement for this study.

The dependence of α_s on the energy scale and a certain *renormalisation scale* μ_R , which is needed for perturbative calculations at higher orders, is given by:

$$\alpha_s(Q^2, \mu_R^2) = \frac{\alpha_s(\mu_R^2)}{1 + \frac{\alpha_s(\mu_R^2)}{12\pi} (11 n_c - 2 n_f) \ln(Q^2/\mu_R^2)}. \quad (2.1)$$

Here, n_c is the number of colours and n_f represents the number of light quarks with $m_q \ll \mu_R$. Usually a cut-off parameter Λ is introduced and the equation can be written as:

$$\alpha_s(Q^2, \Lambda^2) = \frac{12\pi}{(11 n_c - 2 n_f) \ln(Q^2/\Lambda^2)}. \quad (2.2)$$

Thereby, Λ is chosen to set the scale below which QCD can no longer be treated perturbatively. As a consequence of colour confinement, the effective range of the strong force is very small and limited to a range of about 10^{-15} m, despite the fact that the gluons are massless particles.

The weak interaction is mediated by W^\pm and Z^0 bosons. The W bosons carry an electric charge ($Q = \pm 1$) while the Z boson is uncharged. Only particles of the isospin doublets take part in the weak interaction via the exchange of W bosons. This boson has the unique properties to allow for a crossing between the quark generations, theoretically explained by the *CKM* mechanism [13]. This theory states that the weak isospin eigenstates are in fact superpositions of the quark mass eigenstates (d, s, b), the linear combination is given by the *CKM matrix*:

$$\begin{pmatrix} d' \\ s' \\ b' \end{pmatrix} = \begin{pmatrix} V_{ud} & V_{us} & V_{ub} \\ V_{cd} & V_{cs} & V_{cb} \\ V_{td} & V_{ts} & V_{tb} \end{pmatrix} \begin{pmatrix} d \\ s \\ b \end{pmatrix}. \quad (2.3)$$

The diagonal entries V_{ii} show the biggest magnitude, so the coupling within one isospin doublet is favoured. The V_{ij} are free parameters of the Standard Model and must be

2.1. Elementary Particles of the Standard Model

determined by experiments, the recent values can be found in [14]. Unlike W bosons, Z bosons do not change the particle flavour. Consequently, a Z boson can not mediate a transition such as $s \rightarrow d$, which would be called *flavour changing neutral current* (FCNC). In the SM, FCNCs are only possible via higher order processes, however these are very rare since they are strongly suppressed by the *GIM* mechanism [15].

Due to the unitarity of the CKM matrix, the nine entries V_{ij} can be expressed with three mixing angles and one complex phase, which allows for CP-violation. In fact, the weak interaction via W boson exchange turns out to be a maximal parity violating coupling [16]. Mathematically this reflects in a *vector-axialvector* ($V-A$) structure of the coupling, which can be easily spotted in the weak interaction vertex for the W^\pm bosons:

$$-\frac{i g_W}{2\sqrt{2}} \gamma^\mu (1 - \gamma^5) V_{ij}, \quad (2.4)$$

and for the Z^0 boson:

$$-\frac{i g_z}{2} \gamma^\mu (c_V - c_A \gamma^5). \quad (2.5)$$

Here, the Dirac matrices are denoted with γ^μ ($\mu = 0, 1, 2, 3$), $\gamma^5 = i \prod_{k=0}^3 \gamma^k$ and $g_{w/z}$ is the weak gauge coupling constant. The $V-A$ structure itself is given by the term $\gamma^\mu (1 - \gamma^5)$, whereby γ^μ represents the vector part and $\gamma^\mu \gamma^5$ represents the axialvector part of the coupling. Since the neutral weak current is not maximal parity violating, the constant $c_V = T_3 - 2Q \sin(\theta_W)$ describes the vector part and the constant $c_A = T_3$ describes the axialvector part of the Z boson coupling.

Contrary to the gauge bosons of the electromagnetic or the strong force, the mediators of the weak force were experimentally found to be massive particles [17–20]. The W boson weighs roughly 80 GeV, however the Z boson is even heavier. It has a mass of around 91 GeV. Due to the high mass of its mediators, the weak forces' effective range of influence is limited to the order of 10^{-18} m.

Without introducing a further mechanism to the Standard Model, the gauge bosons and fermions would remain massless. Introducing mass terms to the corresponding Lagrangians in an ad-hoc way leads to a violation of local gauge invariance. This is a major problem because the dynamics of particles are required to be invariant under local gauge transformations of certain parameters. However, the spontaneous breaking of the gauge symmetry in the electroweak sector constitutes a working mechanism for the elementary particles and the gauge bosons to acquire mass. The symmetry breaking is performed with the help of an additional quantum field, the so called *Higgs* field.

2.2. Electroweak Symmetry Breaking and the Higgs Mechanism

Mass terms for gauge bosons emerge naturally in the Standard Model Lagrangian if the electroweak symmetry is spontaneously broken through the BROUT-ENGLERT-HIGGS-mechanism [21, 22], which introduces the scalar Higgs field. Local gauge symmetry is preserved this way. The Higgs field permeates the vacuum and is present everywhere in space. At high energies, excitations of this quantum field can occur and these are called Higgs bosons.

Symmetry Breaking of a Scalar Field and the BEH-Mechanism

First, one may consider a complex-valued scalar field ϕ composed of the real fields ϕ_1 and ϕ_2 :

$$\phi = \frac{1}{\sqrt{2}}(\phi_1 + i\phi_2), \quad (2.6)$$

with the Lagrangian [14]:

$$\mathcal{L} = \underbrace{(\partial_\mu \phi)^\dagger (\partial^\mu \phi)}_{\text{Kinetic term}} - \underbrace{\mu^2 (\phi^\dagger \phi)}_{\text{Mass term}} - \underbrace{\lambda (\phi^\dagger \phi)^2}_{\text{Interaction term}}, \quad (2.7)$$

where $\mu^2 (\phi^\dagger \phi) + \lambda (\phi^\dagger \phi)^2$ is the potential term with a global $U(1)$ symmetry. Since $\phi'^\dagger \phi' = \phi^\dagger \phi$, the potential is invariant under the transformation $\phi \rightarrow \phi' = e^{iQ} \phi$. The potential must have a minimum in order to describe a physical vacuum state. Mathematically this requires $\lambda > 0$. For $\mu^2 > 0$, the potential takes the shape of a two dimensional parabola with a single minimum at $\phi_1 = \phi_2 = 0$. However, for spontaneous symmetry breaking one considers $\mu^2 < 0$. This way there is not a single minimum but a two dimensional ring of minima, (see Figure 2.2) at:

$$\phi_1^2 + \phi_2^2 = -\frac{\mu^2}{\lambda} \equiv \nu^2, \quad (2.8)$$

whereby ν is called the *vacuum expectation value*. Since a physical vacuum state will occur at the minima and this state will break the global $U(1)$ symmetry of the Lagrangian \mathcal{L} . For a classical analogy, one can think of a ball spontaneously rolling down a hill. The rotational symmetry would be broken in this picture. Without loss of generality, it is possible to choose the vacuum state to be in the real direction $(\phi_1, \phi_2) = (\nu, 0)$ in order to simplify the following calculations. The physics does not get affected. If the vacuum state

2.2. Electroweak Symmetry Breaking and the Higgs Mechanism

was indeed in an arbitrary direction, the chosen basis would be different from the mass-eigenstate basis. The emerging terms would be harder to interpret physically. However, one could then rotate the potential and rewrite the Lagrangian in terms of the transformed potential to obtain the same results.

To actually obtain physical interactions and particles, one has to rewrite the scalar fields expanded at the vacuum state:

$$\phi_1(x) = \eta(x) + \nu, \quad (2.9)$$

$$\phi_2(x) = \xi(x), \quad (2.10)$$

$$\phi = \frac{1}{\sqrt{2}} (\eta + \nu + i\xi), \quad (2.11)$$

where $\eta(x) = \xi(x) = 0$ at the minimum. The corresponding Lagrangian can then be rewritten as:

$$\mathcal{L} = \underbrace{-\frac{1}{4} \lambda \nu^4}_{\text{Constant term}} + \underbrace{\lambda \nu^2 \eta^2}_{\text{Mass term}} + \underbrace{\lambda \nu \eta^3 + \frac{\lambda}{4} \eta^4 + \frac{\lambda}{4} \xi^4 + \lambda \nu \eta \xi^2 + \frac{1}{2} \lambda \eta^2 \xi^2}_{\text{Physical interaction terms}}, \quad (2.12)$$

$$\equiv \frac{1}{2} (\partial_\mu \eta) (\partial^\mu \eta) - \frac{1}{2} m_\eta^2 \eta^2 + \frac{1}{2} (\partial_\mu \xi) (\partial^\mu \xi) - V_{\text{int}}(\eta, \xi), \quad (2.13)$$

where the mass terms are $m_\eta = \sqrt{2\lambda\nu^2}$ and $m_\xi = 0$. The term $V_{\text{int}}(\eta, \xi)$ describes the physical interaction of the massive scalar field η and the massless scalar field ξ , whose excitations are NAMBU-GOLDSTONE bosons. According to Goldstone's theorem, a breaking of a continuous symmetry implies the existence of those massless scalar particles. However, in order to obtain the physical bosons of the Standard Model one has to apply the BEH-mechanism to a different symmetry group.

Electroweak Symmetry Breaking in the Standard Model

The relevant group product for the electroweak part of the SM is the $SU(2)_L \otimes U(1)_Y$. The BEH-mechanism has to provide four degrees of freedom (d.o.f) from Goldstone bosons in this case. Three of them for the longitudinal d.o.f of the W^\pm and Z^0 boson and one d.o.f for the Higgs boson. Thereby a longitudinal d.o.f directly implies the particles to be massive. A massless particle must not have a longitudinal d.o.f, otherwise parts of the field would travel faster than light, which would violate the principles of special relativity. In order to obtain these additional d.o.f, one now considers a charged scalar field for the charged bosons and a neutral scalar field for the neutral bosons. These two fields are put

2. The Standard Model of Particle Physics

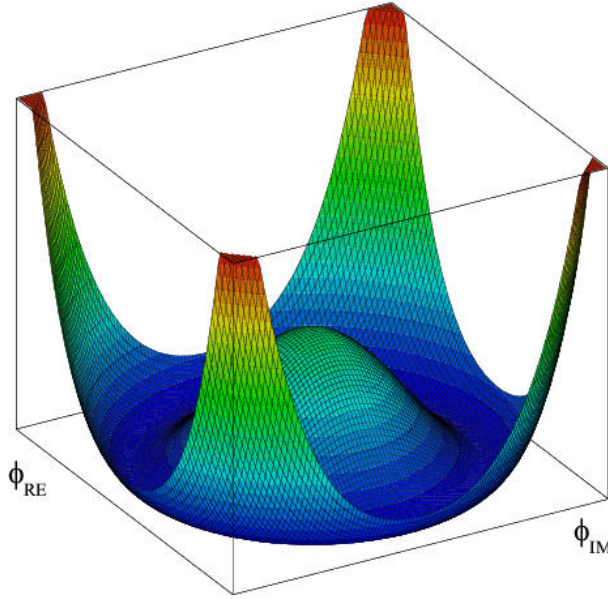


Figure 2.2.: The shape of the Higgs potential.

together in an isospin doublet:

$$\phi = \begin{pmatrix} \phi^\pm \\ \phi^0 \end{pmatrix} = \frac{1}{\sqrt{2}} \begin{pmatrix} \phi_1 + i\phi_2 \\ \phi_3 + i\phi_4 \end{pmatrix} \quad (2.14)$$

In the same manner as described in the previous section, one can write down ϕ in the unitary gauge, expressed via the vacuum expectation value. Thereby, only the neutral part is different from zero since the SM Higgs boson is uncharged. In the next step the Lagrangian is restructured in terms of the electroweak gauge fields. This leads to the desired d.o.f for the longitudinal polarisations of the gauge bosons and a massive scalar field, which represents the Higgs boson. In the first instance one obtains the physical bosons W^1, W^2, W^3 and B . The corresponding Standard Model mass eigenstates W^\pm, Z^0 and γ are obtained through linear combinations of the W and B bosons. Thereby, the photon γ remains massless and the other bosons acquire a mass. The fermion masses are generated in a slightly different way. They are described by the coupling, known as the Yukawa coupling, to the Higgs field and a higher Yukawa coupling leads to a larger mass. However, neutrinos remain massless in the SM. Even though one could add neutrino interaction terms to the Higgs Lagrangian, this would require right handed neutrinos. These would not take part in any interaction (sterile neutrino), except for the tiny Yukawa coupling. Whether they exist or not is questionable. Further, the large mass hierarchy between neutrinos and the other fermions makes it look unlikely that these masses are generated by the same mechanism. This is why a different model, the *Seesaw*

2.2. Electroweak Symmetry Breaking and the Higgs Mechanism

mechanism [23–28] is the preferred generator for neutrino masses.

Nevertheless, it is also possible for the Higgs boson to couple to itself. This behaviour is visualised in the following Lagrangian, that shows the Higgs interaction terms [14]:

$$\mathcal{L} = \underbrace{-g_{Hf\bar{f}}\bar{f}f\bar{f}H}_{\text{Higgs to fermion coupling}} + \underbrace{\frac{g_{HHH}}{6}H^3 + \frac{g_{HHHH}}{24}H^4}_{\text{Higgs self-coupling}} + \delta_V V_\mu V^\mu \underbrace{\left(g_{HVV}H + \frac{g_{HHVV}}{2}H^2\right)}_{\text{Higgs to gauge boson coupling}}, \quad (2.15)$$

where $V = W^\pm$ or Z^0 and $\delta_W = 1$, $\delta_Z = 1/2$. The coupling constants are the following:

$$g_{Hf\bar{f}} = \frac{m_f}{\nu}, \quad g_{HVV} = \frac{2m_V^2}{\nu}, \quad g_{HHVV} = \frac{2m_f^2}{\nu^2} \quad (2.16)$$

$$g_{HHH} = \frac{3m_H^2}{\nu}, \quad g_{HHHH} = \frac{3m_H^2}{\nu^2}. \quad (2.17)$$

With a vacuum expectation value around 246 GeV, which can be derived from the W^\pm boson mass and the weak gauge coupling, the Yukawa coupling of the Higgs particle to the top quark is at the order of ~ 1 . This gives rise to the question if the top quark might play a special, yet unknown role in the electroweak symmetry breaking. Furthermore, a lot of possible new physics scenarios appear in connection with top quarks or Higgs bosons.

The Higgs Boson

The Standard Model Higgs boson, named after the British physicist PETER HIGGS, is a scalar (spin-0) elementary particle that does not carry electric charge ($Q = 0$). Its parity is even ($J^P = 0^+$). For a long period of time, the most important goal of the physicists working with the ATLAS or CMS experiments at CERN was the discovery of the Higgs boson. In fact it was one of the main arguments to even build the Large Hadron Collider, which is up to now the most powerful particle collider on earth, in terms of beam energy and collision energy. Further, the existence of a Higgs boson was one of the strongest tests on the Standard Model because the BEH-mechanism represents an essential part of the theory and it predicts the Higgs boson as an excitation of the Higgs field.

In July 2012, the discovery of a spin-0 resonance with a mass of 125 GeV was announced by the European Organisation for Nuclear Research (CERN) [5, 6]. So far, this resonance is consistent with the SM Higgs boson. However, the experimental physics in the Higgs sector eventually turned into precision measurements and an investigation in the properties and couplings of the particle is a topic of current research.

2. The Standard Model of Particle Physics

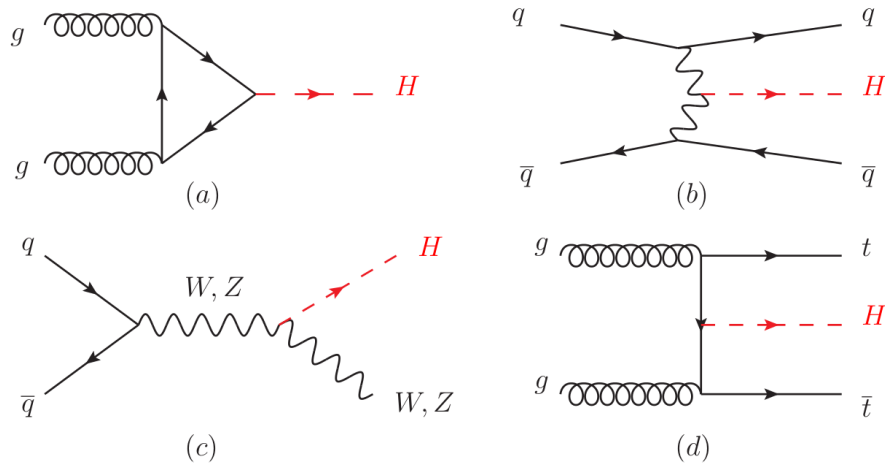


Figure 2.3.: Feynman diagrams of the four major Higgs production processes. At the LHC, the gluon-gluon-fusion (a) and vector-boson-fusion (b) are the most important production channels. The channel (c) is called Higgs-strahlung and (d) is associated production with top quarks.

In 2013, PETER HIGGS and FRANÇOIS ENGLERT received the Nobel Prize for the theoretical development of the Higgs mechanism.

The LHC is a proton-proton collider and therefore initial state anti-quarks are less present than in proton-anti-proton colliders. Consequently, the main Higgs production modes at the LHC are gluon-gluon-fusion (ggH) and vector boson fusion (VBF), see Figure 2.3. The most important decay modes are $H \rightarrow \gamma\gamma$, $H \rightarrow ZZ \rightarrow \ell^+\ell^-\ell^+\ell^-$, $H \rightarrow W^+W^- \rightarrow \ell^+\nu\ell^-\bar{\nu}$, $H \rightarrow \tau^+\tau^-$, and $H \rightarrow b\bar{b}$. The branching fractions of most of these decay modes are visualised in Figure 2.4. Thereby, the Higgs decay mode $H \rightarrow b\bar{b}$ is of particular

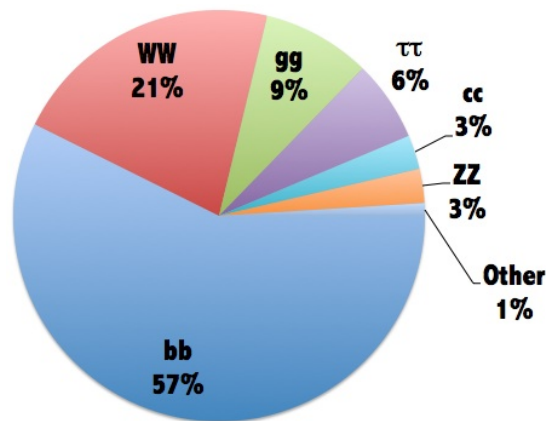


Figure 2.4.: Branching fractions of the Standard Model Higgs boson.

interest in this analysis. The bottom quark is (after the top) quark the second heaviest

fermion and has therefore the second largest Yukawa coupling. Since the Higgs boson is too light to decay into two on-shell W , Z or even into top quarks, the mode $H \rightarrow b\bar{b}$ has the largest branching fraction of approximately 60%. However, investigating this channel is extremely difficult at hadron colliders, because a huge QCD background dominates the signal. Nevertheless, in an associated production of top quarks with an additional Higgs, the characteristic signature of the top quark decays even allows the study of difficult channels like $H \rightarrow b\bar{b}$. Another advantage of $t\bar{t}(H \rightarrow b\bar{b})$ is that both the highest and second highest Yukawa coupling can be studied in a single process.

2.3. The Top Quark

The existence of the top quark was predicted long before its discovery. In 1973, when KOBAYASHI and MASKAWA described a mechanism to explain the CP-violation observed by CRONIN and FITCH in 1964 [29], they proposed a third quark generation [13]. Eventually the E288 experiment observed [30] the Υ meson in 1977. This resonance consists of a b and a \bar{b} quark, consequently, the third quark generation was discovered. However, the weak isospin partner of the bottom quark, the top quark, was not seen in the following 20 years. Only in 1995, the DØ and CDF collaborations announced the top quark observation [9, 10]. The top quark is the heaviest particle in the Standard Model and because of its high mass ($m_t \approx 173 \text{ GeV}$), only two colliders are or were able to produce these particles, the LHC and the TEVATRON. At the LHC, around 6 million top quark pairs were produced within the ATLAS detector during Run-I and more than 75 million during Run-II [31].

The top quark shows some properties that make it unique among all other quarks. If one calculates the top quark decay width Γ_t at leading order (LO) one obtains [32]:

$$\Gamma_t^0 = \frac{G_F m_t^3}{8\pi\sqrt{2}} |V_{tb}|^2 (1 + 2\beta^2) (1 - \beta^2)^2, \quad (2.18)$$

where G_F is the Fermi constant, $|V_{tb}|$ is a CKM matrix element and $\beta = m_W/m_t$ is the ratio between the W boson mass and the top quark mass. At next-to-leading-order (NLO) in QCD one gets the following approximation:

$$\Gamma_t^{\beta \rightarrow 0} = \Gamma_t^0 \left(1 - \frac{2\alpha_s}{3\pi} \left(\frac{2\pi^2}{3} - \frac{5}{2} \right) \right). \quad (2.19)$$

This is a valid approximation because $\beta \approx 0.46$ and the ratio between the NLO and LO decay width versus β is approximately constant for $0 < \beta < 0.6$ [32]. If one inserts the

2. The Standard Model of Particle Physics

corresponding values like $m_t \approx 173 \text{ GeV}$, $m_W \approx 80 \text{ GeV}$, $|V_{tb}| \approx 1$ and $\alpha_s(m_Z^2) \approx 0.12$ [14], one will arrive at a top quark decay width of

$$\Gamma_t^{\beta \rightarrow 0} \approx 1.4 \text{ GeV}. \quad (2.20)$$

A particles lifetime τ is inversely proportional to its decay width. In the case of the top quark one would obtain the following lifetime:

$$\tau_t = \frac{\hbar}{\Gamma_t} \approx 5 \cdot 10^{-25} \text{ s}. \quad (2.21)$$

This extremely short lifetime makes the top quark special. A comparison to the timescale of hadronisation t_{had} (see Equation 2.22) shows that the top quark tends to decay before it gets affected by low energy QCD interactions:

$$t_{\text{had}} = \frac{\hbar}{\Lambda_{\text{QCD}}} \approx 10^{-23} \text{ s}. \quad (2.22)$$

This timescale depends on the chosen cut-off parameter Λ_{QCD} , which lies in the order of several hundred MeV. Since it decays before hadronisation, the top quark can transfer its properties to the decay products unperturbed, allowing in principle for studies of “bare” quark properties. Thereby, the top quark spin correlations are of particular interest within this analysis. As stated in [33, 34], the timescale of top quark spin-decorrelation is given by:

$$t_{\text{decor}} = \frac{\hbar_t}{\Lambda_{\text{QCD}}^2} \approx 10^{-21} \text{ s}. \quad (2.23)$$

As one can see $t_{\text{decor}} \gg t_{\text{had}}, \tau_t$ and therefore one expects the top quark spin correlations to be transmitted to the top decay products.

Top Quark Production

At hadron colliders, two different top production mechanisms exist: via the strong interaction, which produces top-anti-top quark pairs, and via the electroweak interaction, which produces events with a single top quark in it. However, the top quark pair production via the strong interaction is the dominating mechanism. Electroweak pair production is extremely suppressed and can be neglected. Within the strong production, top quark pairs are either produced via gluon-gluon fusion or quark-antiquark annihilation, see Figure 2.5. Which of those processes is dominating depends on the initial state partons. At

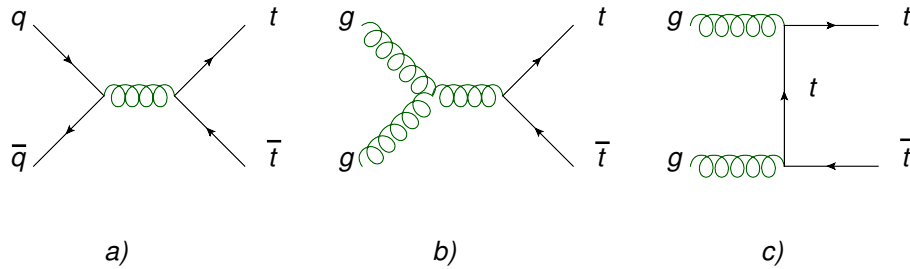


Figure 2.5.: Feynman diagrams of the dominating top quark production mechanisms at the LHC. The quark-anti-quark annihilation is visualised in (a), (b) and (c) show gluon-gluon-fusion.

LHC energies, gluons are the most present partons in the initial state, therefore gluon-gluon fusion dominates. At the TEVATRON, however, the quark-antiquark annihilation represented the leading top production mechanism due to the lower energy ($\sqrt{s} \approx 2 \text{ TeV}$) and because antiquarks were present as valence quarks (since the TEVATRON was a $p\bar{p}$ collider) in the initial state.

Single top quarks can be produced via the s -channel, the t -channel or in association with a W boson (Wt channel), see Figure 2.6. Therefore the electroweak production can be used to study the coupling between the top and the W boson [35, 36]. The single top production via s and t -channel was first observed by CDF and DØ at the TEVATRON in 2009 [37, 38]. The single top production can be used to measure the CKM matrix element $|V_{tb}|$, see for example [39].

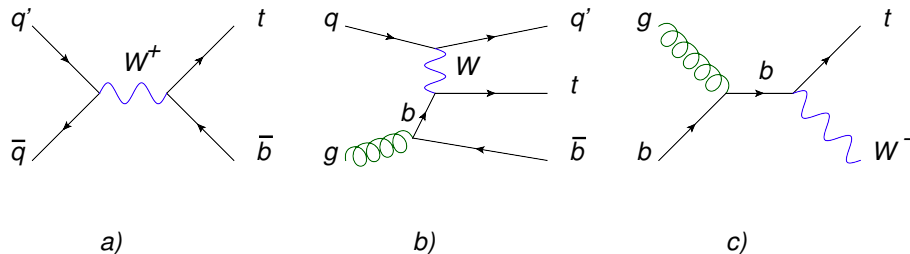


Figure 2.6.: Leading order Feynman diagrams for the production of single top quarks via the electroweak interaction. The s -channel process is visualised in (a) and the t -channel process is shown in (b), (c) shows the associated production of a top quark and a W boson.

Top Quark Decay

The top quark decay is mediated by the weak interaction and since $|V_{tb}|$ is very close to one, it almost always decays into a W^+ boson and a b quark (or in case of the antiparticle, $\bar{t} \rightarrow W^- + \bar{b}$). As a consequence, the final state will be defined by the decay mode of the

2. The Standard Model of Particle Physics

W boson. In around 33% of the cases the W boson will decay into a charged lepton and the corresponding neutrino. One would call this decay mode a “leptonically decaying top quark”. In roughly 67% of its decays the W boson will produce quarks (“hadronically decaying top quark”). However, one has to be careful when it comes to the tau leptons, since they can decay leptonically and hadronically. Usually, a top quark decay into a hadronically decaying tau lepton is labelled as a hadronically decaying top, but it can depend on the analysis. The treatment of tau leptons within this analysis, is described in Chapter 4.2.1

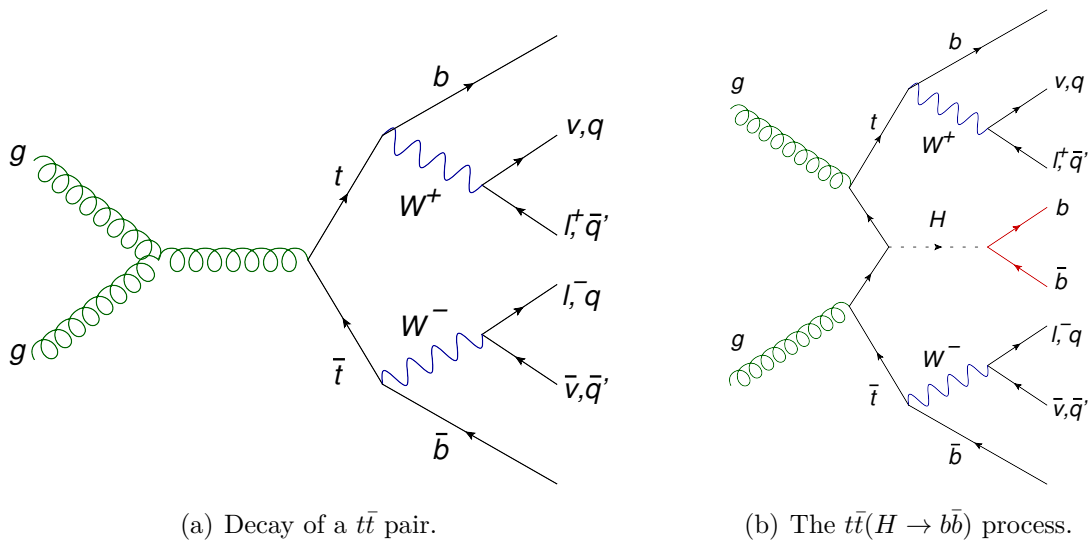


Figure 2.7.: The Feynman diagram on the left shows the top quark pair production via the strong force and its weak decay into a dilepton or lepton + jets final state. The Feynman diagram on the right shows the $t\bar{t}$ pair production with an associated Higgs boson, that decays into a $b\bar{b}$ pair.

In the detector, a hadronically decaying top quark will show up as several light jets and a b -jet (see Figure 2.7), which can be identified through b -tagging algorithms, which make use of the relatively long lifetime of B -mesons ($\sim 10^{-12}$ s). The signature of leptonically decaying top quarks is a b -jet, a charged lepton and missing transverse momentum that is due to the neutrino, whose interaction is so weak that it is not detectable. However, the missing momentum can be calculated from momentum conservation.

When it comes to the decay of a $t\bar{t}$ pair, three channels are possible: the *all-jets* (or fully hadronic) channel, the *dilepton* channel and the *lepton + jets* (or semileptonic) channel. Although the fully hadronic mode shows the highest branching fraction and therefore the highest statistics, it is also the most challenging channel because of the huge multi-jet backgrounds. Studies in this channel also suffer from a large combinatorial

background that arises from wrong assignments of the six jets to their mother particles. The dilepton channel takes advantage of a higher signal-to-background ratio because the two charged leptons can suppress a lot of backgrounds. Charged leptons usually have a good resolution in terms of their four-momentum. Their charge allows them to be classified as top or anti-top decay products. Unfortunately, the two neutrinos that occur in the final state are experimentally challenging. For a full event reconstruction, one has to rely on sophisticated methods, like *neutrino weighting* (ν -weighting) [40]. However, even with such a technique the reconstruction in the dilepton channel is in general worse than in the single lepton decay channel.

The lepton + jets channel allows for a full event reconstruction because there is only one neutrino in the final state, unless the W boson decays into a τ lepton, which might decay leptonically. Powerful algorithms like *KL Fitter* [41] allow for a precise event reconstruction in the single lepton channel. The charged lepton is useful for background suppression, however not as much as in the dilepton channel. Conversely, the semileptonic channel offers more statistics than the dileptonic channel. In this manner the lepton + jets mode forms a compromise between the all-jets and dilepton channel.

Within this analysis, both the dilepton and the lepton + jets channels are studied, however the all-jets channel will play no further role.

2.4. Top Quark Spin Correlations

Since the top quark decays before its spin information gets disturbed by QCD effects, the corresponding spin correlations are observable. At hadron colliders, top quarks are not polarised, however the spins of $t\bar{t}$ pairs are expected to be strongly correlated [42–44]. Experimentally, this behaviour was confirmed at the TEVATRON and at the LHC [45–48]. The top decay products act as spin analysers and their correlation to the original top spin quantisation axis is given by [34]:

$$\frac{1}{\Gamma_t} \frac{d\Gamma}{d \cos(\varphi_i)} = \frac{1}{2} (1 + \alpha_i \cos(\varphi_i)), \quad (2.24)$$

where Γ_t is the top decay width, φ_i is the angle between a top decay product i and the top spin quantisation axis within the top rest frame and α_i is the spin analysing power of

2. The Standard Model of Particle Physics

the top decay product. At leading order, α_i is given by

$$\alpha_i = \begin{cases} 1, & \text{for the down type fermions from the } W \text{ decay,} \\ -0.31, & \text{for the up type fermions from the } W \text{ decay,} \\ 0.41, & \text{for the } W \text{ from the top decay,} \\ -0.41, & \text{for the } b \text{ quark from the top decay.} \end{cases} \quad (2.25)$$

for the top decay products. In case of the anti-top decay products one has to invert the signs of the spin analysing powers given in the equation above. As a consequence of the $t\bar{t}$ spin correlation, and the relation between the $t\bar{t}$ spin and their decay products, the latter will also be correlated among each other. Further, their correlation can be expressed via [34]:

$$\frac{1}{\sigma_t} \frac{d^2\sigma}{d\cos(\varphi_i) d\cos(\bar{\varphi}_{\bar{i}})} = \frac{1}{4} (1 + C_{t\bar{t}} \alpha_i \bar{\alpha}_{\bar{i}} \cos(\varphi_i) \cos(\bar{\varphi}_{\bar{i}})), \quad (2.26)$$

with the spin analysing power α_i from a top decay product i and $\bar{\alpha}_{\bar{i}}$ from an anti-top decay product \bar{i} , as well as with the correlation parameter $C_{t\bar{t}}$, which depends on the chosen spin axes of the $t\bar{t}$ pair. It is given by the following relation:

$$C_{t\bar{t}} = \frac{\sigma_{\uparrow\uparrow} + \sigma_{\downarrow\downarrow} - \sigma_{\uparrow\downarrow} - \sigma_{\downarrow\uparrow}}{\sigma_{\uparrow\uparrow} + \sigma_{\downarrow\downarrow} + \sigma_{\uparrow\downarrow} + \sigma_{\downarrow\uparrow}}. \quad (2.27)$$

Here, $\sigma_{\uparrow/\downarrow\uparrow/\downarrow}$ labels the $t\bar{t}$ pair production cross section with the top quark spin pointing up or down with respect to the top quantisation axis in the top rest frame and the anti-top quark spin pointing up or down with respect to the anti-top quantisation axis in the anti-top rest frame. Obviously, one has to perform the spin correlation measurement within a well chosen spin basis, where $C_{t\bar{t}}$ is as high as possible. However, the best possible basis is directly connected to the $t\bar{t}$ helicity configuration, which again highly depend on the helicities of the initial state particles and also on the $t\bar{t}$ production mechanism itself. Since $gg \rightarrow t\bar{t}$ dominates over $q\bar{q} \rightarrow t\bar{t}$ at the LHC the following discussion will be limited to the gluon-gluon fusion.

Spin Configurations in $t\bar{t}$ Production with Unlike-Helicity Gluons

In Figure 2.8 the helicity configurations are visualised for different kinematical limits, where β is representing the velocity of the $t\bar{t}$ zero-momentum-frame (ZMF), divided by

the speed of light. For a theoretical derivation of the spin configurations, see [34].

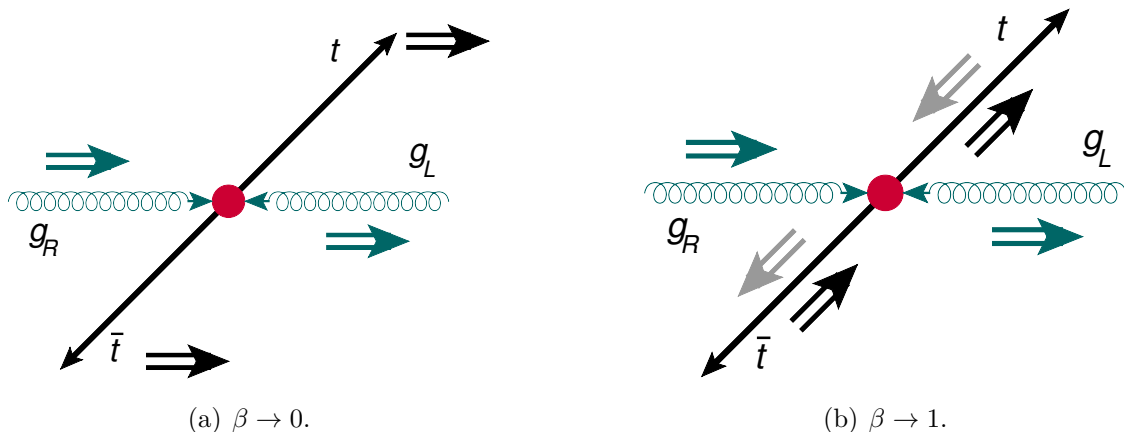


Figure 2.8.: The process $g_R g_L \rightarrow t \bar{t}$ is shown. The double-lined arrows represent the alignment of the spins with respect to the directions of motion, which are indicated by the single-lined arrows. In the limit $\beta \rightarrow 0$ (a) the $t \bar{t}$ spins are aligned with the initial state (gluon) spins. For $\beta \rightarrow 1$ (b) the top spins are in LR or RL configuration.

The initial state gluons have unlike helicity. This means one is right handed (R , spin points along the direction of momentum) and one is left handed (L , spin points against the direction of momentum). In the case $\beta \rightarrow 0$, the top spins are aligned with the gluon spins, which point in or out of the direction of the incoming particles². Therefore, the top spins are best described through the *beamline basis*. In the ultrarelativistic limit $\beta \rightarrow 1$, the $t \bar{t}$ pair will be produced in the LR or in the RL configuration. Which configuration is preferred depends on the scattering angle ξ :

$$\frac{W(t_R \bar{t}_L)}{W(t_L \bar{t}_R)} \sim \frac{(1 + \cos(\xi))^2}{(1 - \cos(\xi))^2}, \quad (2.28)$$

where W labels the probability for the certain helicity configuration. For scattering angles smaller than 90° , the $t_R \bar{t}_L$ configuration will dominate and vice versa. Obviously, for $\beta \rightarrow 1$, the *helicity basis* describes the top spins best. The helicity basis is obtained by the direction of motion of the top or anti-top quark within the centre-of-mass frame of the $t \bar{t}$ pair. There is also a basis that interpolates between both limits $\beta \rightarrow 0, 1$. This basis is called the *off-diagonal basis*, however, it maximises the correlation parameter $C_{t\bar{t}}$ in the case of $q\bar{q}$ annihilation but not for gluon fusion, and therefore one would rather use it under TEVATRON conditions but not at the LHC. Nevertheless, it is also possible to find a maximising basis in case of the LHC [34].

²In Figure 2.8 and 2.9, if the gluon spins were inverted, one would also have to flip the top quark spins.

Spin Configurations in $t\bar{t}$ Production with Like-Helicity Gluons

In Figure 2.9 the helicity configurations (derived in [34]) of the $t\bar{t}$ pair is visualised for a production where the initial state gluons have the same helicity. In the limit $\beta \rightarrow 0$ the helicities are described by the $t_R\bar{t}_R$ or the $t_L\bar{t}_L$ configuration.

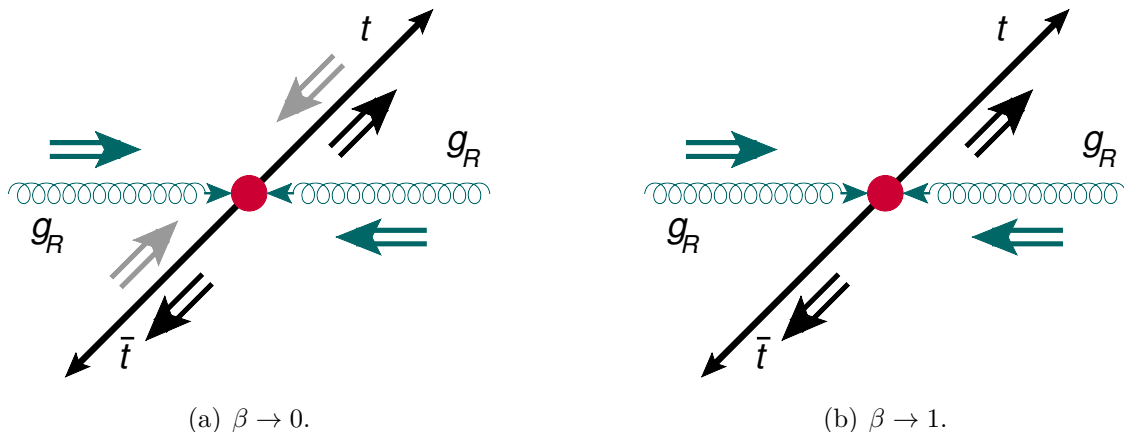


Figure 2.9.: The process $g_R g_R \rightarrow t\bar{t}$ is shown. In the limit $\beta \rightarrow 0$ (a) the $t\bar{t}$ spins are in RR or LL configuration. For $\beta \rightarrow 1$ (b) the top spins are in pure RR configuration.

The relative probabilities for the RR or LL configuration is then given by:

$$\frac{W(t_R\bar{t}_R)}{W(t_L\bar{t}_L)} \sim \frac{(1 + \beta)^2}{(1 - \beta)^2}, \quad (2.29)$$

However, for ultrarelativistic velocities $\beta \rightarrow 1$ the top and anti-top quark will have the same helicities as the incoming gluons (in Figure 2.9 purely right handed). In contrast to the $t\bar{t}$ pair production with unlike-helicity gluons, the production via like-helicity gluons allows the helicity basis to describe the top spins best for all values of β .

One might ask now to what percentage the like and unlike helicity gluons occur in $\sqrt{s} = 13$ TeV collisions at the LHC. It is clear that both will contribute, since it is not possible to polarise the incoming gluons. In [34] it is stated that (at the LHC with $\sqrt{s} = 14$ TeV) in 65 % of the cases the gluons will be in like-helicity configuration. In 35 % of the cases, the gluons will have opposite helicity. Further, more than 75 % of the corresponding events show kinematics that favour the helicity basis as an optimal spin basis [34]. One might finally ask how much the correlation parameter differs if one uses the helicity basis in the full phase space instead of the optimal basis, that is more difficult to set up, but that maximises the correlation parameter $C_{t\bar{t}}$. As shown in [34], the difference is less than

10 %.

2.5. Limits of the Standard Model

Predictions of the Standard Model are well in agreement with experimental measurements over several orders of magnitude in energy. No experimental data conflicts significantly enough with the SM to claim an observation of new physics. However, the Standard Model also leaves a lot of important questions open and most particle physicists do not feel satisfied by this theory. The reason lies in several real and some aesthetic problems that the Standard Model suffers from.

Gravitation

Without doubt, the biggest and most obvious problem of the SM is its inability to describe the fourth force of nature, the gravitation. Therefore one already knows that the theory must be an incomplete description of nature. The root of this issue lies in the incompatibility between the most successful theory of gravity, which is called *general relativity* (GR, a classical field theory), and the framework of quantum field theory. Within quantum field theory one needs to renormalise coupling constants in order to get rid of divergencies that occur during the calculations of process amplitudes. However, gravity is found to be non-renormalisable and therefore non-vanishing divergencies in higher order calculations make predictions of gravitational process amplitudes impossible.

Under normal conditions, neither astronomy nor particle physics suffers much from the lack of a working quantum gravity because GR works out very well on large scales e.g stars or galaxies and QFT provides a good description of small scale structures like atoms and molecules. At these small scales gravity effects can be ignored because of their weakness. Conversely, in order to study extreme energy or mass scales such as black holes or early stages after the Big Bang, an understanding of quantum gravity would be essential.

Dark Matter and Dark Energy

Astronomical observations such as rotational velocities of galaxies or the bullet cluster galaxy have lead to the discovery that baryonic matter constitutes only 5 % of the universes' total energy. A much bigger part, roughly 26 %, is made up of so called *dark matter* [49]. This form of matter became recognised through its gravitational impact, however it does not seem to interact with the Standard Model fields. This means it is not directly visible and therefore “dark”. Dark matter might constitute a real problem

2. The Standard Model of Particle Physics

for the SM, because this theory does not predict a particle with appropriate properties to be a reasonable dark matter candidate. Supersymmetry (SUSY), a symmetry that connects fermionic and bosonic fields, might solve this problem, since it can introduce suitable dark matter candidates. In addition, supersymmetric extensions of the SM can provide a possible solution to the *hierarchy problem*, which is another important problem of the SM, even though more of an aesthetic problem than a real issue with the theory. For quite some time now particle physicists have actively searched for SUSY particles, however so far, none have been discovered.

The biggest part of the total energy in the universe, about 69%, is made up of *dark energy* [49]. This constant energy density was introduced in order to explain the observed increase in cosmic inflation. The dark energy fills out the vacuum, however its nature is very unclear. If one attempts to describe dark energy as a vacuum energy density that results from the Higgs potential, the calculated value is 10^{56} times larger than the measured value for the dark energy density and also has the opposite sign [50].

Neutrino Masses

Within the SM, neutrino masses are not generated via the Higgs mechanism. However, the SM description (massless neutrinos) conflicts with experimental observations: neutrino-oscillation-experiments [51, 52] show that neutrinos have mass. When the neutrino propagates through spacetime, the probability to measure a certain flavour oscillates periodically. However, this oscillation is only sensitive to the mass difference between the neutrino generations and not directly to their masses. Nevertheless, there are attempts to measure neutrino masses directly, for example with the KATRIN experiment [53].

Usually the Seesaw mechanism is added to the SM to explain neutrino masses, but the true origin of neutrino masses is still not very clear and it is not known whether neutrinos are really DIRAC or MAJORANA particles. The latter are their own antiparticles and, since neutrinos have no electric charge, they could be the only elementary particles that show a MAJORANA component.

The Gauge Hierarchy Problem

Although the gauge hierarchy problem can be counted as an aesthetic problem, it is directly connected to the top quark Yukawa coupling Y_t and therefore a motivation for the study of the $t\bar{t}H$ process.

The problem refers to the huge energy difference between the electroweak scale $\Lambda_{\text{weak}} \sim 10^3 \text{ GeV}$, which is determined by the Higgs boson, and the grand-unification (GUT) scale

$\Lambda_{\text{GUT}} \sim 10^{16}$ GeV or the PLANCK scale $\Lambda_{\text{Planck}} \sim 10^{19}$ GeV. If one takes a look at the QFT Higgs propagator, it is obvious that it will be subject to quantum loop corrections. The fermionic corrections contribute to the bare Higgs mass by:

$$\Delta m_H^2 = N_f \frac{g_f^2}{8\pi} \left[-\Lambda^2 - 6 m_f \ln \left(\frac{\Lambda}{m_f} \right) - 2 m_f^2 \right] + \mathcal{O} \left(\frac{1}{\Lambda^2} \right), \quad (2.30)$$

whereby $g_f = \sqrt{2} m_f / \nu$ and Λ is the cut-off scale, needed to regularise the corresponding integral. It will be equal to Λ_{GUT} or Λ_{Planck} if the Standard Model is valid up to those scales. One can see from Equation 2.30 that the top quark will give the leading contribution due to its high mass and because of the Λ^2 dependence one would expect the Higgs mass to be very high. However, the observed Higgs boson is quite light. In the SM, there are also loop contributions by the W, Z and also by the Higgs boson itself. The total one loop correction takes the following shape:

$$\Delta m_H^2 \sim \left(\frac{3}{4} (M_W^2 + M_Z^2 + M_H^2) - \sum m_f^2 \right) \left(\frac{\Lambda^2}{M_W^2} \right). \quad (2.31)$$

While a light Higgs mass leads to a vanishing of this one loop correction, this does not work out on higher orders. Therefore the problem of quadratic divergencies is real. There is no symmetry in the SM that would protect the Higgs mass. It seems very unlikely that the quantum corrections cancel out to 10^{30} digits just by chance, the hierarchy problem is therefore referred to as a problem of naturalness or fine-tuning. Supersymmetry, however can give an explanation of why the corrections should naturally cancel out: if superpartners of the SM particles run in the quantum loop, they would lead to corrections with opposite sign. This was one of the motivations for supersymmetric models.

One might ask why such loop contributions are not leading to fine tuning problems with regard to the masses of fermions or gauge bosons. The answer lies in the quadratic dependence $\sim \Lambda^2$, which is a feature of scalar particles, for fermions and bosons the mass corrections have logarithmic proportionality ($\sim \ln(\Lambda/m)$) to the cut-off scale and even for large Λ the correction is rather small.

CP Violation

If large antimatter regions would exist in the universe, one should be able to observe gamma rays emitted from the edges of these areas due to the particle-antiparticle annihilations that would happen there. However, this is not seen. Instead, a huge asymmetry between matter and antimatter is observed, even though, as mentioned in the introduc-

2. The Standard Model of Particle Physics

tion, one would expect equal amounts of each during the early stages of the universe. The Standard Model CP violation that is introduced over the CKM mechanism is a rather small effect and it cannot explain the magnitude of the observed asymmetry. Therefore, further CP violating physics is expected to exist and it is not excluded that CP violation might show up in connection to the Higgs boson, which also played an important role shortly after the Big Bang.

Strong CP Problem

Theoretically, the QCD-Lagrangian should feature natural terms [54, 55]:

$$\mathcal{L} = -\frac{1}{4} F_a^{\mu\nu} F_{\mu\nu}^a - \frac{\theta g^2}{32\pi^2} F_a^{\mu\nu} \tilde{F}_{\mu\nu}^a + \bar{\psi} \left(i \gamma^\mu D_\mu - m \exp(i\alpha\gamma^5) \right) \psi, \quad (2.32)$$

whereby the second term violates CP [55]. Furthermore, if one considers chiral transformations, a CP violating complex exponential in the mass term arises. For non-zero values of the angle θ or the quark chiral phase α one expects CP violation in strong interactions, however this is not observed. This means that the terms in question are at least very close to zero, which is considered unnatural.

A lot of different Standard Model extensions exist. Some introduce supersymmetry, others solve issues like the hierarchy problem with the help of extra dimensions. Further, there are also attempts to construct theories of everything like loop quantum gravity or string theory. Even though models like these are able to solve parts of the described SM problems, none of them are sophisticated enough to replace the Standard Model. Most often, these theories introduce new unsolved issues or they are not able to make falsifiable predictions, which would be necessary for a useful model.

3. The Experimental Setup

3.1. The Large Hadron Collider

The Large Hadron Collider (LHC) is situated at CERN near Geneva, approximately 100 m below the ground. The LHC is the most powerful particle accelerator of the world with regards to the centre-of-mass (COM) energy \sqrt{s} . It can be used to either collide protons or heavy ions, but since the relevant process for this study occurs as a result of proton collisions, the following description will focus on this only. It took ten years, from 1998 until 2008, to build the LHC. Currently, several different experiments are carried out at the LHC and more than 10,000 scientists from all around the world are involved in the corresponding collaborations.

The collider was built in order to allow for studies of the physics at the TeV scale. It should scrutinise electroweak predictions, explore the Higgs sector and in particular either lead to a Higgs boson discovery or rule out its existence. Studies on the top quark and the Higgs boson are a main task of the LHC. By pushing forward into the highest possible energy regimes, the LHC should contribute to a deeper understanding of the physical phenomena that we observe in our universe.

Because there was an incident with the cooling mechanism of the superconducting magnets when the LHC was put into operation, the collisions were initially performed at a COM energy of 7 and 8 TeV in the years from 2010-2012. However, the collider was designed with a centre-of-mass energy of $\sqrt{s} = 14$ TeV in mind. Eventually, after a two-year phase of upgrading, the COM energy in proton-proton collisions reached 13 TeV in 2015, as can be seen in Table 3.1.

Luminosity

The cross section, σ , represents an important quantity when it comes to particle physics. It describes the probability that a certain process will happen. The measured rate of a process also depends on the *instantaneous luminosity*, see Equation 3.1. The luminosity describes the number of collisions that take place within a certain area and period of time. The luminosity integrated with respect to time, $\int L dt$, quantifies the total number

3. The Experimental Setup

	Year	\sqrt{s} [TeV]	Peak Luminosity [$10^{33} \cdot \text{cm}^{-2} \text{s}^{-1}$]	Integrated Luminosity [fb $^{-1}$]
Run-I	2010	7	0.2	0.0481
	2011	7	3.65	5.46
	2012	8	7.73	22.8
Upgrade Phase	2013			
	2014			
Run-II	2015	13	5.0	4.2
	2016	13	13.8	38.5
	2017	13	20.6	47.1

Table 3.1.: The LHC performance during the years 2010-2017 [56, 57]. The listed luminosities are delivered to the ATLAS experiment.

of collisions. A large integrated luminosity is very important because it means a larger amount of data, and one needs a sufficient amount of statistics in order to study rare processes. Thereby, a high instantaneous luminosity reduces the amount of time that is needed to collect the relevant data. The general expression for the luminosity is

$$L = \frac{1}{\sigma} \frac{dN}{dt}. \quad (3.1)$$

Here dN labels the number of events detected within a certain time interval dt . For a circular collider the instantaneous luminosity can be calculated with the relation

$$L = \frac{n \cdot N_1 \cdot N_2 \cdot f}{A}. \quad (3.2)$$

where n is the number of bunches and N_1 and N_2 quantify the number of particles per bunch¹. The colliding frequency is given by f and the cross sectional area of the bunches is described by A .

In Table 3.1 one can see how much the instantaneous and the integrated luminosity increased (for the ATLAS experiment) over the years. However, this increase in performance comes at the expense of larger *pile up*. Pile up refers to multiple interactions from one bunch crossing or additional interactions from the following bunch crossing that happen shortly after each other and therefore get recorded at the same time. This means a higher luminosity is experimentally more challenging and good pile up suppression methods are needed. In 2017 a peak luminosity of roughly $20 \cdot 10^{33} \text{ cm}^{-2} \text{ s}^{-1}$ was achieved at the LHC, which is the world record for proton accelerators (situation November 2018). However,

¹For technical reasons a particle beam is not continuous. Instead, it consists of small particle bunches that follow each other at a high rate.

the future is expected to see the instantaneous luminosity increase even further.

The Structure of the Large Hadron Collider

The LHC shows a complex arrangement of pre-accelerators. The main colliding ring features a 26.7 km long beam pipe located in the tunnel of the former *Large Electron-Positron Collider* (LEP). However, before protons enter it, they travel through a linear collider (LINAC2, 50 MeV acceleration), the *Proton Synchrotron Booster* (1.4 GeV), the *Proton Synchrotron* (PS, 25 GeV) and finally through the *Super Proton Synchrotron* (SPS) that couples the protons (now with an energy of 450 GeV) into the main ring. In a synchrotron one continuously adjusts the magnetic field strength to keep the particles on a stable path. However, if a charged particle feels a force that would bend its trajectory, *synchrotron radiation* will be emitted. During this process the particle will lose a part of its (kinetic) energy E . This loss, ΔE , is proportional to

$$\Delta E \sim \frac{1}{R} \left(\frac{E}{m} \right)^4. \quad (3.3)$$

To reduce such losses one can either use colliding rings with a large radius R or accelerate particles with large mass m . This is the technical reason why protons, in practice, can be accelerated to higher energies than electrons or positrons. Obviously one has to make compromises when it comes to the design of high energy particle colliders. For example proton collisions do not have a very well defined initial state due to their substructure, and the collisions produce large QCD backgrounds so they are not as “clean” as electron collisions.

Nevertheless, one has to compensate the energy loss through synchrotron radiation. Therefore the circular LHC collider is not a real circle but it shows curved parts where particle trajectories are bent with superconducting dipole magnets and it also has straight sections where superconducting radio frequency cavities are used to accelerate the particles. If a certain energy is reached, these accelerations do not further increase the energy of the particle but just balance out the energy losses.

The superconducting elements are made of ultrapure NbTi, cooled down to a temperature of 1.9 K using liquid helium, which is technically challenging due to its superfluid state. The beam is focused using magnetic quadrupole, sextupole and octupole lenses. The acceleration of the particles requires an ultra high vacuum within the beam pipe. Because the LHC is a symmetric collider, both of the colliding beams will carry the same amount of energy. In general, the relation $\sqrt{s} = \sqrt{4E_1E_2}$ holds for the COM energy \sqrt{s} , with the energies E_1 and E_2 of the respective beams.

3. The Experimental Setup

The LHC features several detectors, which cover different purposes. Consequently they differ widely in size, mass and structure. Namely, the four biggest experiments at the LHC are called ATLAS, CMS, LHCb and ALICE.

3.2. The ATLAS Detector

ATLAS (*A Toroidal LHC ApparatuS*) is a particle detector at the LHC. The detector is about 46 m long and its diameter measures roughly 25 m. The detector weighs approximately 7,000 tons, making it much lighter than the CMS detector. Both CMS and ATLAS are “multi-purpose” detectors. Some of their main tasks are Higgs boson and top quark studies, as well as searches for supersymmetry and beyond Standard Model (BSM) physics. However, it is also possible to record data with ATLAS when heavy ions are collided.

The Structure of the ATLAS Detector

The detector is symmetric and consists of multiple layers, that encircle the beam pipe. Such a structure is rather typical for collision experiments. The purpose of the inner detector (ID) is to determine the origins of particle vertices, which are important for the particle reconstruction. Another important purpose, especially for top quark studies, is *b*-tagging, which means the identification of jets originating from *B*-hadrons. Thereby, good vertex resolution is crucial because *b*-tagging is based on the reconstruction of a secondary vertex, that occurs because, on average, the *B*-hadrons travel a small distance in the beam pipe before they decay. Momenta can be also measured from the curvature of the tracks of charged particles, that are bent in the 2 T magnetic field produced by the solenoid magnet, see Figure 3.1. For Run-II, the diameter of the beam pipe within the ATLAS detector was reduced in order to install the *Insertable B-Layer* (IBL). This was done to recover from radiation damage in the innermost part of the detector. Furthermore, the IBL represents an improvement when it comes to the identification of vertices due to its proximity to the beam pipe and small sized pixels. Therefore it provides better tracking and *b*-tagging. The IBL is followed by the *silicon-pixel detector*, that also provides a high resolution regarding the particle-interaction vertices. It consists of three layers in the barrel and three discs in the end-cap regions respectively. The silicon-pixel detector features more than 80 million read out channels. A *silicon-strip detector* encloses the inner pixel part. This element allows the trajectories of particles passing through it to be determined. As the name suggests, it does not consist of pixels, but it is built from small silicon strips. It features more than six million read out channels. The *transition*

radiation tracker (TRT) completes the inner detector. It makes use of transition radiation in order to distinguish electrons from hadrons. The solenoid magnet surrounds the inner detector.

The magnet is followed by the *electromagnetic calorimeter*, which is composed of lead-absorbers, layered with liquid argon. The calorimeter is used to determine the energy of electrons and photons. When these electromagnetically interacting particles pass through the material, they ionise it. The drift of the ions evoked by an applied electric field results in an induced electric charge, which allows for a measurement of the corresponding particle energy. In order to determine the energy of hadrons, the *hadronic calorimeter*

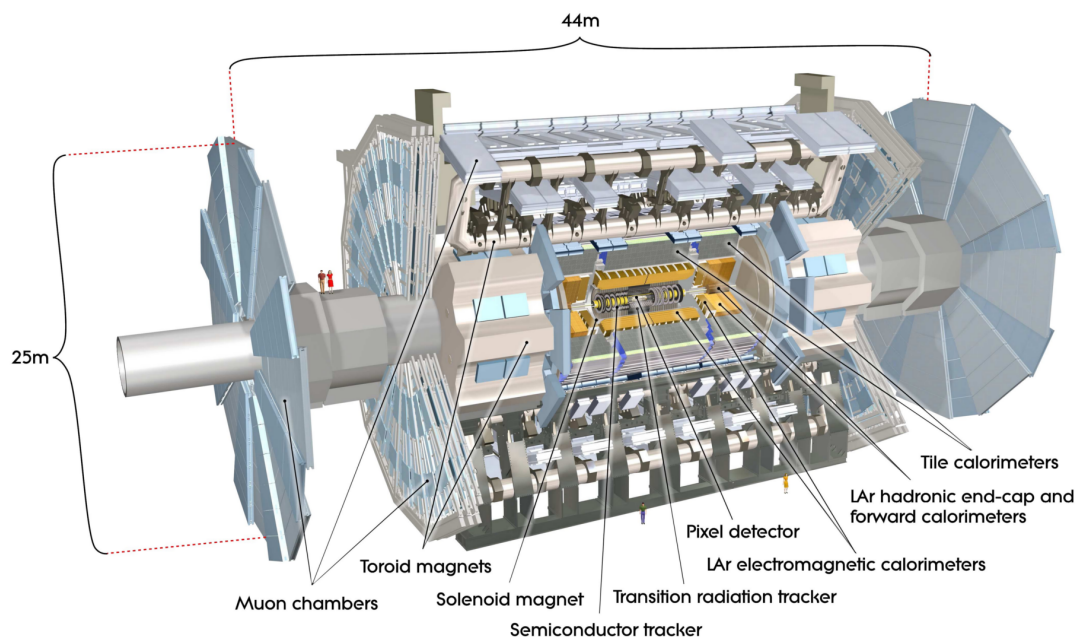


Figure 3.1.: The structure of the ATLAS detector.

is used. It consists of steel-plates, which are layered with synthetic scintillators. If a high-energy particle penetrates the calorimeter, light pulses occur in the scintillators as a consequence of the particle showers taking place in the steel plate. These pulses can be read out and they allow the energy of the corresponding particle to be measured. Near the beam axis, layers of copper and tungsten are inserted to improve the radiation hardness of the hadronic calorimeter.

Muons do not lose much of their energy in the calorimeters, because they are minimal ionising particles. Instead, their energy is measured in the *muon spectrometer* (MS). It is placed at the outermost region of the ATLAS detector. A powerful magnetic field of 4 T, provided by a toroidal magnet permeates the muon chamber. This allows for a determination of the muon momenta.

3. The Experimental Setup

The LHC is designed for an event frequency of 40 MHz. That means if the machine is running at full capacity, around 40 million beam crossings happen per second. If all the corresponding data was recorded, one would have to store petabytes per second (one event roughly corresponds to 25 megabyte of raw data). It is obvious that this is technically impossible. Instead, ATLAS uses a sophisticated system of event-triggers that reduces the quantity of data significantly. The *Trigger and Data Acquisition* (TDAQ) system reduces the number of events down to a rate of 200 Hz. Several triggers are used to achieve this strong reduction. The first trigger (L1) filters the event rate down to 75 kHz. Consequently, the trigger has to work very fast and therefore L1 is not a software, but a hardware trigger. L1 uses information from the calorimeters and the muon spectrometer. Thereby so called *Regions of Interest* (ROI) are defined in the detector. In these regions, L1 can trigger leptons, jets, photons, or events with large or missing transverse momentum. The L1 trigger is followed by the L2 trigger, which uses information from the inner detector to further filter down the event rate to be below 3.5 kHz. Eventually, the low rate of roughly 200 Hz is achieved by the Event Filter trigger, which uses information from the full detector in order to decide if a certain event is stored or not. A visualisation of the ATLAS trigger system is given by Figure 3.2.

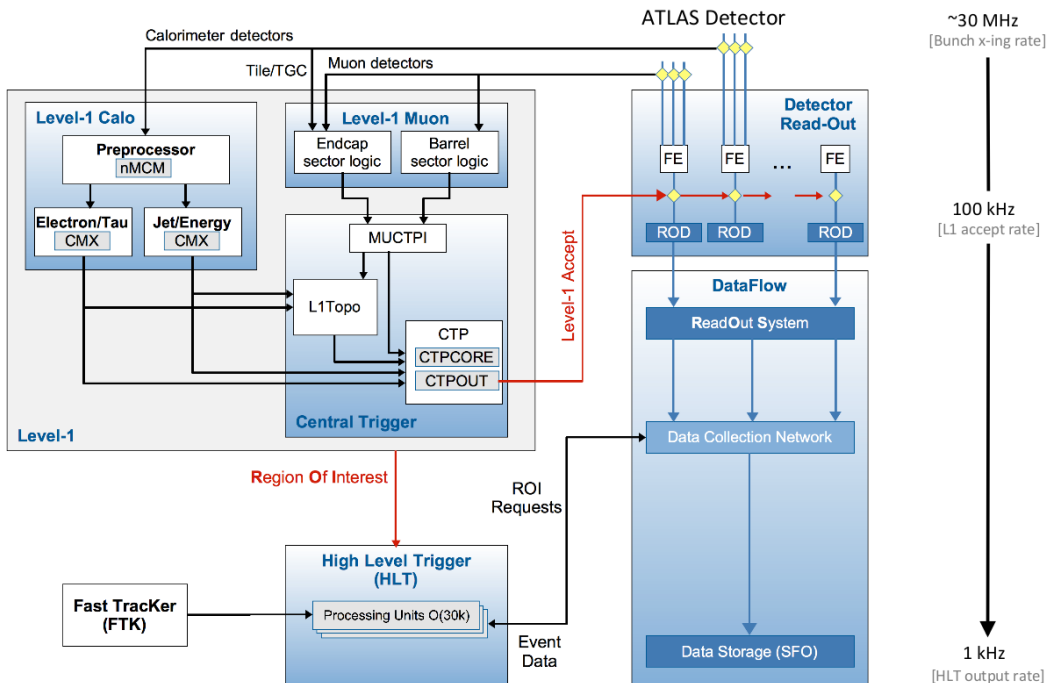


Figure 3.2.: Schematic layout of the Run-2 ATLAS trigger system.

The ATLAS Coordinate System

In order to measure the kinematics of physics objects in form of their four-momenta, some sort of coordinate system must be set up. In case of the ATLAS coordinate system, the nominal interaction point is chosen to be the origin of the system. Thereby, the x -axis points towards the central point of the LHC ring, the y -axis points upwards, and the z -axis points along the beam direction. However, at hadron colliders the incoming partons carry fractions of the total momentum of the respective hadrons and therefore the longitudinal momenta differ among the colliding partons. As a consequence, one prefers non-cartesian coordinates for the measurement of the particle momenta. In detail, one measures the energy E of a particle, its transverse momentum $p_T \equiv \sqrt{p_x^2 + p_y^2}$ and two angles ϕ and η . The angle ϕ is defined as the azimuthal angle around the beam-axis and the *pseudorapidity* η is defined as:

$$\eta = -\ln \left(\tan \left(\frac{\theta}{2} \right) \right), \quad (3.4)$$

whereby θ is the polar angle to the beam-axis. One prefers η over θ because the pseudorapidity is closely related to the *rapidity* y , which can be expressed as a function of η :

$$y = \ln \left(\frac{\sqrt{m^2 + p_T^2} \cosh^2(\eta) + p_T \sinh(\eta)}{\sqrt{m^2 + p_T^2}} \right). \quad (3.5)$$

This quantity is useful because rapidity differences, Δy , are invariant under Lorentz boosts along the longitudinal axis and in the relativistic limit of high energies or massless particles the pseudorapidity becomes equal to the rapidity. Nevertheless, as the pseudorapidity is much easier to measure than the true rapidity, η is chosen as a coordinate.

One can then set up angular separations between particles, such as $\Delta\phi \equiv |\phi_2 - \phi_1|$ and $\Delta\eta \equiv |\eta_2 - \eta_1|$, as well as the distance between two particles in the η - ϕ space $\Delta R \equiv \sqrt{(\Delta\eta)^2 + (\Delta\phi)^2}$.

Last but not least, the momentum in cartesian coordinates can be obtained via the relations:

$$p_x = p_T \cos(\phi), \quad (3.6)$$

$$p_y = p_T \sin(\phi), \quad (3.7)$$

$$p_z = p_T \sinh(\phi). \quad (3.8)$$

4. The $t\bar{t}H$ Process and the ATLAS $t\bar{t}(H \rightarrow b\bar{b})$ Search

4.1. The $t\bar{t}H$ Process and the $t\bar{t}(H \rightarrow b\bar{b})$ Process

In order to scrutinise the true nature of the scalar particle that was discovered by ATLAS and CMS in 2012, a test of the Yukawa coupling Y_t to the top quark is crucial. As mentioned earlier, a model independent analysis cannot be performed with the Higgs boson production via gluon-gluon fusion $gg \rightarrow H$ or the Higgs boson decay channel $H \rightarrow \gamma\gamma$, because the top quark is not directly observable here, although its Yukawa coupling is expected to dominate these processes. Instead, one looks at the very rare process $pp \rightarrow t\bar{t}H$, which exhibits top quark decay products in the final state [58, 59].

For some time it was not clear if the $t\bar{t}H$ process could even be measured at the LHC. The presence of three particles, the most massive within the SM, uses up a large part of the available phase space, therefore the process requires the highest (at the LHC) possible energies. Also large data samples are needed: in the 8 TeV collisions at the LHC the expected cross section was approximately 130 fb [60], which is very low. Even so, ATLAS and CMS were able to study the $t\bar{t}H$ channel in Run-I [61–63] and they provided constraints on the corresponding signal strength. Thereby, CMS did a measurement of the signal strength by combining results from $t\bar{t}(H \rightarrow \tau\tau)$, $t\bar{t}(H \rightarrow \gamma\gamma)$ and $t\bar{t}(H \rightarrow b\bar{b})$ as well as from $t\bar{t}H$ with multiple light charged leptons in the final state, and obtained $\mu = \sigma/\sigma_{\text{SM}} = 2.5^{+1.1}_{-1.0}$ [64]. In Run-II however, due to the higher COM energy and higher luminosity, more precise studies on the $t\bar{t}H$ production are possible. Both ATLAS and CMS collaborations, have, after reporting evidence [64, 65] finally observed the $t\bar{t}H$ process with combined fits from several analyses studying different Higgs boson decay modes [66, 67]. Thereby, ATLAS sees an excess of signal over the expected SM background with an observed significance of 5.8σ (4.9σ expected) using datasets collected at $\sqrt{s} = 13$ TeV. Results from several independent $t\bar{t}H$ searches such as $H \rightarrow WW^*$, $H \rightarrow ZZ^*$, $H \rightarrow \tau\tau$, $H \rightarrow b\bar{b}$ and $H \rightarrow \gamma\gamma$ were combined. The fitted $t\bar{t}H$ cross section is 670 ± 90 (stat.) $^{+110}_{-100}$ (syst.) fb assuming SM Higgs boson branching ratios and it is in agreement with the corresponding

4. The $t\bar{t}H$ Process and the ATLAS $t\bar{t}(H \rightarrow b\bar{b})$ Search

SM prediction of 507_{-50}^{+35} fb [65]. When combining the results with data from earlier runs at $\sqrt{s} = 7$ TeV and $\sqrt{s} = 8$ TeV, ATLAS observes an excess of 6.3σ (5.1σ expected) over the SM background-only hypothesis. The CMS collaboration also reported the observation of the $t\bar{t}H$ process. They combined their data, taken at 7, 8, and 13 TeV with integrated luminosities of respectively 5.1, 19.7 and 35.9 fb $^{-1}$. Several independent $t\bar{t}H$ searches such as $H \rightarrow WW^*$, $H \rightarrow ZZ^*$, $H \rightarrow \tau\tau$, $H \rightarrow b\bar{b}$ and $H \rightarrow \gamma\gamma$ were combined. This combination lead to an observed excess of 5.2σ over the background expectation [67]. From the Standard Model predictions, the expected significance was 4.2σ . Normalised to the SM prediction, CMS measures the $t\bar{t}H$ signal strength via a combined fit to be $\mu_{t\bar{t}H} = 1.26_{-0.26}^{+0.31}$ [67].

While such an observation marks an important milestone in the history of the $t\bar{t}H$ searches, the physically interesting studies (e.g. that give access to quantities like the Yukawa couplings) require observations of the individual $t\bar{t}H$ decay channels rather than observations via combined analyses. Within this study the channel $t\bar{t}(H \rightarrow b\bar{b})$ is of interest. With the dataset collected at $\sqrt{s} = 8$ TeV, ATLAS searched for $t\bar{t}$ pair production in association with a Higgs boson decaying into $b\bar{b}$ in the single lepton channel [61] and in the all-hadronic channel [68]. Thereby, ATLAS measured a combined signal strength of $\mu = 1.4 \pm 1.0$. CMS performed a similar measurement with data collected at $\sqrt{s} = 7$ and 8 TeV. They obtained a signal strength of $\mu = 0.7 \pm 1.9$ [64]. With data collected at $\sqrt{s} = 13$ TeV, ATLAS reported an observed (expected) $t\bar{t}(H \rightarrow b\bar{b})$ excess of 1.4 (1.6) standard deviations over the background-only hypothesis [69]. The signal strength is specified as $\mu = 0.84_{-0.61}^{+0.64}$ [69]. As one can conclude from that measurement, it will still take some time until this particular channel can be observed significantly.

The following sections give an overview over the current ATLAS $t\bar{t}(H \rightarrow b\bar{b})$ search. For reasons of consistency and compatibility the object definitions, event selection criteria, event reconstruction, MC samples etc. of the ATLAS search are adopted within this study.

4.2. Object Reconstruction

This analyses makes use of following physics objects for the corresponding event selection and reconstruction: electrons, muons, and jets (especially b -jets).

4.2.1. Leptons

Throughout this thesis, the term “lepton” refers to electrons or muons, unless stated otherwise.

Electrons

The candidates for electrons are built from those energy deposits in the electromagnetic calorimeter, that are related to reconstructed tracks in the Inner Detector [70]. The candidates are required to pass the *tight* identification criterion, see [71]. Thereby, shower shape and track matching observables are joined in a likelihood discriminator. Additionally, selected electrons must have at least a transverse momentum $p_T > 10 \text{ GeV}$ and $|\eta| < 2.47$. Electrons that have $1.37 < |\eta| < 1.52$ are rejected because in this η range, the ATLAS detector sees a transition between the calorimeter barrel and endcap region. The electron candidates must fulfil $|\text{IP}_z| < 0.5 \text{ mm}$ and $|\text{IP}_{r\phi}|/\sigma_{r\phi} < 5$, whereby IP_z is the longitudinal impact parameter of the electron and $|\text{IP}_{r\phi}|/\sigma_{r\phi}$ means the significance of the transverse impact parameter. These criteria ensure that the electron track is consistent with the primary vertex of the event. Furthermore, the electron must satisfy the Gradient isolation working point [71] in order to suppress non-prompt electrons (such as conversions, or electrons from hadronic decays). Last but not least, the separation of the electron candidate and the nearest selected jet must satisfy $\Delta R_y > 0.4$, where $\Delta R_y = \sqrt{(\Delta y)^2 + (\Delta \phi)^2}$ is the distance measure in y - ϕ space. This is part of an overlap-removal that aims to prevent the multiple counting of a single detector response misinterpreted as multiple leptons or jets.

Muons

Muon candidates are built from the fractional tracks detected in the different layers of the Muon Spectrometer that are associated with tracks in the Inner Detector [72]. By using the full available track information from both detector systems, the traces get fitted and finally the muon track is obtained. The candidates must satisfy $p_T > 10 \text{ GeV}$ as well as $|\eta| < 2.5$. Additionally, the muons must pass the *medium* identification working point [72] for muons and the Gradient isolation working point [72]. Furthermore, the separation of the muon candidate and the nearest selected jet must satisfy $\Delta R_y > 0.4$. In this way the background arising from hadronic decays inside of jets is suppressed. Nevertheless, if the nearest jet is related to fewer than three tracks, the jet is removed instead of the muon candidate. This is done in order to circumvent the inefficiency, that would occur for high-energetic muons, which experience a severe energy loss in the calorimeter. Finally the muon candidates must also fulfil $|\text{IP}_z| < 0.5 \text{ mm}$ and $|\text{IP}_{r\phi}|/\sigma_{r\phi} < 3$.

4. The $t\bar{t}H$ Process and the ATLAS $t\bar{t}(H \rightarrow b\bar{b})$ Search

Taus

Leptonically decaying τ leptons (τ_{lep}) are detected as electrons or muons and they are not distinguished from electrons or muons that directly originate from the corresponding W^\pm decay.

However, τ leptons that decay hadronically (τ_{had}) are differentiated from jets with, firstly, the track multiplicity and, secondly, a multivariate classifier. The latter in turn takes kinematic information, the track collimation and the jet substructure into account [73]. Selected τ_{had} particles must satisfy the *medium* τ -identification working point [73] and their transverse momentum p_T must be above 25 GeV. Additionally, a pseudorapidity of $|\eta| < 2.5$ is required. Finally, a τ_{had} candidate can only be selected if there is no selected electron or muon within a radius of $\Delta R_y < 0.2$ with respect to the τ_{had} candidate.

4.2.2. Jets

The three dimensional topological energy clusters [74] in the calorimeter are used for the reconstruction of jets. Thereby, the jet candidates are built via FastJet [75] using the anti- k_t algorithm [76]. The corresponding radius parameter is set to 0.4 [69]. Subsequently, the jets are calibrated to the jet energy scale [77]. Afterwards, a reconstructed jet must have $p_T > 25$ GeV and $|\eta| < 2.5$ otherwise it is rejected. The jet candidates undergo an additional *jet cleaning procedure*. This procedure is about identifying jets that do not originate from the collision [78]. If such a jet is found, the corresponding event is rejected. In order to suppress jets originating from secondary proton-proton interactions (pile up), the jet vertex tagger (JVT) [79] is used. This algorithm is applied to jets with $p_T < 60$ GeV and $|\eta| < 2.4$ in order to test their consistency with the primary vertex. The separation of a jet and a selected electron must be $\Delta R_y < 0.2$, otherwise the jet is rejected.

B-Tagging

For this analysis it is of great importance that jets originating from the bottom quarks, which again stem from the top quark decay, are distinguished from jets of a different origin. For this purpose of tagging these jets containing B -hadrons, a multivariate algorithm, called *MV2c10* is used, which combines different kinds of information such as data related to topological properties of secondary and tertiary decay vertices found within the jet or information based on the impact parameters of displaced tracks [80, 81]. The MV2c10 algorithm is trained on simulated $t\bar{t}$ events and optimised to separate b -jets from c -jets, light jets, gluon jets, and hadronically decaying τ leptons.

The obtained b -tagging information can be used in various ways. One would be to choose a certain b -tagging working point (WP) corresponding to a desired b -tagging efficiency and select jets based on the tagger weight at the chosen WP. Four different working points are defined, which are called *loose* (85 % efficiency), *medium* (77 %), *tight* (70 %), and *very tight* (60 %). The mentioned efficiencies refer to b -jets with $p_T > 20$ GeV (in simulated $t\bar{t}$ events) passing or not passing the corresponding working point. This analysis, however, makes use of the entire b -tag weight distribution provided by the MV2c10 tagger. The distribution is subdivided into five bins related to the defined WPs and the edge points that are interpreted as WPs at 100 % and 0 % efficiency. This method is named *pseudo-continuous b-tagging*. Instead of classifying a jet as tagged or not tagged using a single WP, the pseudo-continuous approach allows for a finer distinction between the jets: a b -tag discriminant is set up, that separates jets into five classes corresponding to the tightest WP they pass. Thereby, a value of one is assigned to a jet not passing any of the defined WPs and a value of five is assigned to a jet passing the *very tight* criterion. The b -tag discriminant is then later used for the categorisation and classification of events.

Large Radius Jets

In the case of boosted events, with at least one boosted Higgs candidate with high transverse momentum (boosted) of $p_T > 200$ GeV and a boosted top candidate of $p_T > 250$ GeV, jets with a large radius are formed from the selected jets [82]. Consequently, the anti- k_t algorithm is used with a radius parameter $R = 1.0$. Even though in this study the large- R jets as defined by the ATLAS $t\bar{t}(H \rightarrow b\bar{b})$ search are not considered, they should be mentioned here for the sake of completeness.

4.2.3. Missing Transverse Energy

The missing transverse energy (E_T^{Miss}) is calculated from the negative vector sum of the transverse momenta of all the leptons and jets that pass the selection in a certain event. An extra term is added, calculated from additional tracks in the inner detector that match the primary vertex [83]. This extra term describes the missing transverse momentum that is not directly associated with the leptons and jets [84, 85]. Although the event selection does not make demands with regards to missing transverse momentum in an event, it is still an important quantity for the event reconstruction.

4.3. Monte Carlo Modelling

This analysis is a study of MC generated simulations. For consistency, the MC samples and event selections (as described in the following sections) of the ATLAS $t\bar{t}(H \rightarrow b\bar{b})$ search [69] were also used here.

In both, the signal and the background samples relevant to the reconstruction level studies within this analysis, a full simulation of the ATLAS detector [86], built on GEANT4 [87] was implemented. All events were simulated for a centre-of-mass energy of $\sqrt{s} = 13$ TeV.

4.3.1. Signal

In the simulations, the top quark mass is set to $m_t = 172.5$ GeV and the Higgs boson mass is set to $m_H = 125$ GeV. None of the Higgs boson decay modes were ignored and the corresponding branching fractions were obtained with HDECAY [88]. The $t\bar{t}H$ cross section of 507_{-50}^{+35} fb was calculated in [89–94] including the corrections from next-to-leading order (NLO) QCD and electroweak effects. Different $t\bar{t}H$ signal samples were generated, however within the default one, the $t\bar{t}H$ matrix element was calculated with the POWHEG-BOX v2 NLO generator [95–98] (in the following referred to as POWHEG) at next-to-leading order in QCD. The parton shower and hadronisation were performed using PYTHIA 8.210 [99, 100] with the A14 tune [101]. The parton distribution function NNPDF3.0ME [102] was used. The renormalisation and factorisation scales were set to an equal value: $\mu_R = \mu_F = H_T/2$. Thereby $H_T = \sum_i \left(\sqrt{p_T^2 + m^2} \right)_i$ is the sum over the final state particle transverse masses. MADSPIN [103] was used for the top quark decays and all spin correlations were preserved. The decays of b - and c -hadrons are modelled with EVTGEN v1.2.0 [104].

Additionally, alternative signal samples were generated, using MADGRAPH5_aMC@NLO (version 2.3.2) [105] for the $t\bar{t}H$ matrix element calculation at NLO in QCD. The parton shower was then performed using PYTHIA 8.210 with the A14 tune and for a second sample, using HERWIG 7.0 [106].

For the purpose of studying the $t\bar{t}H$ coupling with a CP-odd or CP-mixed Higgs boson, non-SM MC samples, one with a CP-odd coupling and one with maximum mixing ($\cos(\alpha) = 45^\circ$, see Chapter 6) were generated using MADGRAPH5_aMC@NLO (version 2.6.0) interfaced with PYTHIA 8.230. The UFO model [107] as described in [108] was used. These samples do not contain the full ATLAS reconstruction information and are therefore used for particle level studies.

4.3.2. The $t\bar{t}$ Backgrounds

Similar to the nominal signal sample, the default $t\bar{t}$ background was generated at NLO in QCD using POWHEG interfaced with PYTHIA 8.210 for the parton showering. The A14 tune [101] and the parton distribution function NNPDF3.0NLO [102] were used. The $t\bar{t}$ cross section was calculated with TOP++2.0 [31]. Thereby, the obtained value of 832_{-51}^{+46} pb includes the next-to-next-to-leading order (NNLO) corrections in perturbative QCD and the next-to-next-to-leading-logarithmic (NNLL) soft gluon contributions [109–112]. The parameter h_{damp} is set to $1.5 m_t$ [113]. This parameter describes the transverse momentum of the first NLO gluon emission. The renormalisation and factorisation scales were set to an equal value: $\mu_R = \mu_F = m_t^T$. The transverse top quark mass m_t^T is thereby defined as $m_t^T = \left(\sqrt{(p_t^{T*})^2 + m_t^2} \right)$, whereas p_t^{T*} means the transverse momentum of the top quark within the $t\bar{t}$ centre-of-mass frame.

Alternative $t\bar{t}$ samples were generated at NLO in QCD with SHERPA [114] (version 2.1.1) using the ME+PS@NLO setup and OPENLOOPS [115]. The NNPDF3.0NNLO parton distribution function was used and the renormalisation and factorisation scales were set to $\mu_R = \mu_F = \sqrt{0.5 \left((m_t^T)^2 + (m_{\bar{t}}^T)^2 \right)}$.

In order to divide the $t\bar{t}$ +jets background into the different flavour categories, the following procedure is applied [69]: at first, generator level jets are constructed from particles with a mean lifetime $\tau > 3 \cdot 10^{-11}$ s with the anti- k_t algorithm using $R = 0.4$. These jets are required to have $p_T > 15$ GeV and $|\eta| < 2.5$. Subsequently, the numbers of B - or C -hadrons satisfying $\Delta R < 0.4$ with regards to the respective jet axis are counted. If a jet contains one B -hadron it is denoted as a b -jet. If more than one B -hadron matches with one jet, that jet is labelled B -jet. Jets containing C -hadrons are named in an analogous manner. Events are then divided into the categories $t\bar{t}+ \geq 1b$, $t\bar{t}+ \geq 1c$ and $t\bar{t}$ +light jets, depending on whether they have at least one b - or B -jet, c - or C -jet, or no heavy flavour jets respectively. The heavy flavour jets originating from the top quark or W boson decay are disregarded.

To maximise the precision of the $t\bar{t}$ background modelling, the $t\bar{t}+ \geq 1b$ events are subdivided into $t\bar{t} + b$, $t\bar{t} + b\bar{b}$, $t\bar{t}+ \geq 3b$ and $t\bar{t} + B$ depending on the number of b - or B -jets respectively. These categories are then scaled according to a $t\bar{t} + b\bar{b}$ sample generated at NLO with SHERPA [114] (version 2.1.1) and the CT10 four flavour scheme (4F) PDF [116]. The SHERPA sample delivers a precise description of the $t\bar{t} + b\bar{b}$ process and the bottom quark kinematics, that also take the bottom quark mass into consideration [69].

4.3.3. Other Backgrounds

The $t\bar{t}V$ ($V \in \{Z, W^\pm\}$) and non- $t\bar{t}$ background are taken into account for the total background prediction. However, they will only briefly be introduced here since, due to their small contribution, these backgrounds are not considered in the studies on angular distributions performed within this analysis.

MADGRAPH5_aMC@NLO interfaced with PYTHIA 8.210 was used to generate $t\bar{t}W$ and $t\bar{t}Z$ samples. The Wt and s-channel single top samples were produced using POWHEG-BOX v1 interfaced with PYTHIA 6.428 [117]. The W +jets and Z +jets samples were generated using SHERPA 2.2.1. Further, tWH samples were produced using MADGRAPH5_aMC@NLO interfaced with HERWIG 7.0. Single top events in association with a Higgs boson and jets were produced using MADGRAPH5_aMC@NLO interfaced with PYTHIA 8.210. Finally, four top events $t\bar{t}t\bar{t}$, diboson events in association with a top quark pair ($t\bar{t}WW$), tZ events and tZW events were generated using MADGRAPH5_aMC@NLO interfaced with PYTHIA 8.210 or PYTHIA 6.428 in case of tZ .

4.4. Event Selection

Single lepton triggers were used in order to record single lepton events, as well as dilepton events. Events must either satisfy a trigger with a low lepton p_T threshold and an additional lepton isolation criterion or one with a higher lepton p_T threshold at a looser identification working point and without an additional lepton isolation criterion. For 2015 (2016) data, the low p_T thresholds are 24 GeV (26 GeV) in case of electrons and 20 GeV (26 GeV) in case of muons.

Single Lepton Channel

In the lepton + jets channel, selected events have exactly one isolated lepton with $p_T > 27$ GeV and no other leptons with a transverse momentum above $p_T > 10$ GeV. Events are rejected if they contain more than one hadronic τ candidate. At least five jets are required. In cases of events with exactly five jets, at least three b -tagged jets at the *medium* working point are required. In cases of single lepton events with six or more jets, two jets must be b -tagged at the *very tight* working point or three of them must satisfy the *medium* b -tagging working point.

Dilepton Channel

The dilepton channel requires exactly two leptons with opposite charge. Thereby, the leading lepton must have $p_T > 27$ GeV and the subleading lepton is required to have $p_T > 15$ GeV in the ee channel and $p_T > 10$ GeV for the $e\mu$ or $\mu\mu$ channel. The channels with same-flavour leptons have the following requirements for the invariant mass of the lepton system: $m_{ll} > 15$ GeV and $m_{ll} \notin [83-99]$ GeV. With the latter requirement, it is ensured that the leptons do not come from an on-shell Z boson decay. In the $e\mu$ channel this requirement is not necessary because the Z boson does not mix flavours. No hadronically decaying τ candidates are allowed in the dilepton channel in order to preserve orthogonality to other analyses. The dilepton channel requires at least three jets, of which at least two are b -tagged at the medium working point. Events must have four or more jets in order to enter the signal regions as explained in the following section.

4.4.1. Event Categorisation

The events that pass the described event selection are manifold. They are clearly dominated by $t\bar{t}$ +jets background, however, only some parts of the selected phase space see events with a large b -jet component ($t\bar{t}(H \rightarrow b\bar{b})$, $t\bar{t}+ \geq 1b$). Others in turn show a low b -jet contribution but are highly enriched in $t\bar{t}+ \geq 1c$ or $t\bar{t}$ +light jets content. Categorising the whole event sample into smaller, non-overlapping samples, referred to as *regions*, helps to control the different background contents. Thereby, one differentiates between *signal-enriched regions* (signal regions, SR), that contain a signal-to-background ratio¹ of $S/B > 1\%$ and $S/\sqrt{B} > 0.3$, and *signal-depleted regions* that mainly consist of backgrounds and have little signal contribution (referred to as control regions, CR). While the signal regions provide sensitivity to the $t\bar{t}(H \rightarrow b\bar{b})$ signal, the control regions help to constrain the systematic uncertainties of the background and therefore enhance the background prediction in the signal regions. Given these constraints, the sensitivity of a combined fit, as performed in the ATLAS $t\bar{t}(H \rightarrow b\bar{b})$ search [69], is improved.

The events are classified according to the number of jets and the corresponding values of the b -tagging discriminant of the individual jets.

Single Lepton Channel

In the single lepton channel, the event sample is split up into events containing exactly five and more than five jets. Events with five jets are separated into two signal regions

¹Hereby, S means the expected number of $t\bar{t}(H \rightarrow b\bar{b})$ signal events with a SM Higgs boson, $m_H = 125$ GeV and B denotes the expected number of corresponding background events.

4. The $t\bar{t}H$ Process and the ATLAS $t\bar{t}(H \rightarrow b\bar{b})$ Search

SR_1^{5j} , SR_2^{5j} and three control regions $CR_{t\bar{t}+\text{light}}^{5j}$, $CR_{t\bar{t}+\geq 1c}^{5j}$, $CR_{t\bar{t}+b}^{5j}$. Thereby SR_1^{5j} is an ultra-pure signal region that requires at least four b -tags at the *very tight* working point, whereby “ultra-pure” in this case means a S/B ratio of approximately 5%. In this region, the $t\bar{t} + \geq 2b$ background contribution makes up at least 60% of the total background. The $CR_{t\bar{t}+b}^{5j}$ region merges the remaining b -tagging discriminant categories with a $t\bar{t} + 1b$ content of at least 20% with respect to the total background.

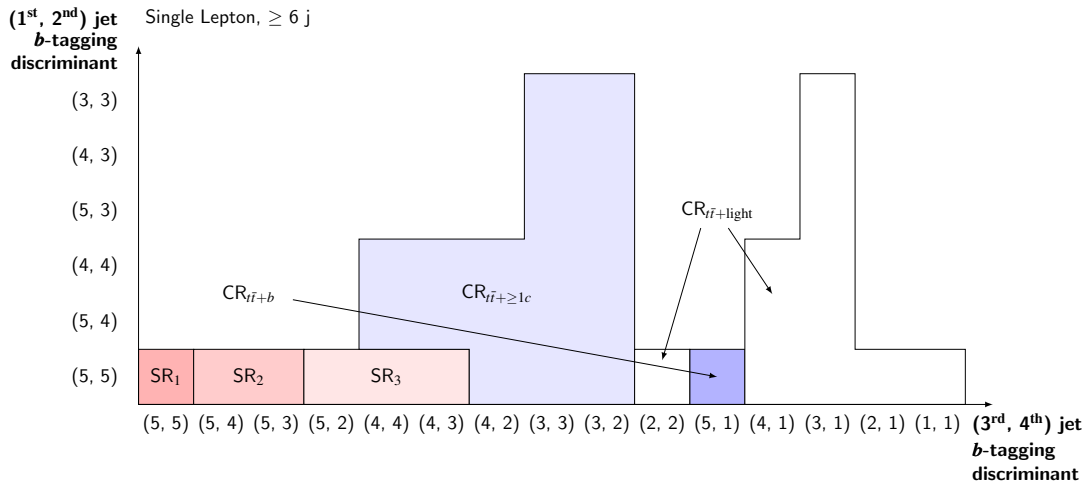
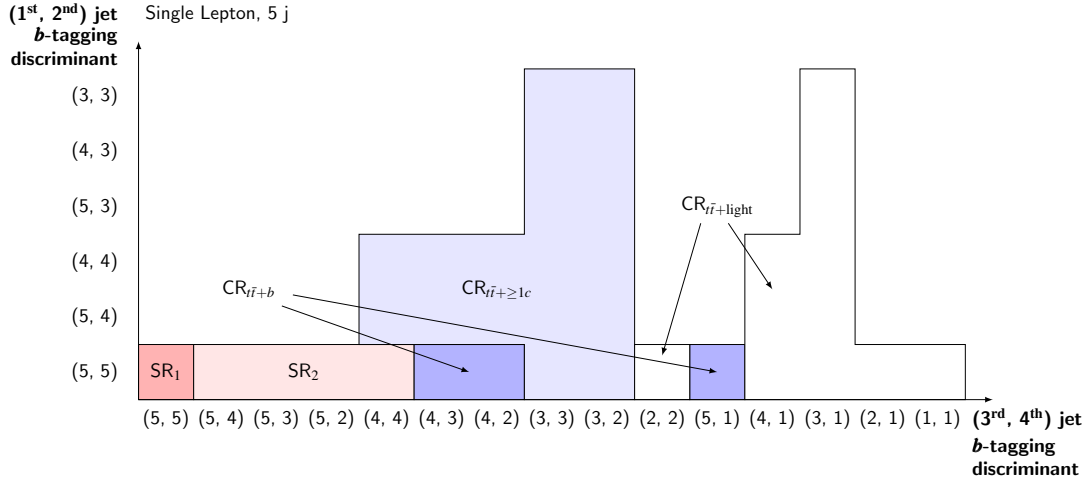
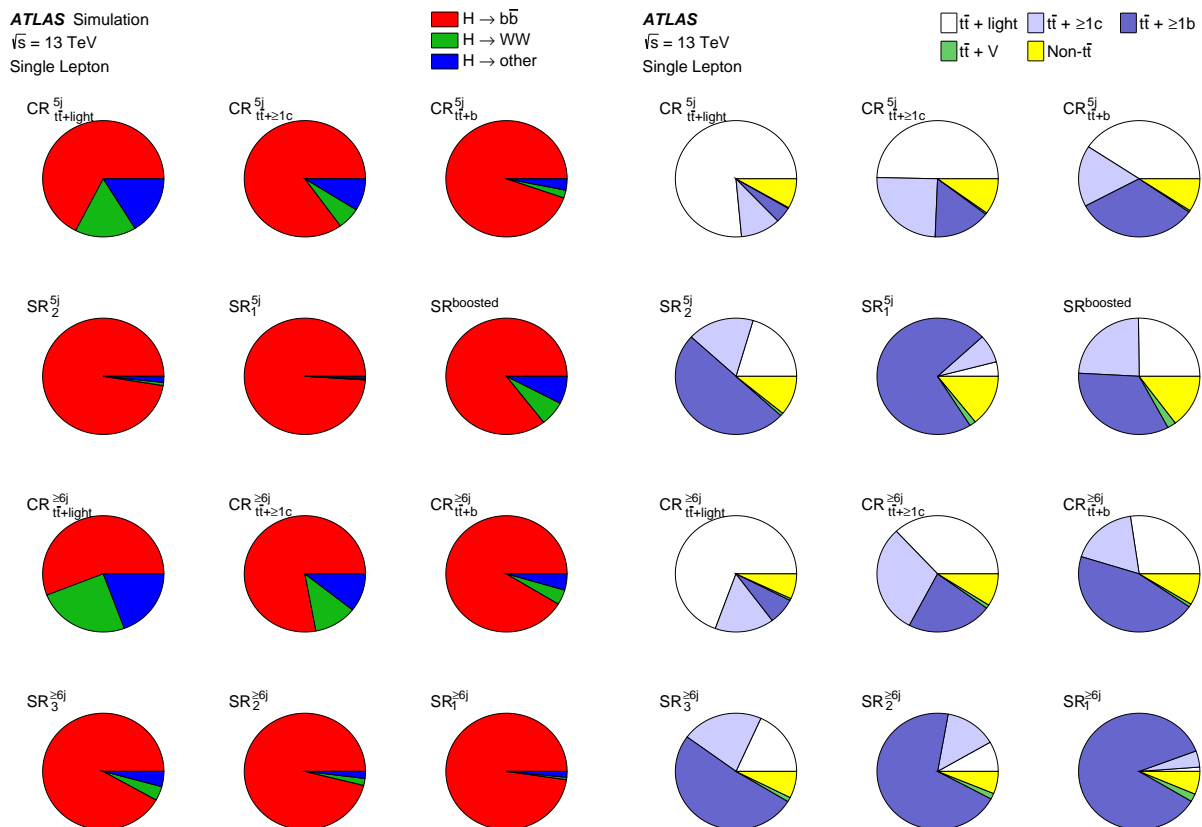


Figure 4.1.: The signal and control regions in the single lepton channel with exactly five (a) and more than five jets (b) [69]. On the vertical axis, the values of the b -tagging discriminant for the first two jets are shown and on the horizontal axis, the values for the third and fourth jets are shown.

The second signal region SR_2^{5j} requires four b -tagged jets and either at least three passing

the *very tight* and one passing the *loose* criterion or at least two passing the *very tight* and two passing the *tight* working point. The SR_2^{5j} contains all remaining categories with at least 20% $t\bar{t} + \geq 2b$ content. The region $\text{CR}_{t\bar{t} + \geq 1c}^{5j}$ then contains all the categories left with a $t\bar{t} + \geq 1c$ contribution of at least 20% and all remaining events with 5 jets are merged in the $\text{CR}_{t\bar{t} + \text{light}}^{5j}$ category. Figure 4.1 (a) visualises how the signal and control regions emerge from the b -tagging discriminant values of the first four jets (ordered in decreasing order related to their b -tagging discriminant value).



(a) Signal composition.

(b) Background composition.

Figure 4.2.: Contribution from various Higgs boson decay modes to the $t\bar{t}(H \rightarrow b\bar{b})$ signal (a) in the single lepton channel for each analysis category. The contributions from the different backgrounds to the total background prediction in the single lepton channel is shown in (b) for each category [69].

Single lepton events with more than five jets are divided into three signal regions $\text{SR}_1^{\ge 6j}$, $\text{SR}_2^{\ge 6j}$, $\text{SR}_3^{\ge 6j}$ and three control regions $\text{CR}_{t\bar{t} + \text{light}}^{\ge 6j}$, $\text{CR}_{t\bar{t} + \ge 1c}^{\ge 6j}$, $\text{CR}_{t\bar{t} + b}^{\ge 6j}$. Just like SR_1^{5j} , $\text{SR}_1^{\ge 6j}$ is considered an ultra-pure signal region and requires four b -tagged jets at the *very tight*

4. The $t\bar{t}H$ Process and the ATLAS $t\bar{t}(H \rightarrow b\bar{b})$ Search

working point. The remaining b -tagging discriminant categories with more than 45% $t\bar{t}+ \geq 2b$ content are joined in $\text{SR}_2^{\geq 6j}$. Afterwards, categories that show a $t\bar{t}+ \geq 2b$ content of more than 30% are merged in $\text{SR}_3^{\geq 6j}$. The remaining categories are merged into the control regions, namely into $\text{CR}_{t\bar{t}+b}^{\geq 6j}$ for all categories with a $t\bar{t}+ 1b$ contribution of more than 30% and the remaining categories with a $t\bar{t}+ \geq 1c$ content of at least 30% are classified into $\text{CR}_{t\bar{t}+\geq 1c}^{\geq 6j}$. The leftover events are categorised as $\text{CR}_{t\bar{t}+\text{light}}^{\geq 6j}$. The signal and control regions in the single lepton channel with six or more jets are visualised in Figure 4.1 (b) as a function of the b -tagging discriminant values of the individual jets. Figure 4.2 shows the different signal and background compositions for all regions in the single lepton channel. Thereby, the signal events “ $H \rightarrow \text{other}$ ” are mainly $H \rightarrow \tau^+\tau^-$ and $H \rightarrow ZZ^*$. In case of the backgrounds, $t\bar{t}+V$ refers to the background arising from the $t\bar{t}W$ and $t\bar{t}Z$ production. The “Non- $t\bar{t}$ ” background is composed of Wt , s -channel single top, W/Z +jets and tH +jets production that are all estimated using respective MC simulations [69]. Additionally, the background from fake leptons in the single lepton channel is estimated using a data driven technique [69]. The $t\bar{t}$ +jets background is divided into the individual flavour components as described in Section 4.3.2.

Dilepton Channel

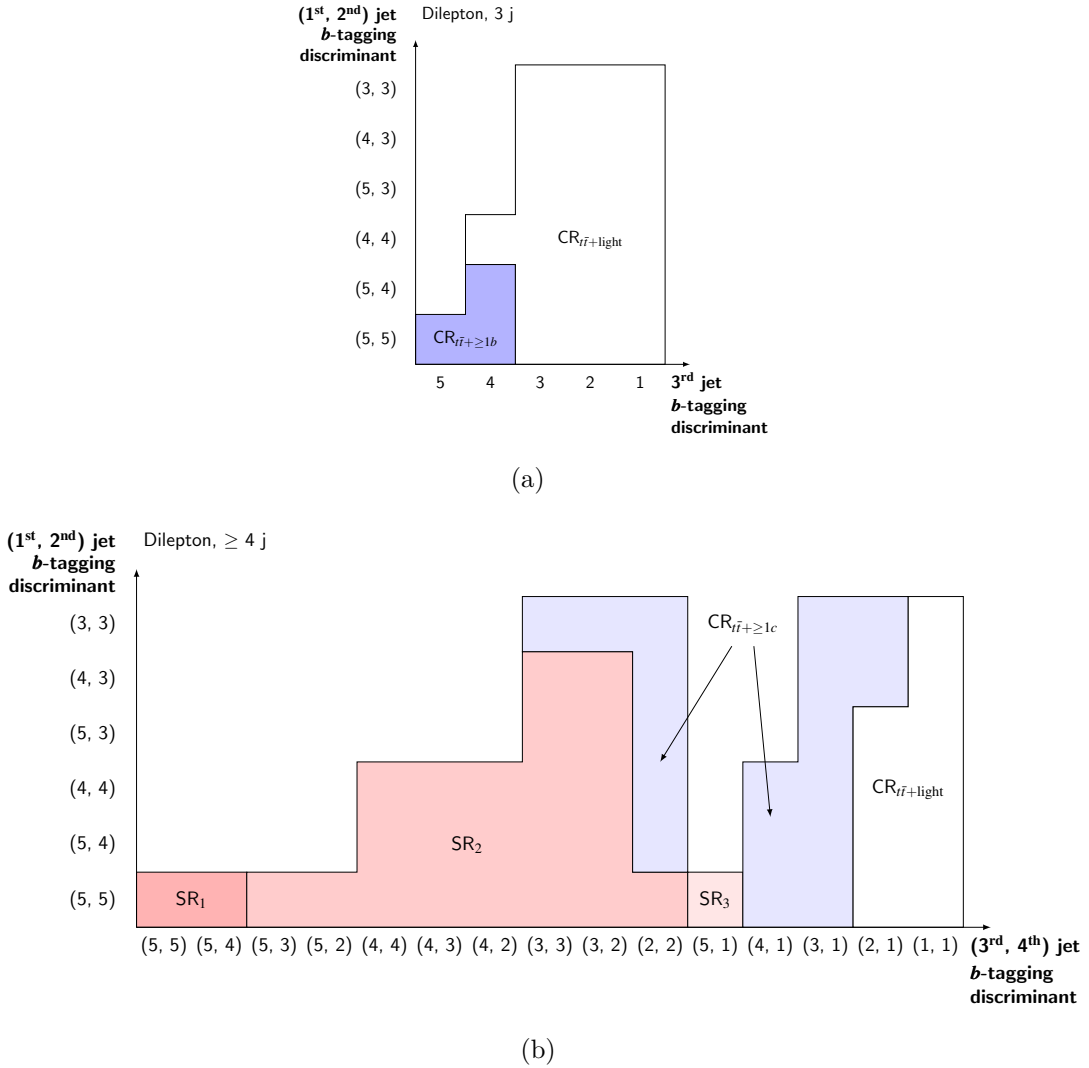


Figure 4.3.: The control regions in the dilepton channel with exactly three jets (a) and the respective signal and control regions with more than three jets [69]. On the vertical axis, the values of the b -tagging discriminant for the first two jets are shown and on the horizontal axis, the values for the third (and fourth in case of (b)) jet are shown.

The selected dilepton events are divided into two subsets, one with the events containing exactly three jets and the other with the events having four or more jets. As shown in Figure 4.3 (a), the sample with exactly three jets is further subdivided into two control regions $CR_{t\bar{t}+\ge 1b}^{3j}$ and $CR_{t\bar{t}+light}^{3j}$, enriched in $t\bar{t}+\ge 1b$ (contribution at least 30%) and $t\bar{t}+light$ jets (remaining three jet events), respectively.

The events with four or more jets are classified into three signal regions $SR_1^{\ge 4j}$, $SR_2^{\ge 4j}$,

4. The $t\bar{t}H$ Process and the ATLAS $t\bar{t}(H \rightarrow b\bar{b})$ Search

$SR_3^{\geq 4j}$ and two control regions $CR_{t\bar{t}+\text{light}}^{\geq 4j}$ and $CR_{t\bar{t}+\geq 1c}^{\geq 4j}$. Thereby, $SR_1^{\geq 4j}$ requires at least three b -tags at the *very tight* and at least one b -tag at the *tight* working point. In this way $SR_1^{\geq 4j}$ has a $t\bar{t}+\geq 2b$ content of at least 70%. The region $SR_3^{\geq 4j}$ is then built from the remaining categories with at least 30% $t\bar{t}+1b$ contribution. The other categories with a signal content of at least 1.5% are joined in $SR_2^{\geq 4j}$. The remaining categories with a $t\bar{t}+\geq 1c$ content of at least 25% are grouped in $CR_{t\bar{t}+\geq 1c}^{\geq 4j}$. Finally the left over events are merged in $CR_{t\bar{t}+\text{light}}^{\geq 4j}$. The different analysis regions with four or more jets are plotted in Figure 4.3 (b) as a function of the b -tag discriminant value of the jets.

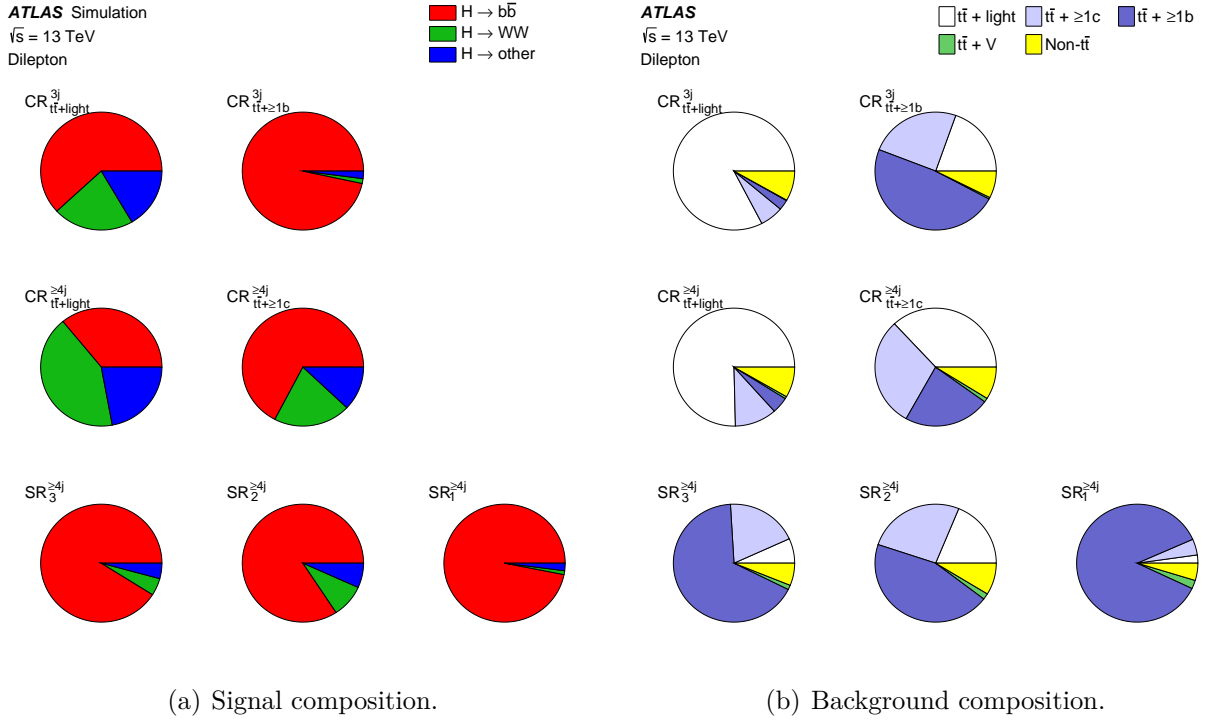


Figure 4.4.: Contribution from various Higgs boson decay modes to the $t\bar{t}(H \rightarrow b\bar{b})$ signal (a) in the dilepton channel for each analysis category. The contributions from the different backgrounds to the total background prediction for each category in the dilepton channel is shown in (b) [69].

The different compositions of the predicted SM signal and total background are presented in Figure 4.4 for all analysis regions in the dilepton channel. Thereby the “Non- $t\bar{t}$ ” contribution consists of the same background contents as described for the single lepton channel, however, without the data driven fake lepton estimation. The corresponding signal-to-background ratios S/B and S/\sqrt{B} after event selection and categorisation are shown in Figure 4.5 for the single lepton channel (a) and the dilepton channel (b), respectively for each defined region. The most sensitive signal regions SR_1^{5j} , $SR_1^{\geq 6j}$ and $SR_1^{\geq 4j}$ see a S/B

ratio of around 4-5 %.

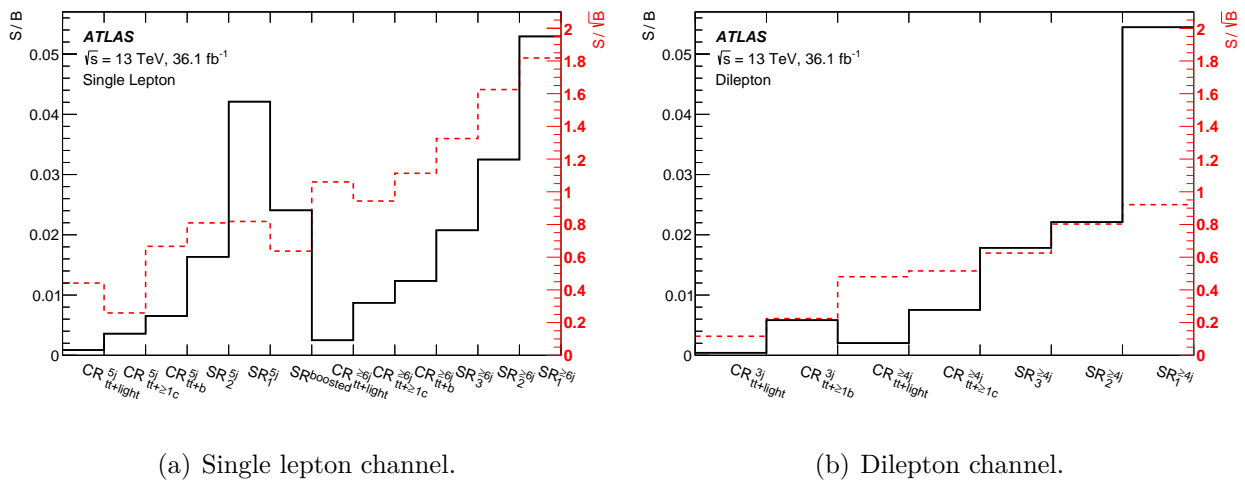


Figure 4.5.: S/B and S/\sqrt{B} ratios as a function of the different analysis regions in the single lepton channel (a) and the dilepton channel (b) [69].

4.5. Event Reconstruction

4.5.1. Reconstruction BDT

As one has seen from the right Feynman diagram (b) in Figure 2.7, the $t\bar{t}(H \rightarrow b\bar{b})$ final state is complex. Even if all the b -jets can be identified and separated from light jets, the reconstruction will suffer from a combinatorial background, that arises from wrong assignments of the b -jets to the top quark or Higgs boson. For the purpose of reconstructing the $t\bar{t}(H \rightarrow b\bar{b})$ events, *Boosted Decision Trees* (BDTs) were trained with TMVA [118] and applied in all single and dilepton signal regions [69]. These reconstruction BDTs separate between correct and incorrect jet and lepton assignments by making use of invariant masses and angular separations or kinematic variables of the $t\bar{t}(H \rightarrow b\bar{b})$ signal. Thereby, the BDT signal is the correct assignment of jets to the final state particles and the BDT background consists of all the possible wrong combinations. In order to define the correct combination for the BDT training, a truth matching procedure is applied to the reconstructed jets. For this purpose the jets are related to quarks from the hard scatter event when they fulfil a geometric matching criterion of $\Delta R < 0.3$ between the quark and the jet four-momenta. A jet can only be matched to one parton. Leptons are not truth matched because they can be assigned correctly in almost all cases.

Two different kinds of BDTs are used. One with and one without kinematical information on the Higgs boson. While the former delivers a worse reconstruction efficiency (the

4. The $t\bar{t}H$ Process and the ATLAS $t\bar{t}(H \rightarrow b\bar{b})$ Search

Higgs boson gets correctly reconstructed only in 32% of the cases), the BDT with Higgs information (correct reconstruction in 48% of single lepton and 49% of dilepton events) biases the $t\bar{t} + b\bar{b}$ background towards the signal expectation. This can (but does not necessarily have to) lead to a decrease in the S/B separation power of certain observables, as shown in the next chapter. The exact definitions of the input variables are listed in the Appendix in Table A.1.

Single Lepton Channel

In the single lepton channel with exactly five jets, around 68% of the selected events have all b -jets truth matched. In events with more than five jets, around 80% get truth matched. In 55% (42%) of the events all involved jets get truth matched in the five jet (more than five jet) region, with the latter number being lower since more jets are involved. These fractions correspond to the highest achievable reconstruction efficiency assuming an optimal identification of jets.

The reconstruction BDT then builds top, W and Higgs candidates from combinations of the reconstructed lepton and jets. Hundreds of jet permutations are possible in events with more than six jets. To reduce the number of permutations, b -quarks can only be assigned to b -tagged jets. Thereby, the jets are ordered according to their b -tagging discriminant value and the four highest ranked jets are taken as b -jets.

The permutation with the highest BDT output is chosen to give the best candidates. While the p_x and p_y components of the neutrino four-momentum, needed for the reconstruction of the leptonically decaying W boson, can directly be calculated from the measured missing transverse momentum, the neutrino p_z component has to be calculated via the relation $m_W^2 = \sqrt{P_l^2 + P_\nu^2}$. Thereby P_l and P_ν are the four-momenta of the charged lepton and the neutrino respectively. Solving this equation gives:

$$p_z^{\nu\pm} = \frac{1}{2} \left(\frac{p_z^l \beta \pm \sqrt{\delta}}{E_l^2 - (p_z^l)^2} \right). \quad (4.1)$$

Here, β is defined as

$$\beta = m_W^2 - m_l^2 + 2 p_x^l p_x^\nu + 2 p_y^l p_y^\nu \quad (4.2)$$

and δ is given by

$$\delta = E_l^2 \left(\beta^2 + (2 p_z^l p_T^\nu)^2 - (2 E_l p_T^\nu)^2 \right). \quad (4.3)$$

The best working solution (positive or negative discriminant) is chosen, however if no real solution exists, which can occur for example in the case of an off-shell W boson, δ is set equal to zero in order to obtain a real solution. This happens in about 20% of

the events. The hadronically decaying W boson is reconstructed by a combination of two non b -tagged jets. However, in events with only five jets, the hadronic W boson is not reconstructed. Instead, the corresponding top quark is reconstructed by a combination of a b -jet and a light jet. Otherwise, the top quark is reconstructed from a W boson and a b -jet. The remaining b -jets are then used for the Higgs boson reconstruction.

Dilepton Channel

In the dilepton channel, the reconstruction follows the same procedure as in the single lepton channel, however the algorithm is simpler because of the lower jet multiplicity, resulting in fewer permutations that have to be tested. Furthermore, in the previous ATLAS $t\bar{t}(H \rightarrow b\bar{b})$ search [69] no attempt was made to reconstruct the W bosons in the analysis, which lead to a simple reconstruction whereby the “top quarks” were built just from a lepton and a b -jet. However, by now the dilepton samples feature a full event reconstruction via the ν -weighting method, first applied in [40]. The benefits of this enhanced reconstruction procedure are also explored within this study.

4.5.2. Likelihood Discriminant

Similar to the reconstruction BDT, a likelihood discriminant (LHD) based on different probability density functions (pdfs) built from invariant masses, angular separations and E_T^{Miss} , was set up in the single lepton channel [69]. The product of these individual pdfs then provides the probabilities p^{sig} and p^{bkg} for the signal and background hypotheses. The LHD is defined as the ratio of p^{sig} and the sum $p^{\text{sig}} + p^{\text{bkg}}$.

4.5.3. Matrix Element Discriminant

In the single lepton channel, a matrix element discriminant (MEM_{D1}) is calculated from signal and background likelihoods (\mathcal{L}_S and \mathcal{L}_B) via: $\text{MEM}_{D1} = \log_{10}(\mathcal{L}_S) - \log_{10}(\mathcal{L}_B)$ [69]. Thereby, the signal and background likelihoods, representing the order of consistency between an event and a signal or background hypothesis, are calculated from the $t\bar{t}(H \rightarrow b\bar{b})$ and $t\bar{t} + b\bar{b}$ matrix elements. This procedure is computationally so time-consuming that it is only applied in the most sensitive region, $\text{SR}_1^{\geq 6j}$.

4.6. Multivariate Event Classification

The events ending up in the previously defined signal regions are further classified as “signal” or “background” events with the help of a classification BDT. This BDT makes use of kinematic variables, angular separations as well as b -tagging information, event shape variables and outputs from the multivariate methods, such as the reconstruction BDT response and the LHD. The input variables vary for the single and the dilepton channel and within this study the performance of the corresponding classification BDTs is optimised with the help of additional angular observables.

Classification BDT input variables that are built entirely from b -tagged jets use different b -tagging requirements. In single lepton events, the four leading jets in terms of the b -tagging discriminant values are chosen to be the b -jets. In the case of two jets sharing the same b -tagging discriminant bin, they are ordered after p_T in a decreasing order. In the dilepton channel the ordering after the b -tagging discriminant is not used, instead the *tight*, *loose* and *very tight* working points are used in the regions $\text{SR}_1^{\geq 4j}$, $\text{SR}_2^{\geq 4j}$ and $\text{SR}_3^{\geq 4j}$, respectively.

The training and application of the classification BDT is performed via the TMVA package. Thereby, an exclusive training on the individual regions does not outperform an inclusive training if some b -tagging information is provided as an input for the BDT. For simplicity the BDT is therefore trained inclusively.

The list of input variables for the ATLAS $t\bar{t}(H \rightarrow b\bar{b})$ classification BDT is presented in the Appendix in Table A.2 (Table A.3) for the single lepton (dilepton) channel.

5. Analysis of Angular Distributions in the $t\bar{t}(H \rightarrow b\bar{b})$ Channel

As already mentioned, it will still take some time until the particular channel $t\bar{t}(H \rightarrow b\bar{b})$ can be observed. Large backgrounds and challenging systematic uncertainties make the $t\bar{t}(H \rightarrow b\bar{b})$ search very difficult. The dominating background is represented by $t\bar{t} + \text{jets}$, and in particular the irreducible component, $t\bar{t} + b\bar{b}$ is challenging. Without cuts the signal-to-background ratio lies in the order of 10^{-3} , and even with a sophisticated event selection the ratio is not better than approximately 0.05 in the purest signal regions [69, 83]. Without doubt, one would like to enhance the signal-to-background ratio as much as possible in order to get sensitive to the interesting physical quantities in future studies. In that manner, this analysis aims to improve the S/B ratio in the $t\bar{t}(H \rightarrow b\bar{b})$ channel by making use of spin structures that manifest themselves in angular distributions of $t\bar{t}H$ decay products. In the case of $t\bar{t}H$ angular distributions, $t\bar{t}$ spin correlations are expected to have a heavier impact on the distributions than the NLO QCD corrections [103, 119]. As already stated in the previous chapters, the top quark transfers its spin properties to its decay products due to the short top quark lifetime. Thereby, the down-type fermions from the W boson decay show the maximal spin-analysing power because they have the highest spatial correlation with the top quark spin quantisation axis [120, 121]. As described in Chapter 2.4, the top quark spins are correlated at the LHC. For very high invariant masses $m_{t\bar{t}} \gg m_t, m_{\bar{t}}$ (or in the top quark chiral limit), $t\bar{t}$ pairs are produced in the $LR+RL$ helicity configuration, because the production via unlike-helicity gluons will dominate in the high energy region. One could now ask how the presence of the Higgs boson affects these top quark helicities in the $t\bar{t}H$ channel. In fact, the $t\bar{t}$ spin correlation in $t\bar{t}H$ is actually complementary with regard to the configuration in $t\bar{t}$ alone [83]. This is due to the Yukawa interaction between the top quark and the Higgs boson causing a chiral flip to the top quark spin and the $t\bar{t}$ pair will finally be observed in a $LL+RR$ helicity configuration [83]. Predicting the helicity configuration for the $t\bar{t} + b\bar{b}$ background turns out to be harder, even in the naive chiral limit. The reason is, that many different processes (initial state radiation from gluon, final state radiation from

5. Analysis of Angular Distributions in the $t\bar{t}(H \rightarrow b\bar{b})$ Channel

top quark or bottom quark etc.) will interfere and generally they all represent different final state top helicity configurations [83]. Further, the chiral limit is, at least for current LHC energies, very unrealistic. In reality, the top quark spin correlations are changing over phase space and it is not trivial to predict them. Nevertheless, one expects that the Yukawa coupling to the top quark has some impact on the top quark spins, so that the corresponding angular distributions will help to separate the signal from the background. Several observables were shown to be sensitive to top quark spin correlations [122]. One might use the opening angle θ between any top quark decay product and an anti-top quark decay product. Double polar distributions $\left(\frac{d^2\sigma}{d\cos(\theta_a)d\cos(\theta_b)}\right)$ are also sensitive. Thereby the observable θ_a ($\bar{\theta}_b$) describes the angle between the direction of flight of a top (anti-top) quark (or one of the respective decay products) and some direction \hat{a} (\hat{b}) that has to be defined. Further, one dimensional variables $\left(\frac{d\sigma}{d(\phi\pm\bar{\phi})}\right)$ that combine azimuthal angles ϕ ($\bar{\phi}$) of top (anti-top) quark decay products are also quite useful. All of the three mentioned types of observables were studied in this analysis. However, in order to increase their sensitivity one can also reconstruct the event and then boost the spin analysers into corresponding frames of reference, which increase the spatial correlation with the original top (anti-top) spin axis. Especially the t/\bar{t} rest frames, with respect to the laboratory frame (here referred to as Frame 2) or with respect to the $t\bar{t}$ zero-momentum-frame (referred to as Frame 1) [42] were already shown to be sensitive [83] (Frame 1 is actually equal to the helicity basis, discussed previously) and were also further studied in this analysis.

Boosting into those frames requires precise event reconstruction, however such is very challenging because of the large jet multiplicities that impede a correct jet-parton assignment in the single lepton channel and the presence of two neutrinos in the dilepton channel. Inter alia, one goal of this analysis was to find powerful laboratory-frame observables, which do not require further boosting. As shown in the following sections these can be set up, if one does not restrict the angular distributions to top quark decay products but also makes use of the decay products of the Higgs boson. The reason, why these decay products help to separate between signal and background is more obvious than in case of the top quark decay products. Since the Higgs boson is a scalar particle, it will show a very different emission pattern compared to the spin-1 gluon, which produces the $b\bar{b}$ -pair in the dominating background process. If one considers the angle Ω between the Higgs boson decay axis within the Higgs particle rest frame and the axis of the initial state gluons (beam axis) one expects a flat distribution for a scalar particle. The emission is isotropic and all angles equally probable. However, in the case of a decaying massless vector boson one expects a non-flat distribution, but one which follows a relation like $\frac{dN}{d\Omega} \sim 1 + \cos^2(\Omega)$. Due to the very different shape of these distributions one expects a

high separation between signal and background. Furthermore, it is possible to combine products from the top quark and the Higgs boson decay to obtain highly separative observables, see Section 5.1.1. One might reconstruct the top quark and the Higgs boson and study angular distributions between those two particles. It is clear that the emission of a Higgs boson will have an impact on the top quark four-momentum. One would expect that this effect varies for the corresponding background processes and therefore potentially be helpful for signal/background separation.

5.1. Single Lepton Channel

Different sets of angular observables were studied in the single lepton channel, including $\cos(\theta_{ij})$, ΔR_{ij} , $\Delta\eta_{ij}$ and $\Delta\phi_{ij}$, where $\{i, j\}$ denote certain top (or anti-top) quark or Higgs boson candidate decay products. From all possible $\{i, j\}$ combinations, 25 combinations that were found to be particularly sensitive, were chosen for a closer inspection. These combinations are presented in Table 5.1.

Top related	Remaining l related	Remaining W_{lep} related	Remaining $b_{t_{\text{lep}}}$ related	Remaining Higgs related
$\{i, j\}$	$\{i, j\}$	$\{i, j\}$	$\{i, j\}$	$\{i, j\}$
$t_{\text{lep}}, t_{\text{had}}$	l, W_{lep}	$W_{\text{lep}}, W_{\text{had}}$	$b_{t_{\text{lep}}}, b_H^1$	b_H^1, b_H^2
t_{lep}, l	l, W_{had}	$W_{\text{lep}}, b_{t_{\text{lep}}}$	$b_{t_{\text{lep}}}, b_H^2$	b_H^1, H
$t_{\text{lep}}, W_{\text{lep}}$	$l, b_{t_{\text{lep}}}$	W_{lep}, b_H^1	$b_{t_{\text{lep}}}, H$	
$t_{\text{lep}}, W_{\text{had}}$	l, b_H^1	W_{lep}, b_H^2		
$t_{\text{lep}}, b_{t_{\text{lep}}}$	l, b_H^2	W_{lep}, H		
$t_{\text{lep}}, b_{t_{\text{had}}}$	l, H			
t_{lep}, b_H^1				
t_{lep}, b_H^2				
t_{lep}, H				

Table 5.1.: Combinations of top quark, anti-top quark, Higgs boson and/or corresponding decay products. The studied angular observables are then set up between the particles i and j . Notation: t_{lep} (t_{had}) is the leptonically (hadronically) decaying top or anti-top quark, decay products from the respective top or anti-top quark are labelled with “lep” or “had”, l is the charged lepton, b means b -jet, H is the Higgs candidate, b_H^1 and b_H^2 are the p_T ordered b -jets from the Higgs candidate.

Thereby, the angular distributions with the highest separation between signal and back-

5. Analysis of Angular Distributions in the $t\bar{t}(H \rightarrow b\bar{b})$ Channel

ground are generally those that combine $t\bar{t}$ and Higgs boson decay products, for example $\cos(\theta_{tH})$. One might ask if one could only take the angle between the Higgs particle and the top or anti-top quark that actually emitted that Higgs boson. Ignoring the fact that the Higgs particle also can be emitted from an intermediate top quark and that the Higgs emissions from the different top quarks are quantum mechanically indistinguishable, one can take an experimental approach and take the angle between the Higgs boson and the closest top or anti-top quark. Thereby, closest means the shortest distance in η, ϕ space (minimal ΔR). For this purpose, a second set of particle combinations $\{i, j; k, l\}$ is set up (in the following referred to as *nearest* set). If ΔR between the particle i and the Higgs candidate is smaller than ΔR between the particle k and the Higgs candidate, the respective angular observable is evaluated between the pair $\{i, j\}$ and otherwise it is evaluated between the particles k and l . The particle combinations for the *nearest* set are given in Table 5.2.

Top related	Remaining W_{lep} related	Remaining $b_{t_{\text{lep}}}$ related	Remaining Higgs related
$\{i, j; k, l\}$	$\{i, j; k, l\}$	$\{i, j; k, l\}$	$\{i, j; k, l\}$
$t_{\text{lep}}, l; t_{\text{had}}, l$	$W_{\text{lep}}, l; W_{\text{had}}, l$	$b_{t_{\text{lep}}}, l; b_{t_{\text{had}}}, l$	$b_H^1, H; b_H^2, H$
$t_{\text{lep}}, W_{\text{lep}}; t_{\text{had}}, W_{\text{had}}$	$W_{\text{lep}}, b_{t_{\text{lep}}}; W_{\text{had}}, b_{t_{\text{had}}}$	$b_{t_{\text{lep}}}, b_H^1; b_{t_{\text{had}}}, b_H^1$	
$t_{\text{lep}}, W_{\text{had}}, t_{\text{had}}, W_{\text{lep}}$	$W_{\text{lep}}, b_H^1; W_{\text{had}}, b_H^1$	$b_{t_{\text{lep}}}, b_H^2; b_{t_{\text{had}}}, b_H^2$	
$t_{\text{lep}}, b_{t_{\text{lep}}}; t_{\text{had}}, b_{t_{\text{had}}}$	$W_{\text{lep}}, b_H^2; W_{\text{had}}, b_H^2$	$b_{t_{\text{lep}}}, H; b_{t_{\text{had}}}, H$	
$t_{\text{lep}}, b_{t_{\text{had}}}; t_{\text{had}}, b_{t_{\text{lep}}}$	$W_{\text{lep}}, H; W_{\text{had}}, H$		
$t_{\text{lep}}, b_H^1; t_{\text{had}}, b_H^1$			
$t_{\text{lep}}, b_H^2; t_{\text{had}}, b_H^2$			
$t_{\text{lep}}, H; t_{\text{had}}, H$			

Table 5.2.: Combinations of top quark, anti-top quark, Higgs boson and/or corresponding decay products. The same notation as in Table 5.1 is used. The studied angular observables are then set up either between the particles i and j or the particles k and l depending on whether i or k is closer to the Higgs boson candidate in terms of ΔR .

A further set of angular observables was studied. These variables are more complex and require individual definition. The angle $\Omega_{t_{\text{lep}}}^{t\bar{t}}$ is the angle between the direction of the leptonically decaying top quark within the $t\bar{t}$ COM and the direction of the beam axis. The observable $\Omega_{t_{\text{lep}}}^{t_{\text{lep}}H}$ describes the same angle, but with the leptonic top quark boosted into the $t_{\text{lep}}H$ system. The observable $\Omega_{b_H^1}$ is the polar angle between the beam line and the leading (p_T) b -jet from the Higgs boson decay within the laboratory frame. The

observables φ_{CP}^* and $\varphi_{CP}^{\text{Lab}}$ were studied. Thereby, φ_{CP}^* is actually designed in a way similar to [123] to be applied to the Higgs boson decay products in order to determine the Higgs CP quantum number. However, it also turned out to be sensitive when it comes to the separation between the $t\bar{t}(H \rightarrow b\bar{b})$ signal and the $t\bar{t} + b\bar{b}$ background. The observable is defined through the relations

$$\varphi^* = \arccos(\hat{l}_+^\perp \cdot \hat{l}_-^\perp), \quad (5.1)$$

and

$$\varphi_{CP}^* = \begin{cases} \varphi^*, & \text{if } (\hat{l}_+ \times \hat{l}_-) \cdot \hat{k} \geq 0, \\ 2\pi - \varphi^*, & \text{if } (\hat{l}_+ \times \hat{l}_-) \cdot \hat{k} < 0. \end{cases} \quad (5.2)$$

Here, \hat{l}_+^\perp (\hat{l}_-^\perp) are the normalised directions of flight of the Higgs boson decay products, perpendicular to a direction \hat{k} , which is in this case the direction of the leptonically decaying top quark defined in Frame 1. Then, $\varphi_{CP}^{\text{Lab}}$ was set up in a similar fashion, however using only laboratory frame quantities, namely using the lepton momentum instead of the respective top quark in order to define the direction \hat{k} .

Further CP sensitive observables were set up in a similar fashion to [124–126]. Thereby, angles θ_Y^X are defined between the direction of a particle (or particle system) Y within the rest frame of particle (system) X and the direction of X in the rest frame of its own mother particle or particle system. All decays then start from the $t\bar{t}H$ system ($X = t\bar{t}H$) and its direction of momentum is measured within the laboratory frame [125]. The studied angular distributions are:

$$\begin{aligned} & \cos(\theta_H^{t_{\text{lep}}H}) \cos(\theta_l^H) \text{ (db)}, \\ & \sin(\theta_H^{t\bar{t}H}) \sin(\theta_{b_{t_{\text{lep}}}}^{t_{\text{lep}}}) \text{ (sb)}, \\ & \sin(\theta_H^{t\bar{t}H}) \cos(\theta_{b_H}^{\text{lep}}) \text{ (sb)}, \\ & \sin(\theta_{t_{\text{had}}}^{t\bar{t}H}) \sin(\theta_{W_{\text{had}}}^H) \text{ (sb)}, \\ & \sin(\theta_{t_{\text{lep}}}^{t\bar{t}H}) \sin(\theta_{b_H}^H) \text{ (sb)}, \\ & \sin(\theta_H^{t\bar{t}H}) \sin(\theta_{t_{\text{had}}}^{t\bar{t}}) \text{ (db)}. \end{aligned}$$

So the first distribution is calculated by multiplying the cosines of the angle $\theta_H^{t_{\text{lep}}H}$ between the direction of the Higgs candidate measured in the $t_{\text{lep}}H$ frame of reference and the direction of the $t_{\text{lep}}H$ system evaluated within the $t\bar{t}H$ system, and the angle θ_l^H between

5. Analysis of Angular Distributions in the $t\bar{t}(H \rightarrow b\bar{b})$ Channel

the momentum direction of the lepton measured within the Higgs candidate rest frame and the direction of the Higgs candidate boosted into the $t_{\text{lep}}H$ frame of reference. The other distributions are calculated analogously. Thereby, “db” means a *direct* Lorentz boost into the respective system and “sb” means a chain of *sequential* boosts through all intermediate systems until the four-momenta are evaluated in the $t\bar{t}H$ system. The last studied observable, b_4 , was introduced in [127] and it is defined by the following relation:

$$b_4 = \frac{p_{t_{\text{lep}}}^z \cdot p_{t_{\text{had}}}^z}{|\vec{p}_{t_{\text{lep}}}| \cdot |\vec{p}_{t_{\text{had}}}|}, \quad (5.3)$$

where p^z is z -component of the corresponding top or anti-top quark momentum \vec{p} .

5.1.1. Generator Level and Reconstruction Level Studies

On MC generator level, the only irreducible background arises from the $t\bar{t} + b\bar{b}$ events. The introduced angular observables were studied on particle level, whereby the generator level jets were matched to the corresponding partons via a minimum ΔR match. Thereby, generator level events are selected if the corresponding physics objects on reconstruction level satisfy the introduced selection criteria, however with no restriction on the number of reconstructed jets, as only true $t\bar{t}(H \rightarrow b\bar{b})$ (and respectively $t\bar{t} + b\bar{b}$) events are selected.

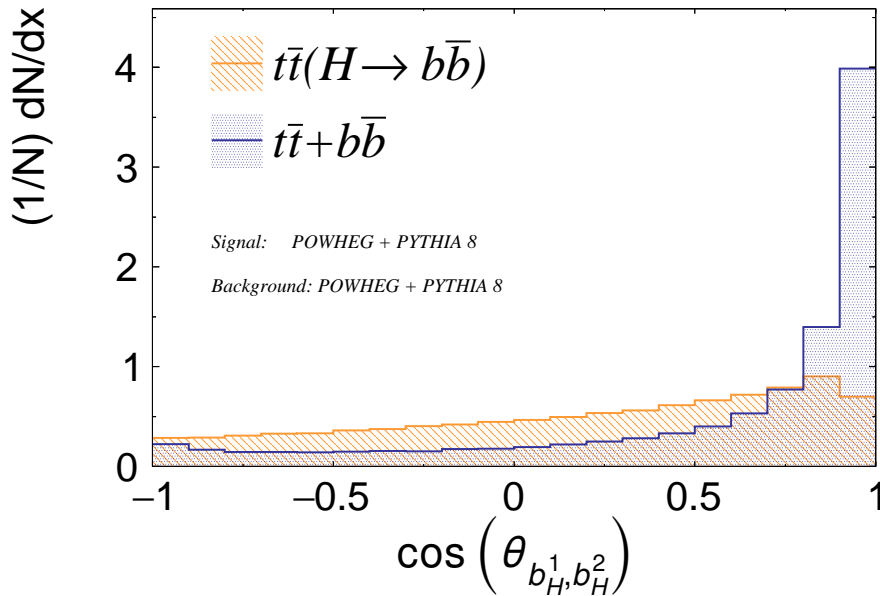


Figure 5.1.: The $\cos(\theta_{b_H^1, b_H^2})$ distribution for the $t\bar{t}(H \rightarrow b\bar{b})$ signal (orange) and for the $t\bar{t} + b\bar{b}$ background (blue) on the MC generator particle level. Signal and background modelled with POWHEG + PYTHIA 8.

It was found that the $\cos(\theta_{b_H^1, b_H^2})$ distribution, presented in Figure 5.1, is the most sensitive one when it comes to a separation between signal and background. The separation power of the studied observables is quantified by the separation value \mathcal{S} . In the case of $\cos(\theta_{b_H^1, b_H^2})$, the separation value \mathcal{S}^1 is 19.7%², whereby \mathcal{S} is defined via the relation:

$$\mathcal{S} = \frac{1}{2} \sum_i^N \frac{(y_i^{\text{sig}} - y_i^{\text{bkg}})^2}{(y_i^{\text{sig}} + y_i^{\text{bkg}})} \cdot \Delta x. \quad (5.4)$$

Thereby N is the number of bins in the corresponding histogram, y_i^{sig} and y_i^{bkg} are the (normalised) numbers of signal and background events within a given bin i , respectively. The bin width is described by Δx , assuming non-variable bin widths.

It is clear, however, that the opening angle between the two b -jets from the Higgs candidate is strongly anti-correlated with the mass m_H of the Higgs candidate in the case of the background, because jets originating from gluon radiation follow the collinear divergence of QCD. Low energetic jets then tend to have a small opening angle, hence the distribution will peak at $\cos(\theta) = 1$. On the other hand, the signal distribution is rather flat due to the scalar nature of the Higgs boson. The slight slope of the distribution is explained by the boost that the b -jets experience from the non-zero momentum of the Higgs boson in the laboratory frame. The drop of the event rate near $\cos(\theta) = 1$ is related to the event selection cuts. These cuts are also present in the $t\bar{t} + b\bar{b}$ truth distribution, however, since the event rate is very high in the last bin, the impact of the cuts is not directly visible at that point.

The second highest separation value is given by the distribution φ_{CP}^* with, $\mathcal{S} = 17.7\%$. The observable is visualised in Figure 5.2. Despite its high separation power on particle level and low correlations with respect to other variables such as angular separations or the invariant mass m_H , this variable does not turn out to be very useful in the single lepton channel on reconstruction level. The main reason for this is that φ_{CP}^* is found to be particularly sensitive to the $t\bar{t} + b\bar{b}$ background. However, as discussed later on in more detail, on the reconstruction level only some regions are dominated by this type of background and other regions show large background contributions from other types of $t\bar{t}$ +jets. As a consequence, one obtains $\mathcal{S} = 0.09\%$, $\mathcal{S} = 0.4\%$ and $\mathcal{S} = 0.8\%$ if one constructs φ_{CP}^* in the single lepton channel control regions, signal regions or exclusively

¹As apparent from the definition in Equation 5.4, the separation value depends on the chosen binning for the signal and background histograms. Throughout this analysis, quoted separation values pertain to a number of 40 bins, regardless of how many bins are plotted in a corresponding figure.

²The statistical uncertainties on the separation values are generally very low in the order of $10^{-3}\%$. In the following, they will not be specified unless stated otherwise. Generally, statistical uncertainties are not a limiting factor for $t\bar{t}(H \rightarrow b\bar{b})$ searches.

5. Analysis of Angular Distributions in the $t\bar{t}(H \rightarrow b\bar{b})$ Channel

in the $t\bar{t} + b\bar{b}$ dominated signal regions, respectively. However, none of these separation values can be considered good and as later shown, the variable is more useful in the dilepton channel.

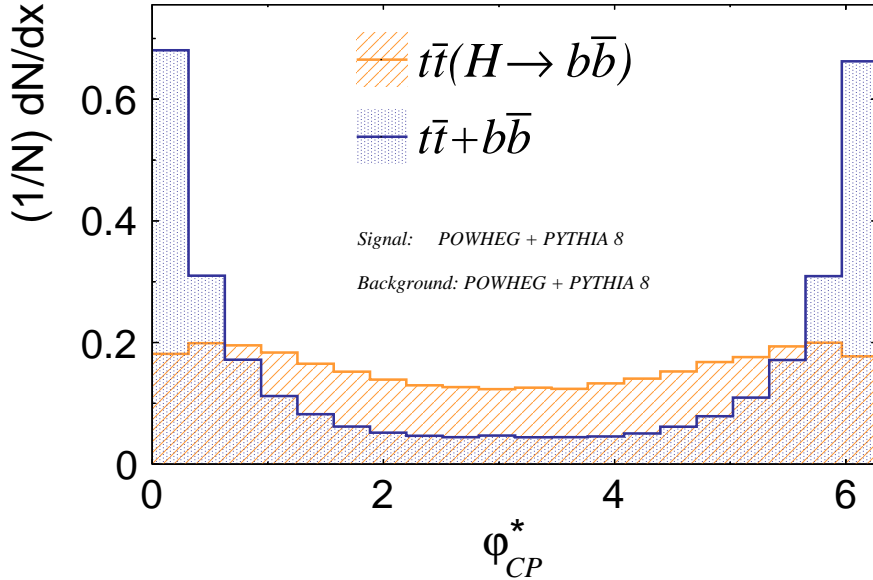


Figure 5.2.: The φ_{CP}^* distribution for the $t\bar{t}(H \rightarrow b\bar{b})$ signal (orange) and for the $t\bar{t} + b\bar{b}$ background (blue) on the MC generator particle level. Signal and background modelled with POWHEG + PYTHIA 8.

From the ten observables with the highest ranked separation powers on particle level, the remaining ones are dominated by $\Delta\eta$ variables, whereby $\Delta\eta_{t_{lep}, H}$, shown in Figure 5.3 (a), is found to be the most sensitive one with $\mathcal{S} = 17.6\%$. The particle pair $\{t_{lep}, H\}$ also gives the best performing ΔR observable ($\mathcal{S} = 13.2\%$), presented in Figure 5.4 (a), which is of course correlated with the respective $\Delta\eta$ distribution. As apparent, the well performing angular observables are constructed from combinations of top or anti-top quark and the Higgs boson candidate or from their respective decay products. From the studied particle level observables, the most sensitive ones related entirely to the top or anti-top quark (or their decay products) turned out to be $\Delta R_{t\bar{t}}$ (with $\mathcal{S} = 1.3\%$) and $\Delta\eta_{t\bar{t}}$ (with $\mathcal{S} = 0.7\%$).

Reconstruction Level

On MC reconstruction level, the separation power of the angular observables changes significantly with respect to the generator particle level. Thereby, the biggest differences do not arise from detector resolution effects but rather from the combinatorial backgrounds

due to wrong jet-parton assignments and from the contributions of $t\bar{t} + c$ /light jets to the (irreducible) $t\bar{t}$ +jets background that is no longer purely of $t\bar{t} + b\bar{b}$ nature.

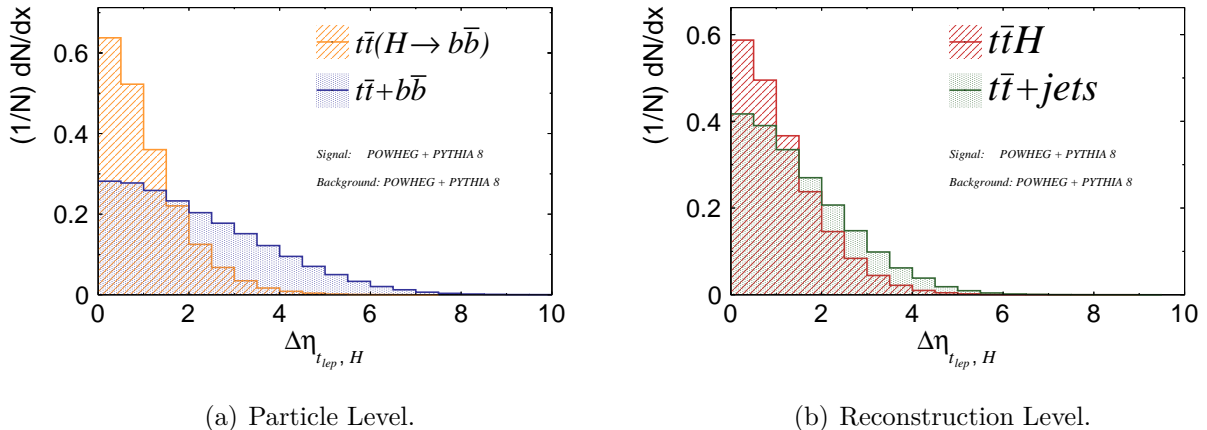


Figure 5.3.: The $\Delta\eta_{lep,H}$ distribution for the $t\bar{t}(H \rightarrow b\bar{b})$ signal (orange) and for the $t\bar{t} + b\bar{b}$ background (blue) on the MC generator particle level (a) and for the $t\bar{t}H$ signal (red) and the $t\bar{t}$ +jets background (green) on reconstruction level (b). Signal and background modelled with POWHEG + PYTHIA 8.

The former effect has of course a large impact on most distributions because one effectively constructs a completely different angle if the jet-parton assignment is wrong. In this way, the most separative angular distributions from the particle level such as $\Delta\eta_{lep,H}$, $\Delta R_{lep,H}$

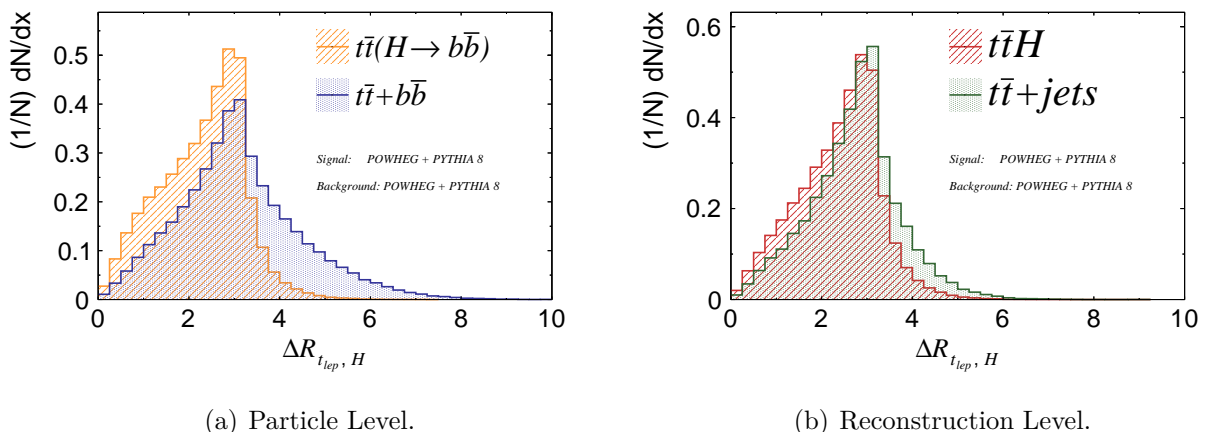


Figure 5.4.: The $\Delta R_{lep,H}$ distribution for the $t\bar{t}(H \rightarrow b\bar{b})$ signal (orange) and for the $t\bar{t} + b\bar{b}$ background (blue) on the MC generator particle level (a) and for the $t\bar{t}H$ signal (red) and the $t\bar{t}$ +jets background (green) on reconstruction level (b). Signal and background modelled with POWHEG + PYTHIA 8.

5. Analysis of Angular Distributions in the $t\bar{t}(H \rightarrow b\bar{b})$ Channel

(presented in Figure 5.3 (b) and 5.4 (b) on the reconstruction level) and foremost $\cos(\theta_{b_H^1, b_H^2})$, lose most of their separation power on the reconstruction level ($\mathcal{S} = 3.4\%$, $\mathcal{S} = 3.6\%$ and $\mathcal{S} = 1.3\%$, respectively, when calculated on all signal regions inclusively). In the latter case, the separation gets even worse ($\mathcal{S} = 0.9\%$) if one uses the four-momenta obtained from the reconstruction BDT with additional Higgs boson information, since the strongly correlated input variable m_H is used as an input there and the corresponding distribution gets biased towards the signal expectation by this BDT. Besides, on reconstruction level, the Higgs candidate mass distribution loses most of its separation power as well, as a consequence of the wrong jet assignments, resolution effects and selection criteria. This is shown in Figure 5.5: while the Higgs candidate mass is one of the most sensitive variables one can construct in the $t\bar{t}(H \rightarrow b\bar{b})$ channel on particle level ($\mathcal{S} = 48\%$), its separation power decreases by a factor of ten to approximately 4% (reconstructed by the BDT without Higgs information and calculated from all signal regions inclusively).

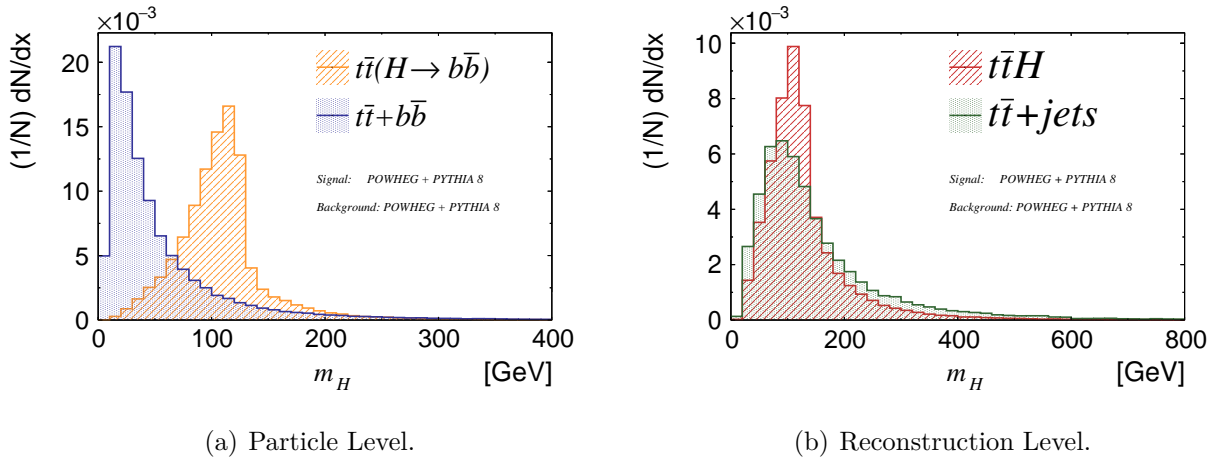


Figure 5.5.: The Higgs candidate mass (m_H) distribution for the $t\bar{t}(H \rightarrow b\bar{b})$ signal (orange) and for the $t\bar{t} + b\bar{b}$ background (blue) on the MC generator particle level (a) and for the $t\bar{t}H$ signal (red) and the $t\bar{t}+jets$ background (green) on reconstruction level (b). Signal and background modelled with POWHEG + PYTHIA 8.

Interestingly, there are also angular observables with a higher separation power on reconstruction level than on particle level, for example the variables $\Delta R_{t\bar{t}}$ or $\Delta\eta_{t\bar{t}}$ (respectively $\mathcal{S} = 1.8\%$ and $\mathcal{S} = 2.2\%$, when calculated from all signal regions inclusively). This might seem counterintuitive, however, the reason for this behaviour becomes clear if one keeps in mind the combinatorial mistakes in the reconstruction process. If a wrong bottom quark (a b -jet from the Higgs boson decay) gets assigned to the top quark or anti-top quark, one effectively obtains angles between top and (or sometimes only) Higgs decay products,

which have in general higher separation powers because of the fundamental difference in the spin quantum number of the Higgs boson and gluon, as discussed previously. This explanation gets confirmed if one looks at the same angle, but reconstructed via the BDT with additional Higgs boson information. Here, the chance that the Higgs particle gets reconstructed properly is higher. Consequently, the separation power will be lower than for the reconstruction with the BDT without additional information on the Higgs boson (in the case of $\Delta\eta_{t\bar{t}}$, $\mathcal{S} = 2\%$ for the BDT with Higgs information). However, other distributions benefit from the reconstruction with additional Higgs boson information. In fact, the angular observable $\Delta\eta_{b_{t_{\text{lep}}}, b_H^1}$ between the b -jet from the leptonically decaying top or anti top quark and the highest p_T b -jet from the Higgs boson candidate, was found to be the most sensitive variable on reconstruction level, if it is constructed with four-momenta obtained from the reconstruction BDT using additional Higgs boson information.

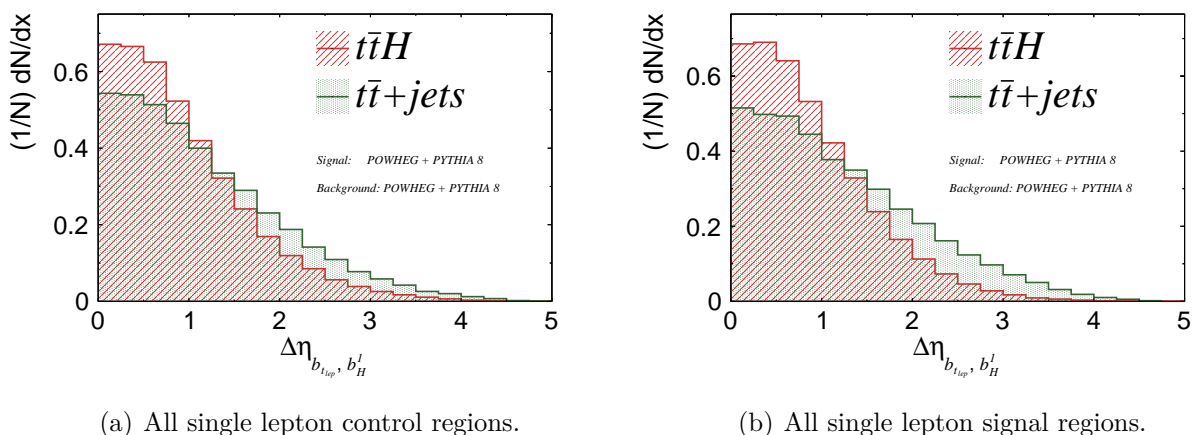


Figure 5.6.: The $\Delta\eta_{b_{t_{\text{lep}}}, b_H^1}$ distribution for the $t\bar{t}H$ signal (red) and the $t\bar{t}+\text{jets}$ background (green) on reconstruction level inclusively in all single lepton control regions (a) and in all signal regions (b). Signal and background modelled with POWHEG + PYTHIA 8.

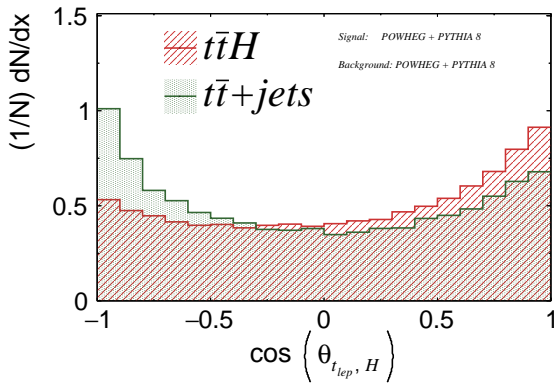
As mentioned before, another effect with large impact on the angular distributions is in fact the contribution of $t\bar{t}+\text{jets}$ backgrounds that are of non $t\bar{t} + b\bar{b}$ nature. Thereby, angular distributions of the $t\bar{t} + c/\text{light jets}$ background are found to be more signal-like than the $t\bar{t} + b\bar{b}$ distributions and therefore the studied angular observables show less separation power in regions dominated by $t\bar{t} + c/\text{light jets}$. This effect is demonstrated in Figure 5.6, that shows the distribution of the most sensitive angular separation $\Delta\eta_{b_{t_{\text{lep}}}, b_H^1}$, inclusively in all single lepton control regions (a) and inclusively in all single lepton signal regions (b). While the separation is $\mathcal{S} = 2.3\%$ in the former case, the value roughly

5. Analysis of Angular Distributions in the $t\bar{t}(H \rightarrow b\bar{b})$ Channel

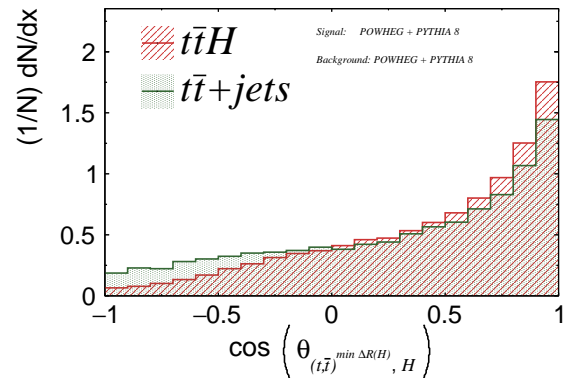
doubles to $\mathcal{S} = 4.4\%$ in the latter case. As is visible in Figure 5.6 (a), the peak and the tail of the background distribution is clearly shifted toward the signal distribution with respect to the distribution shown in Figure 5.6 (b). Note that also the signal compositions in the control regions differ from those in the signal regions, however they are still largely dominated by $t\bar{t}(H \rightarrow b\bar{b})$ and therefore the signal shape does not change significantly.

Consequently, one would expect an additional increase of separation power, if the two single lepton signal regions dominated by $t\bar{t} + c/\text{light jets}$ SR_2^{5j} and $\text{SR}_3^{\geq 6j}$ are excluded. Indeed, a further increase in separation power of the angular observables is then observed. In the case of $\Delta\eta_{b_{\text{lep}}, b_H^1}$ for example, the separation value increases to $\mathcal{S} = 4.8\%$.

The possible advantage of the *nearest* set of angular observables is visualised in Figure 5.7 (a) and (b). In (a), the cosine of the opening angle between the leptonically decaying top quark and the Higgs boson candidate, $(\theta_{t_{\text{lep}}, H})$, is presented on reconstruction level. On the right plot (b), one can see the corresponding distribution of the *nearest* set, $\cos(\theta_{(t\bar{t})^{\min \Delta R(H), H})})$, which is the cosine of the angle between the Higgs candidate and the closest top or anti-top quark in terms of ΔR . The separation values are $\mathcal{S} = 1.9\%$ and $\mathcal{S} = 2.2\%$, respectively, (calculated from SR_1^{5j} , $\text{SR}_1^{\geq 6j}$ and $\text{SR}_2^{\geq 6j}$). Even though the gain is rather small in this case, larger impacts are observed in the corresponding ΔR distributions (from $\mathcal{S} = 3.67\%$ with $\Delta R_{t_{\text{lep}}, H}$ to $\mathcal{S} = 4.11\%$ with $\Delta R_{(t\bar{t})^{\min \Delta R(H), H}}$), which are even more powerful in the dilepton channel as shown later on.



(a) Higgs candidate and top quark.



(b) Higgs candidate and closest top quark.

Figure 5.7.: The $\cos(\theta_{t, H})$ distribution (a) and the $\cos(\theta_{(t\bar{t})^{\min \Delta R(H), H}})$ distribution (b) for the $t\bar{t}H$ signal (red) and the $t\bar{t}+\text{jets}$ background (green) on reconstruction level, considering the signal regions SR_1^{5j} , $\text{SR}_1^{\geq 6j}$ and $\text{SR}_2^{\geq 6j}$. Signal and background modelled with POWHEG + PYTHIA 8.

As indicated earlier, the separation power of certain observables should be enhanced by boosting the corresponding decay products into other frames such as Frame 1 or Frame

2. This was studied and it was found that the separation of variables exclusively related to the $t\bar{t}$ system increases, see Section 5.2.1. However, the gain is rather modest and the observables with high sensitivity, such as certain $\Delta\eta$ and ΔR distributions combining top quark and Higgs boson decay products, were observed to rather lose their separation power when boosting them outside of the laboratory frame.

5.1.2. Boosted Events

Due to the different event topologies that arise in the case of events that contain at least one top quark, anti-top quark or Higgs boson (candidate) with high transverse momentum, the separation power of certain (angular) observables is expected to be higher in the corresponding phase space regions [83]. In order to study this effect, four *boosted regions* (referred to as BR) are defined. Thereby, events with at least one top or anti-top quark with $p_T > 250$ GeV enter region BR₁. The remaining events with a Higgs boson candidate with $p_T > 250$ GeV enter BR₂. The remaining events with at least one top or anti-top quark with $p_T > 200$ GeV then enter BR₃ and the leftover events are classified as BR₄. The impacts of these selection cuts, imposed by the regions BR₁ and BR₂, on the studied angular distributions are not trivial. While some distributions gain in separation power, other variables see a decrease. However, also the correlations of the variables change and the performance of multivariate algorithms can benefit from these cuts, as shown in the following section.

5.1.3. Multivariate Techniques on Reconstruction Level

On reconstruction level, many of the studied angular observables show quite some separation power on the order of up to 5%. However, it is clear that a lot of these observables are correlated with each other. Combining several of them to some probability density function that helps enhancing the S/B ratio is therefore difficult. Instead, as the separation power of the most sensitive studied angular observables is comparable to the majority of the variables already used in the ATLAS $t\bar{t}(H \rightarrow b\bar{b})$ classification BDT, they can be used to enhance the BDT performance.

For this purpose different BDTs are trained on and applied to MC simulations on reconstruction level, using TMVA. One of the BDTs represents the ATLAS $t\bar{t}(H \rightarrow b\bar{b})$ classification BDT (in the following referred to as classification BDT) with all the input variables as defined in Appendix A.2, with exception of MEM_{D1} as it is only defined in one region, but the BDTs are trained and tested inclusively on several regions. The other BDT (in the following referred to as angular BDT) takes all the studied angular

5. Analysis of Angular Distributions in the $t\bar{t}(H \rightarrow b\bar{b})$ Channel

observables as input variables, however with exception of the $\Delta\phi$ variables as they were in general found to give poor performance.

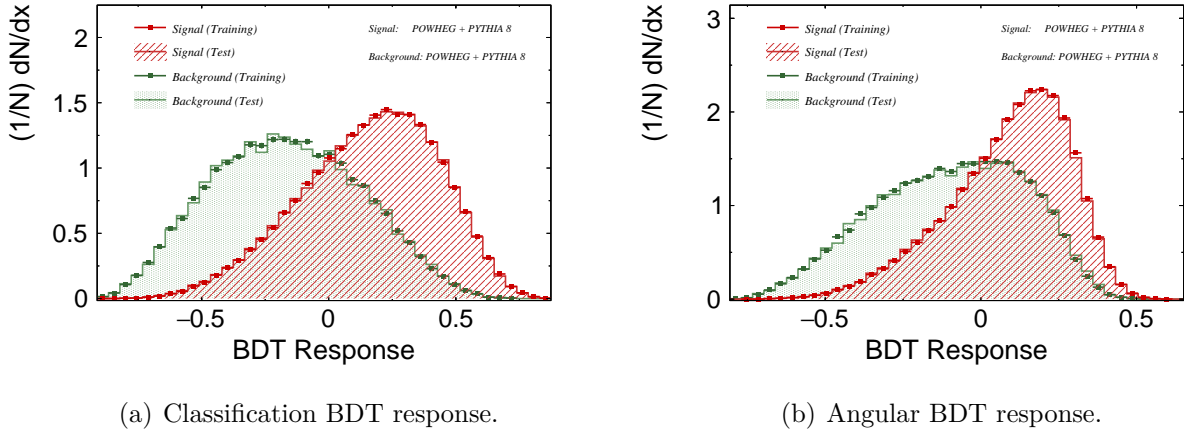


Figure 5.8.: BDT response distributions for the single lepton channel on MC reconstruction level. All single lepton signal regions are considered. Signal ($t\bar{t}H$) and background ($t\bar{t}$ +jets) were modelled with POWHEG + PYTHIA 8.

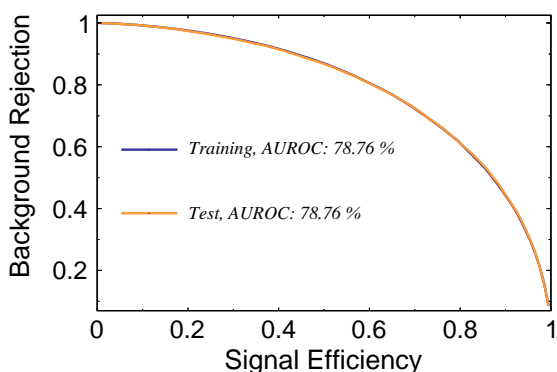
The following TMVA settings were used: the minimum node size is set to 4%, the boosting type is set to “AdaBoost” and the corresponding parameter β is set to 0.15, for the separation type “GiniIndex” is chosen and the number of cuts is set to 80. These settings represent the settings of the ATLAS $t\bar{t}(H \rightarrow b\bar{b})$ classification BDT, with exception of the number of trees in the forest, which is set to 400 instead of 250 because a slight increase in performance was observed when using more trees. The input distributions are scaled in such a way, that the number of signal and background events are equal.

Figure 5.8 (a) presents the output of the classification BDT trained on and applied to all single lepton signal regions. Thereby, the other plot, (b), shows the respective distribution of the angular BDT. The separation values of the output distributions are $\mathcal{S} = (24.8 \pm 0.2)\%$ and $\mathcal{S} = (16.6 \pm 0.1)\%$ respectively. Thereby, the most sensitive input variables (in terms of separation power) to the classification BDT are the LHD ($\mathcal{S} = 11.4\%$), $\Delta R_{bb}^{\text{avg}}$ ($\mathcal{S} = 7.7\%$) and $\Delta\eta_{jj}^{\text{max}\Delta\eta}$ ($\mathcal{S} = 4.8\%$). However, these are not the three most important variables, as not only the separation power, but also the correlations and the amount of input variables determine the performance of a BDT. In this sense, the LHD, $\Delta R_{bb}^{\text{avg}}$ and the reconstruction BDT (with Higgs boson information) output ($\mathcal{S} = 3.5\%$) are the three most important input variables.

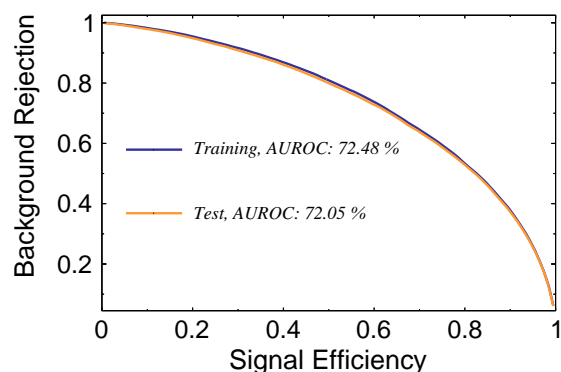
Aside from the separation \mathcal{S} , another quantity is used to specify the BDT performance. Thereby, it is about the area under the *Receiver Operating Characteristic* (ROC) curve.

Here, the ROC curve is obtained from the signal efficiency as a function of background rejection. The respective area under the ROC curve is in the following referred to as AUROC.

The ROC curves related to the classification and angular BDT performance are presented in Figure 5.9 (a) and (b) respectively. The corresponding AUROC values are 78.76% in case of the classification BDT and 72.05% in case of the angular BDT. The mentioned numbers thereby refer to the distributions of the tested events, shown in orange in Figure 5.9. The ones obtained from the training events are shown in blue. In both plots, the blue and orange curves agree well and one can conclude that no significant overtraining is happening.



(a) Classification BDT ROC curve.



(b) Angular BDT ROC curve.

Figure 5.9.: ROC curves from the classification BDT and the angular BDT for the single lepton channel on MC reconstruction level. All single lepton signal regions are considered. Signal ($t\bar{t}H$) and background ($t\bar{t}$ +jets) were modelled with POWHEG + PYTHIA 8.

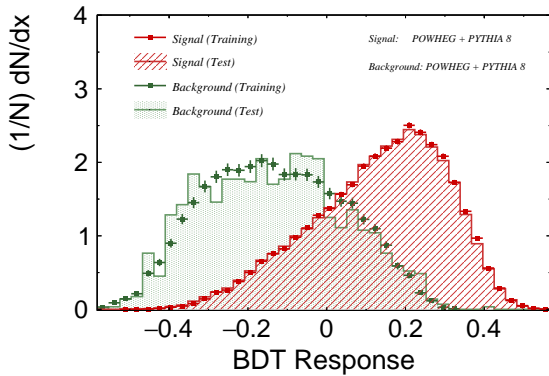
As apparent from the Figures 5.8 and 5.9, the angular BDT performs worse than the classification BDT. If all classification and angular BDT input variables are joined as inputs for a combined BDT, the performance increases with respect to the classification BDT alone. One obtains $\mathcal{S} = (26.0 \pm 0.5)\%$ and $\text{AUROC} = 79.45\%$. These values represent the maximum performance an optimised classification BDT could achieve using some of the angular observables as alternative input. In this case, the gain seems rather small. Nevertheless, signal and phase space regions were found in which the angular BDT appears to be more useful. First of all, the signal regions can be addressed. As the separation power of the individual angular observables increases once the $t\bar{t}$ +jets background is dominated by $t\bar{t} + b\bar{b}$, one would expect an enhanced performance of the BDT when the

5. Analysis of Angular Distributions in the $t\bar{t}(H \rightarrow b\bar{b})$ Channel

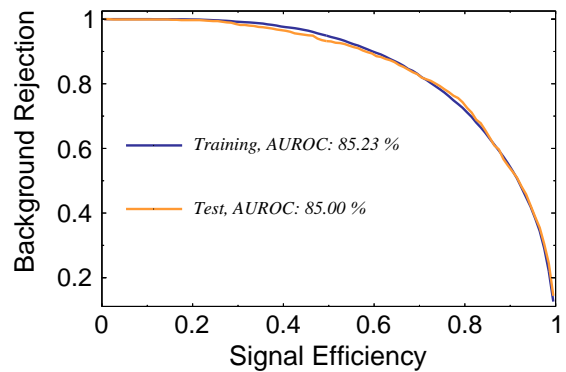
signal regions SR_2^{5j} and $SR_3^{\geq 6j}$ are excluded from consideration. Actually, this was found to be the case and the performance of the angular BDT increases from $\mathcal{S} = (16.6 \pm 0.1) \%$ to $\mathcal{S} = (20.0 \pm 0.3) \%$, while the performance of the classification BDT remains almost unchanged with $\mathcal{S} = (25.0 \pm 0.5) \%$. If all angular and classification BDT input variables are then joined as an input for a combined BDT, the respective BDT response distributions show a separation of $\mathcal{S} = (27.7 \pm 0.6) \%$ and the corresponding ROC curve gives an AUROC value of 80.36 %. By taking also SR_1^{5j} out of consideration (slightly less precise reconstruction with respect to regions with more than five jets), no further improvement is observed.

However, an improved performance is observed when training and testing the BDT on events in the boosted regions. The separation power of the angular BDT output increases from $\mathcal{S} = (16.6 \pm 0.1) \%$ to $\mathcal{S} = (17.3 \pm 0.2) \%$ when only the boosted regions BR_1 , BR_2 and BR_3 are considered (but all signal regions are considered). In this manner, the performance is further enhanced to $\mathcal{S} = (19.3 \pm 0.2) \%$ if only BR_1 and BR_2 are considered. The AUROC values change accordingly from 72.05 % over 73.91 % to 75.18 % respectively. The separation value of the classification BDT is $\mathcal{S} = (24.5 \pm 0.5) \%$ if only the first three boosted regions are considered and $\mathcal{S} = (25.9 \pm 0.5) \%$ if BR_3 is also excluded.

Consequently, the best performance is observed if one selects events that are simultaneously in SR_1^{5j} , $SR_1^{\geq 6j}$ or $SR_2^{\geq 6j}$ and BR_1 or BR_2 . In the case of the background, around 13 % of the signal region events are selected using these criteria and in case of the signal the acceptance is higher, around 20 %.



(a) Combined BDT response.



(b) Combined BDT ROC curve.

Figure 5.10.: BDT response distributions for the single lepton channel on MC reconstruction level. The signal regions SR_1^{5j} , $SR_1^{\geq 6j}$ and $SR_2^{\geq 6j}$ are considered. Additionally, BR_1 or BR_2 must contain the selected events. Signal ($t\bar{t}H$) and background ($t\bar{t}$ +jets) were modelled with POWHEG + PYTHIA 8.

Nevertheless, the performance of the angular BDT enhances from $\mathcal{S} = (20.0 \pm 0.3) \%$ (in $\text{SR}_1^{5j} + \text{SR}_1^{\geq 6j} + \text{SR}_2^{\geq 6j}$ and no additional boosted region criterion) over $\mathcal{S} = (23.4 \pm 0.5) \%$ (in $\text{SR}_1^{5j} + \text{SR}_1^{\geq 6j} + \text{SR}_2^{\geq 6j}$ within BR_1 , BR_2 or BR_3) to $\mathcal{S} = (29.1 \pm 0.9) \%$ (in $\text{SR}_1^{5j} + \text{SR}_1^{\geq 6j} + \text{SR}_2^{\geq 6j}$ within BR_1 or BR_2). The performance of the classification BDT increases from $\mathcal{S} = (25.0 \pm 0.5) \%$ (in $\text{SR}_1^{5j} + \text{SR}_1^{\geq 6j} + \text{SR}_2^{\geq 6j}$ and no additional boosted region criterion) over $\mathcal{S} = (27.9 \pm 0.6) \%$ (in $\text{SR}_1^{5j} + \text{SR}_1^{\geq 6j} + \text{SR}_2^{\geq 6j}$ within BR_1 , BR_2 or BR_3) to $\mathcal{S} = (31.2 \pm 1.1) \%$ (in $\text{SR}_1^{5j} + \text{SR}_1^{\geq 6j} + \text{SR}_2^{\geq 6j}$ within BR_1 or BR_2). If then all angular and classification BDT input variables are joined as an input for a combined BDT, the respective BDT response distributions, presented in Figure 5.10 (a) show a separation of $\mathcal{S} = (37.2 \pm 1.4) \%$ and the corresponding ROC curve, presented in 5.10 (b) gives an AUROC value of 85.00%. As apparent from Figure 5.10 (a) the number of events (especially in the background) is rather low, however this is not a problem since no overtraining is happening apart from statistical effects, as visible in Figure 5.10 (b).

5.1.4. Optimised Classification BDT

As shown in the previous section, the performance of the classification BDT can be enhanced by variables from the angular BDT. However, since the number of input variables is very high in the case of the angular BDT, an optimisation procedure is needed under which the number of input variables to the classification BDT remains invariant, but its separation power gets improved. The developed optimisation method is based on the input variable ranking provided by TMVA, which is derived from the number of appearances of certain variables within the BDT structure. In detail, it is counted how many times a respective input variable is used to split a decision tree node. Thereby, each split is then weighted, according to the number of events in the corresponding node and the squared gain in separation that is provided by the split. However, this measure of the variable importance is unstable, which means if a full set of input variables has a TMVA ranking with a certain order, the order is likely to change if the number of input variables is reduced. In order to optimise the classification BDT, the BDT is trained and tested and the worst performing variable according to the respective recent TMVA ranking is removed from the set of input variables. This procedure is repeated until no variables are left. To reduce the number of iterations, the worst ten (five) variables are removed after each training if the number of input variables is higher than hundred (thirty). When the original number of input variables to the classification BDT is reached, an alternative optimisation procedure is used. Thereby, the variable with the least impact on the performance in terms of the AUROC value is removed iteratively. This search procedure in very high dimensional parameter space can perform better than the method described above,

5. Analysis of Angular Distributions in the $t\bar{t}(H \rightarrow b\bar{b})$ Channel

however, it is more CPU intensive since the number of needed BDT training entities scales with the number of input variables n as $n(n+1)/2$.

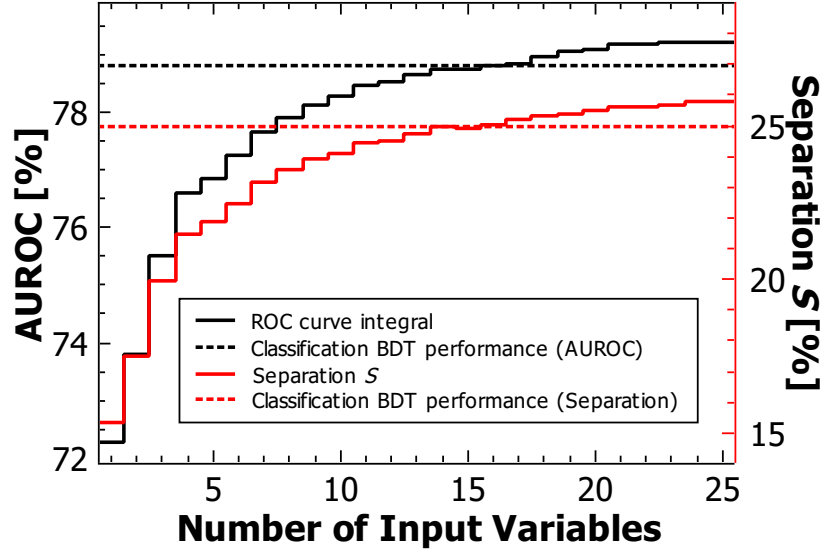


Figure 5.11.: Number of input variables to the (optimised) classification BDT in the single lepton channel, considering the signal regions SR_1^{5j} , $SR_1^{\geq 6j}$ and $SR_2^{\geq 6j}$ versus the performance, measured in AUROC values (black) and separation values (red).

While it would be possible to optimise the classification BDT considering all single lepton signal regions, no attempt was made because the gain is rather low and the advantage is open to question when keeping systematic uncertainties in mind. However, the classification BDT was optimised in the signal regions SR_1^{5j} , $SR_1^{\geq 6j}$ and $SR_2^{\geq 6j}$ with the help of the studied angular observables. Thereby, Figure 5.11 visualises the number of input variables to the optimised classification BDT versus its performance. As a benchmark, the respective AUROC and separation power of the original classification BDT are also plotted (dashed lines). One can see, that the optimised classification BDT with the original number of variables has $\mathcal{S} = (25.6 \pm 0.5)\%$ and $\text{AUROC} = 79.19\%$, or rephrased, it needs 16 input variables in order to match the performance of the original BDT with 22 input variables.

Due to the rather high statistical uncertainties in the sensitive boosted regions no attempt of BDT optimisation was made, as the low statistics make the optimisation procedure quickly unstable and meaningless. However, a list of variables performing better than the original classification BDT was obtained directly from the TMVA ranking and it is listed

in Appendix A.3, together with respective information on the optimised BDT.

5.1.5. Modelling Uncertainties

It was found that the studied angular distributions showed systematically higher separation power, if MC simulations of the background were generated with SHERPA. In order to estimate the sensitivity of the optimised BDT to modelling uncertainties, the classification BDT, the optimised BDT, and the optimised BDT with minimal number of input variables (16) were trained on the default samples (signal and background modelled with POWHEG + PYTHIA 8) and tested on POWHEG + PYTHIA 8 (signal) and SHERPA (background), aMC@NLO + PYTHIA 8 (signal) and POWHEG + PYTHIA 8 (background) as well as on aMC@NLO + PYTHIA 8 (signal) and SHERPA (background). The result is presented in Figure 5.12.

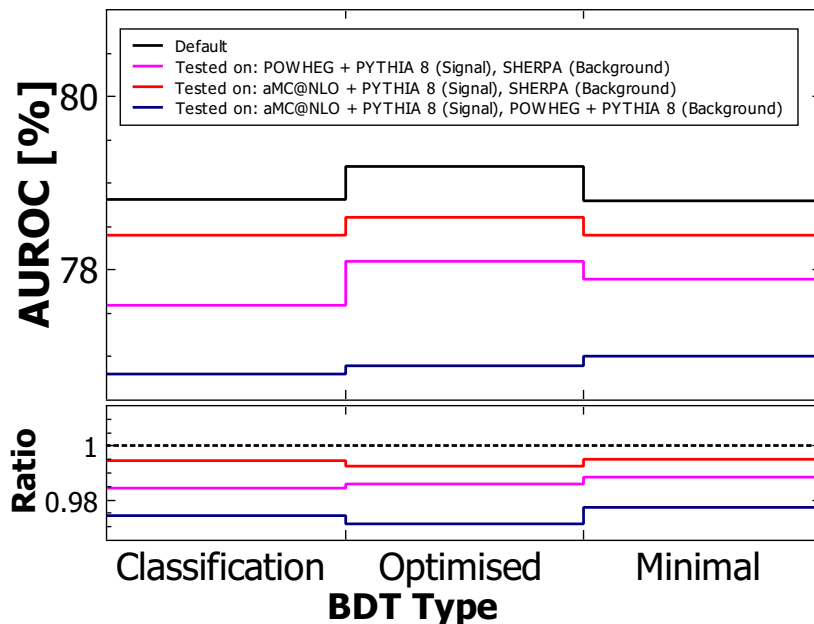


Figure 5.12.: The BDT performance (AUROC) of the classification BDT, the optimised BDT, and the minimal BDT is shown for different MC generators.

As expected, one can see that the BDTs, when tested on different generators, perform slightly worse. From the ratio plot, that shows the performance (AUROC) normalised to the performance obtained when the BDTs are trained and tested on the default samples, it becomes apparent that the optimised minimal BDT has the lowest modelling uncertainty and performs always equal or better than the original classification BDT. While the optimised BDT shows higher AUROC values than the classification BDT in all studied

5. Analysis of Angular Distributions in the $t\bar{t}(H \rightarrow b\bar{b})$ Channel

cases, it has slightly higher modelling uncertainty (except for the signal modelled with POWHEG + PYTHIA 8 and the background modelled with SHERPA). Nevertheless, the overall effect is in the order of a few percent and therefore rather small.

5.2. Dilepton Channel

Analogously to the single lepton channel, respective sets of angular observables were studied in the dilepton channel, including $\cos(\theta_{ij})$, ΔR_{ij} , $\Delta\eta_{ij}$ and $\Delta\phi_{ij}$, where $\{i, j\}$ denote certain top (or anti-top) quark or Higgs boson candidate decay products. However, the exact combinations of decay products differs from the ones used in the single lepton channel. From all possible $\{i, j\}$ combinations, 18 combinations that were found to be particularly sensitive, were chosen for a closer inspection. These combinations are presented in Table 5.3.

Top related	Remaining l^+ related	Remaining b_t related	Remaining Higgs related
$\{i, j\}$	$\{i, j\}$	$\{i, j\}$	$\{i, j\}$
t, \bar{t}	l^+, l^-	b_t, b_H^1	b_H^1, b_H^2
t, l^+	l^+, b_t	b_t, b_H^2	b_H^1, H
t, b_t	$l^+, b_{\bar{t}}$	b_t, H	
$t, b_{\bar{t}}$	l^+, b_H^1		
t, b_H^1	l^+, b_H^2		
t, b_H^2	l^+, H		
t, H			

Table 5.3.: Combinations of top quark, anti-top quark, Higgs boson and/or corresponding decay products. The studied angular observables are then set up between the particles i and j . Notation: t (\bar{t}) is the top (anti-top) quark, decay products from the respective top or anti-top quark are labelled with “ t ” or “ \bar{t} ”, l^\pm are the charged leptons, b means b -jet, H is the Higgs candidate, b_H^1 and b_H^2 are the p_T ordered b -jets from the Higgs candidate.

Thereby, a *nearest* set of angular observables was set up in a similar manner as performed in the single lepton channel in order to benefit from the enhanced signal-background separation that can be obtained through this procedure. The respective particle combinations for the *nearest* set in the dilepton channel are presented in Table 5.4.

Top related	Remaining l^+ related	Remaining b_t related	Remaining Higgs related
$\{i, j; k, l\}$	$\{i, j; k, l\}$	$\{i, j; k, l\}$	$\{i, j; k, l\}$
$t, l^+; \bar{t}, l^-$	$l^+, b_t; l^-, b_{\bar{t}}$	$b_t, b_H^1; b_t, b_H^1$	$b_H^1, H; b_H^2, H$
$t, b_t; \bar{t}, b_{\bar{t}}$	$l^+, b_{\bar{t}}; l^-, b_t$	$b_t, b_H^2; b_t, b_H^2$	
$t, b_{\bar{t}}; \bar{t}, b_t$	$b_t, H; b_t, H$		
$t, b_H^1; \bar{t}, b_H^1$	$l^+, b_H^2; l^-, b_H^2$		
$t, b_H^2; \bar{t}, b_H^2$	$l^+, H; l^-, H$		
$t, H; \bar{t}, H$			

Table 5.4.: Combinations of top quark, anti-top quark, Higgs boson and/or corresponding decay products. The studied angular observables are then set up either between the particles i and j or the particles k and l depending on whether i or k is closer to the Higgs boson candidate in terms of ΔR . The notation is the same as in Table 5.3.

A further set of angular observables was studied. These variables are more complex and require individual definition. The angle $\Omega_t^{t\bar{t}}$ is the angle between the direction of the top quark within the $t\bar{t}$ COM and the direction of the beam axis. The observable Ω_t^{tH} describes the same angle, but with the top quark boosted into the tH system. The observable $\Omega_{b_H^1}$ is the polar angle between the beam line and the leading (p_T) b-jet from the Higgs boson decay. The observables φ_{CP}^* and $\varphi_{\text{CP}}^{\text{Lab}}$ were studied in the dilepton channel using the same definition as in the single lepton channel. Another two variables were considered, which require two leptons to be set up [128]:

$$\omega^{lH}(l^+, l^-) = \arccos \left(\frac{(\vec{p}_H \times \vec{p}_{l^+}) \cdot (\vec{p}_H \times \vec{p}_{l^-})}{|\vec{p}_H \times \vec{p}_{l^+}| \cdot |\vec{p}_H \times \vec{p}_{l^-}|} \right), \quad (5.5)$$

and $\beta\omega^{lH}(l^+, l^-)$, whereas β is defined by the relation:

$$\beta = \text{sgn} \left((\vec{p}_{b_t} \times \vec{p}_{b_{\bar{t}}}) \cdot (\vec{p}_{l^-} \times \vec{p}_{l^+}) \right). \quad (5.6)$$

Thereby, $\omega^{lH}(l^+, l^-)$ can be understood as the angle between the directions of the two lepton momenta projected on the plane that is perpendicular to the momentum direction of the Higgs boson candidate and β is a CP-odd correlation that makes the observable $\beta\omega^{lH}(l^+, l^-)$ sensitive to CP-violating effects [128].

As was done in the single lepton channel, CP sensitive double-polar distributions were studied in a similar manner, however, due to the conditions of the channel, with slightly

5. Analysis of Angular Distributions in the $t\bar{t}(H \rightarrow b\bar{b})$ Channel

different definitions:

$$\begin{aligned}
 & \cos(\theta_{\bar{H}}^{\bar{t}H}) \cos(\theta_t^H) \text{ (db)}, \\
 & \sin(\theta_{\bar{H}}^{t\bar{t}H}) \sin(\theta_{b\bar{t}}^{\bar{t}}) \text{ (sb)}, \\
 & \sin(\theta_{\bar{H}}^{t\bar{t}H}) \cos(\theta_{b\bar{H}}^{\bar{t}}) \text{ (sb)}, \\
 & \sin(\theta_t^{t\bar{t}H}) \sin(\theta_{t^+}^H) \text{ (sb)}, \\
 & \sin(\theta_{\bar{t}}^{t\bar{t}H}) \sin(\theta_{b\bar{H}}^H) \text{ (sb)}, \\
 & \sin(\theta_{\bar{H}}^{t\bar{t}H}) \sin(\theta_{\bar{t}}^{t\bar{t}}) \text{ (db)}.
 \end{aligned}$$

Finally the observable b_4 was also set up using the following definition:

$$b_4 = \frac{p_t^z \cdot p_{\bar{t}}^z}{|\vec{p}_t| \cdot |\vec{p}_{\bar{t}}|}. \quad (5.7)$$

5.2.1. Generator Level Studies

Regarding the most sensitive angular distributions on MC generator particle level in the $t\bar{t}(H \rightarrow b\bar{b})$ dilepton channel, not much changes with respect to the single lepton channel. Nevertheless, the separation power of the angular observables increases slightly, as the jet-parton matching is more likely to be correct because of the lower jet multiplicity. This is exemplified by the outputs of the classification BDT and the angular BDT in the dilepton channel on MC generator particle level. These have slightly higher separation power than in the single lepton channel, even though less input variables are used. In detail, the separation values are 64.0 % (68.8 %) for the classification BDT in the case of the single lepton and dilepton channel respectively and 46.8 % (50.3 %) for the angular BDT in the case of the single lepton and dilepton channel respectively. Thereby, the classification BDTs use the same input variables as in the case of the reconstruction level classification BDTs, however, without the distributions directly related to the event reconstruction, such as the reconstruction BDT score or b -tagging weights. Generator particle level events are selected using the same criteria as described for the single lepton events.

Although rather of academic interest, Figure 5.13 visualises some of the previously discussed effects related to the top quark spin correlations and the corresponding helicity configurations in the top quark chiral limit. The respective plots in Figure 5.13 show the $\cos(\theta_{ll})$ distribution in the dilepton channel, after event selection but on MC truth level, (a) in the laboratory frame and (b) for the leptons boosted into the t/\bar{t} rest frame within the $t\bar{t}$ zero momentum frame (Frame 1). Thereby, θ_{ll} labels the opening angle between the leptons from the top and anti-top quark decays. Without selection cuts one would

expect the distribution in the laboratory frame to peak at $\cos(\theta_U) = \pm 1$, however since parts of the phase space are cut out for $\cos(\theta_U) = 1$, one can see how the event rate drops in this region. Since only top and anti-top quark decay products are studied in these distributions, the separation between signal and background is just due to the top quark spin polarisation effects. By boosting the $\cos(\theta_U)$ distribution from the laboratory frame of reference into the Frame 1, the separation between signal and background increases by a factor of three to $\mathcal{S} = 0.06\%$.

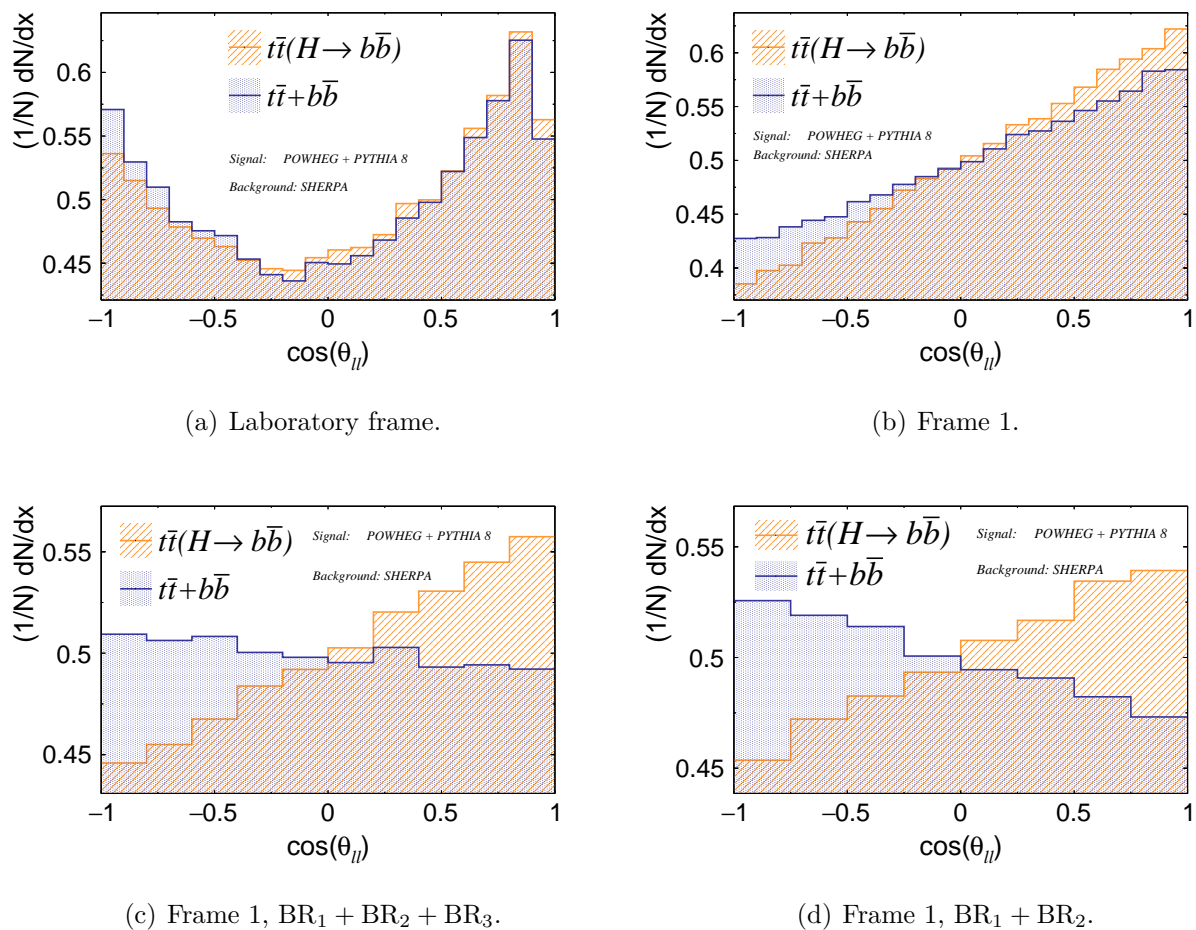


Figure 5.13.: The $\cos(\theta_U)$ distribution for the $t\bar{t}(H \rightarrow b\bar{b})$ signal (orange), modelled with POWHEG + PYTHIA 8 and for the $t\bar{t} + b\bar{b}$ background (blue), modelled with SHERPA 2.2.1 on the MC generator particle level in the laboratory frame of reference (a), in Frame 1 (b), in Frame 1 for events with p_T^t or $p_T^{\bar{t}} > 200$ GeV or $p_T^H > 250$ GeV (c) and for events with p_T^t , $p_T^{\bar{t}}$ or $p_T^H > 250$ GeV (d).

If one then further requires boosted topologies with a top or anti-top quark or a Higgs boson with high transverse momentum, one will see how the $\cos(\theta_U)$ signal and back-

5. Analysis of Angular Distributions in the $t\bar{t}(H \rightarrow b\bar{b})$ Channel

ground distributions gradually approach a complementarity (at least to a certain degree) as expected in the top quark chiral limit. This effect is shown in Figure 5.13 (c) and (d). Thereby, Figure 5.13 (c) visualises the $\cos(\theta_U)$ distribution for events with at least one top or anti-top quark with $p_T > 200$ GeV or a Higgs boson candidate with $p_T > 250$ GeV. The lower right plot (d), shows the same distribution but requiring at least one top, anti-top quark or Higgs boson candidate with $p_T > 250$ GeV. These kinematic cuts see the separation values of the $\cos(\theta_U)$ distributions increase to $\mathcal{S} = 0.19\%$ and $\mathcal{S} = 0.23\%$ respectively. Note that the background distributions presented in Figure 5.13 are modelled with SHERPA 2.2.1. The shown distributions agree with theoretical predictions [83], however, when the $t\bar{t} + b\bar{b}$ distribution is modelled with POWHEG + PYTHIA 8 the effects of the top quark spin polarisation seems to be slightly underestimated, so that the separation between signal and background is even smaller and for reasons of clarity the SHERPA distribution is shown here. Anyway, the respective separation power is, even on the MC generator level, negligible compared to the separation provided by observables constructed from combinations of top quark and Higgs boson decay products. For this reason, $\cos(\theta_U)$ and the other observables constructed from decay products exclusively related to the top quark spin, are useless for the purpose of signal and background separation via a multivariate method.

5.2.2. Reconstruction Level Studies

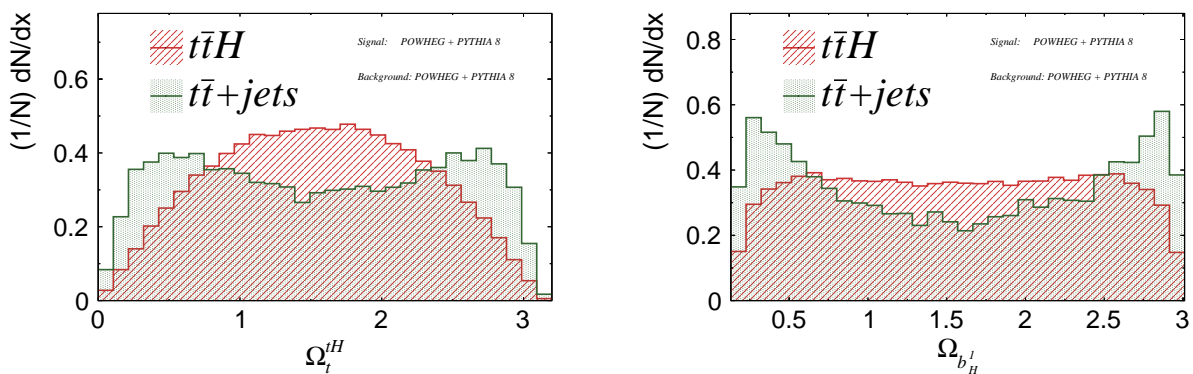
In the dilepton channel the separation power of the studied angular observables is generally higher with respect to the single lepton channel. This is mainly due to the lower jet multiplicity and therefore more precise jet-parton assignments. Analogously to the single lepton channel, the angular distributions show different separation values between signal and background depending on in which signal region they are calculated. Thereby, the regions $\text{SR}_1^{\geq 4j}$ and $\text{SR}_3^{\geq 4j}$ are dominated by the $t\bar{t} + b\bar{b}$ background and therefore more sensitive than the $t\bar{t} + c/\text{light jets}$ dominated region $\text{SR}_2^{\geq 4j}$. Further, the reconstruction with ν -weighting provides an additional increase in signal and background separation with respect to the simple reconstruction.

Simple Reconstruction

When all three dilepton signal regions are considered, the best performing variable from the sets of studied angular observables is $\Delta R_{(b_t, b_{\bar{t}})\text{min}\Delta R(H), b_H^1}$ with $\mathcal{S} = 5.49\%$, if the simple reconstruction method is used. This observable is an angular separation between the b -jet from the top or anti-top quark that is nearest to the Higgs boson candidate (in terms of

ΔR) and the leading (p_T) jet from the Higgs candidate.

If the signal region $\text{SR}_2^{\geq 4j}$ is excluded from consideration, the separation power of the individual angular observables significantly increases in some cases. For example, the variable $\Delta R_{(b_t, b_{\bar{t}})\text{min}\Delta R(H), b_H^1}$, sees an enhancement in separation to $\mathcal{S} = 5.90\%$, however, this variable falls down to the tenth place, if the observables are ranked after their separation power. The most sensitive distribution is then given by $\Delta R_{(t, \bar{t})\text{min}\Delta R(H), H}$, an angle between the Higgs boson candidate and the nearest top or anti-top quark with $\mathcal{S} = 7.26\%$.



(a) Angle between t and the beam direction.

(b) Angle between b_H^1 and the beam direction.

Figure 5.14.: The distributions of the polar angle Ω_t^{tH} between the top quark within the tH COM frame and the beam direction (a) and the respective polar angle of b_H^1 in the laboratory frame (b), calculated in the regions $\text{SR}_1^{\geq 4j}$ and $\text{SR}_3^{\geq 4j}$ using the simple reconstruction, are shown. The $t\bar{t}H$ signal (red) and the $t\bar{t}$ +jets background (green) were modelled with POWHEG + PYTHIA 8.

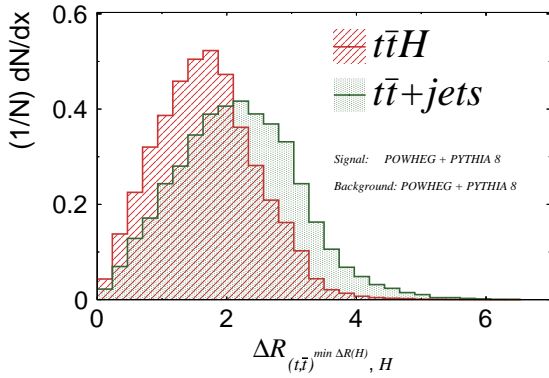
In contrast to the single lepton channel, also variables of non $\cos(\theta)$, $\Delta\eta$ or ΔR type acquire relative high separation power, for example Ω_t^{tH} ($\mathcal{S} = 5.16\%$) or $\Omega_{b_H^1}$ ($\mathcal{S} = 3.42\%$) which are presented in Figure 5.14 (a) and (b) respectively. Thereby, $\Omega_{b_H^1}$ illustrates the difference between the decay products of the scalar Higgs particle and the vector boson (gluon) clearly. One can see how the background distribution peaks near 0 and π , while the signal distribution remains flat. Of course, the dropping event rate in the regions $\Omega_{b_H^1} = 0, \pi$ is due to the event selection cuts.

Reconstruction with ν -weighting

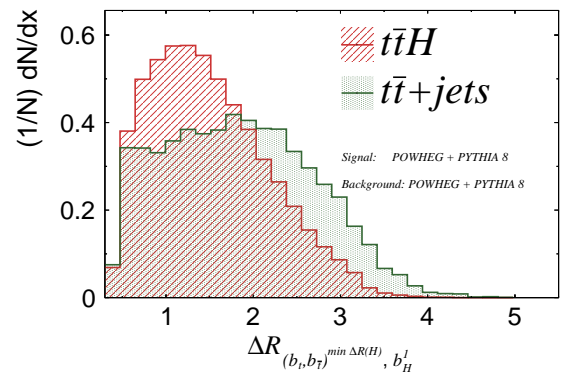
If events are reconstructed using the ν -weighting algorithm instead of the simple reconstruction, most of the studied angular distributions are observed to benefit from this more

5. Analysis of Angular Distributions in the $t\bar{t}(H \rightarrow b\bar{b})$ Channel

elaborate method. As a consequence, the separation power of the most sensitive observable $\Delta R_{(t,\bar{t})\min\Delta R(H),H}$, visualised in Figure 5.15 (a) increases again, in detail to $\mathcal{S} = 7.89\%$. The separation value of the variable $\Delta R_{(b_t,b_{\bar{t}})\min\Delta R(H),b_H^1}$, presented in 5.15 (b), increases to $\mathcal{S} = 6.19\%$. The observable $\Delta\eta_{b_t,b_H^1}$, which provided the most sensitive new angular distribution in the single lepton channel, has the third highest separation power in the dilepton channel, namely $\mathcal{S} = 7.14\%$ when constructed via ν -weighting.



(a) Angle between H and nearest t or \bar{t} .

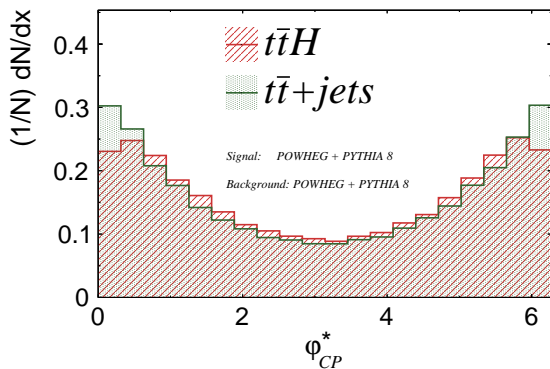


(b) Angle between b_H^1 and b_t or $b_{\bar{t}}$ nearest to H .

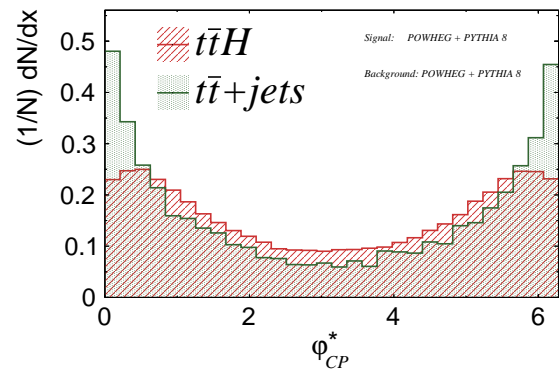
Figure 5.15.: Different ΔR distributions in the dilepton channel for the $t\bar{t}H$ signal (red) and for the $t\bar{t}+\text{jets}$ background (green) on the MC reconstruction level. Events were selected from the signal regions $\text{SR}_1^{\geq 4j}$ and $\text{SR}_3^{\geq 4j}$ and were reconstructed using the ν -weighting method. Signal and background were modelled with POWHEG + PYTHIA 8.

Thereby, all the mentioned separation values related to the reconstruction with ν -weighting were calculated with $\text{SR}_2^{\geq 4j}$ taken out of consideration.

Last but not least, the regions $\text{SR}_1^{\geq 4j} + \text{SR}_3^{\geq 4j}$, reconstructed with the help of ν -weighting, see a separation value of $\mathcal{S} = 2.86\%$ for the φ_{CP}^* distribution, a value that is by a factor of 3.6 larger than the respective one obtained in the single lepton region. Figure 5.16 illustrates the differences between the φ_{CP}^* distributions in the single lepton channel (a) and in the dilepton channel (b). In the dilepton case, it is clearly visible how the shape of the distribution starts to approach the one known from the particle level, while the combinatorial backgrounds in the single lepton channel distort the distributions in such a way that little difference between signal and background is seen on the left plot.



(a) Single lepton channel.



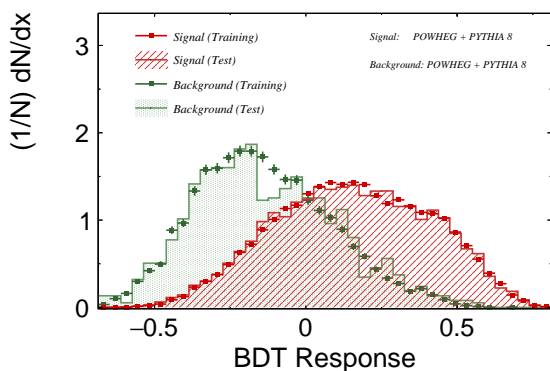
(b) Dilepton channel.

Figure 5.16.: The φ_{CP}^* distribution in the single lepton channel (a) and in the dilepton channel (b) for the $t\bar{t}H$ signal (red) and for the $t\bar{t}+jets$ background (green) on the MC reconstruction level. Signal and background were modelled with POWHEG + PYTHIA 8.

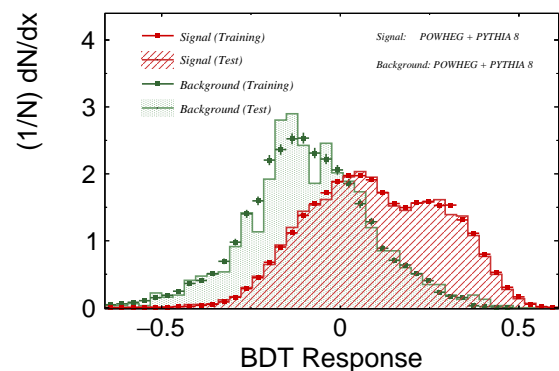
5.2.3. Multivariate Techniques on Reconstruction Level

Simple Reconstruction

Analogously to the single lepton channel, a classification and an angular BDT were set up using the same TMVA settings as introduced before. The BDTs were trained on and



(a) Classification BDT response.



(b) Angular BDT response.

Figure 5.17.: BDT response distributions for the dilepton channel without ν -weighting. All dilepton signal regions are considered. Signal: POWHEG + PYTHIA 8 ($t\bar{t}H$). Background: POWHEG + PYTHIA 8 ($t\bar{t}+jets$).

applied to MC simulations on reconstruction level in the signal regions $SR_1^{\geq 4j} + SR_2^{\geq 4j} +$

5. Analysis of Angular Distributions in the $t\bar{t}(H \rightarrow b\bar{b})$ Channel

$\text{SR}_3^{\geq 4j}$ and $\text{SR}_1^{\geq 4j} + \text{SR}_3^{\geq 4j}$ using the simple reconstruction method. The corresponding BDT response distributions for the first case (inclusive signal regions) are shown in Figure 5.17. Thereby, the plot on the left side (a) represents the response of the ATLAS $t\bar{t}(H \rightarrow b\bar{b})$ classification BDT, which shows a separation value of $\mathcal{S} = (25.5 \pm 1.2)\%$ and an AUROC value of 78.86%. The plot on the right side (b), shows the response of the angular BDT with a separation value of $\mathcal{S} = (20.9 \pm 0.7)\%$ and an AUROC value of 76.06%. As recognisable in Figure 5.17, the background distributions suffer from the low number of statistics available in the corresponding MC samples. The number of test events is by an order of magnitude lower than the number of training events, explaining the visible statistical fluctuations. However, in this case this does not lead to any real problems: while the corresponding separation values of course show higher statistical uncertainties than those obtained with the larger MC samples in the single lepton channel, the respective ROC curves in Figure 5.18 show no significant signs of overtraining apart from the statistical effects in the test curves.

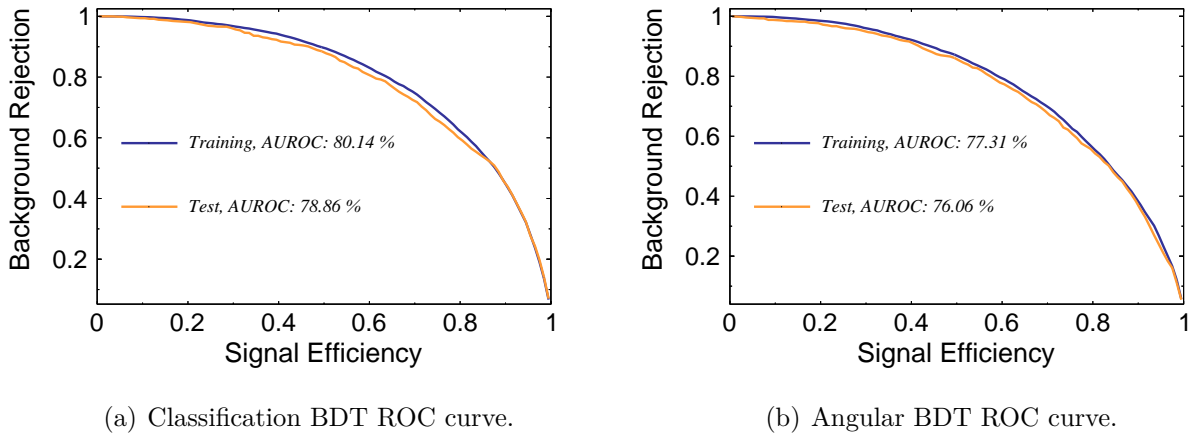


Figure 5.18.: ROC curves from the classification BDT and the angular BDT in the dilepton channel without ν -weighting. All dilepton signal regions are considered. Signal: POWHEG + PYTHIA 8 ($t\bar{t}H$). Background: POWHEG + PYTHIA 8 ($t\bar{t}$ +jets).

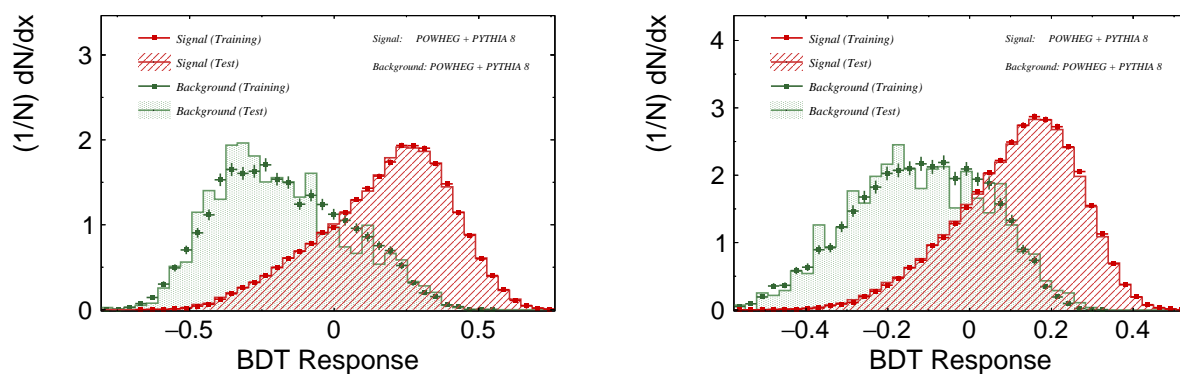
Nevertheless, the BDT response distributions of both, the classification BDT and the angular BDT see a strong increase regarding their separation power, when only the signal regions $\text{SR}_1^{\geq 4j}$ and $\text{SR}_3^{\geq 4j}$ are considered in the training and application of the BDTs. In detail, the separation value of the classification BDT is enhanced by a factor of 1.39 to $\mathcal{S} = (35.4 \pm 1.5)\%$ and the separation power of the angular BDT is enhanced by a factor of 1.45 to a value of $\mathcal{S} = (30.4 \pm 1.2)\%$. These results also imply an increase of the corresponding ROC curve integrals, which are 84.21% and 81.53% for the classification

BDT and the angular BDT, respectively.

Here, the room for optimisation is potentially larger than in case of the single lepton channel, as the separation values provided by combined BDTs that join the classification and angular BDT input variables, are $\mathcal{S} = (29.2 \pm 0.9) \%$ and $\mathcal{S} = (39.2 \pm 1.5) \%$ in case of considering all signal regions or only $\text{SR}_1^{\geq 4j}$ and $\text{SR}_3^{\geq 4j}$ respectively. The corresponding AUROC values are 81.09 % and 86.01 %.

Reconstruction with ν -weighting

Last but not least, the classification BDT and the angular BDT were trained on and applied to MC simulations on reconstruction level in the regions $\text{SR}_1^{\geq 4j} + \text{SR}_3^{\geq 4j}$ using the reconstruction via the ν -weighting method. The respective response distributions for the classification and the angular BDT are shown in Figure 5.19 (a) and (b) respectively. Thereby, a separation value of $\mathcal{S} = (40.1 \pm 2.1) \%$ is obtained in the case of the classification BDT and $\mathcal{S} = (36.5 \pm 1.6) \%$ in the case of the angular BDT. The respective AUROC values are 86.38 % and 84.71 %. If the input variables of both BDTs are joined into a combined BDT, another significant gain in separation power is observed, in fact $\mathcal{S} = (46.6 \pm 2.4) \%$ and AUROC = 89.06 %, as visualised in Figure 5.20 (a) and (b), respectively.



(a) Classification BDT response.

(b) Angular BDT response.

Figure 5.19.: BDT response distributions for the dilepton channel with ν -weighting. Only the signal regions $\text{SR}_1^{\geq 4j}$ and $\text{SR}_3^{\geq 4j}$ are considered. Signal: POWHEG + PYTHIA 8 ($t\bar{t}H$). Background: POWHEG + PYTHIA 8 ($t\bar{t} + \text{jets}$).

5. Analysis of Angular Distributions in the $t\bar{t}(H \rightarrow b\bar{b})$ Channel

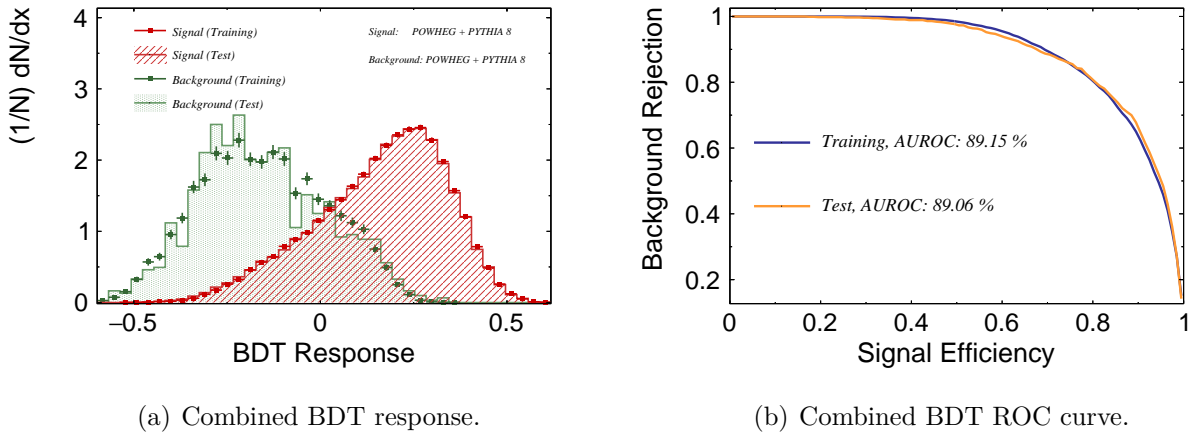


Figure 5.20.: BDT response distribution and ROC curve for the combined BDT in the dilepton channel with ν -weighting. Only the signal regions $SR_1^{\geq 4j}$ and $SR_3^{\geq 4j}$ are considered. Signal: POWHEG + PYTHIA 8 ($t\bar{t}H$). Background: POWHEG + PYTHIA 8 ($t\bar{t}$ +jets).

5.2.4. Optimised Classification BDT

Analogously to the single lepton channel, an optimised classification BDT was built up in the dilepton channel considering all three signal regions (without ν -weighting). The optimisation procedure is based on the TMVA ranking as previously explained. The result is presented in Figure 5.21, that shows the number of input variables to the optimised classification BDT as a function of AUROC and separation. It was found that an optimised BDT with a minimum of ten input variables matches the performance of the original classification BDT with 21 variables. However, it is important to note that the optimisation suffers from low statistics in the dilepton event files and it is unlikely that one can really remove that much variables without unwanted side effects. For example, it was found that, in contrast to the single lepton channel, the optimised BDT and the optimised BDT with a minimal number of input variables, perform worse than the original classification BDT when tested on samples modelled with different generators, such as aMC@NLO or SHERPA. Nevertheless, this optimisation gives an indication which variables can potentially be used to improve the original classification BDT.

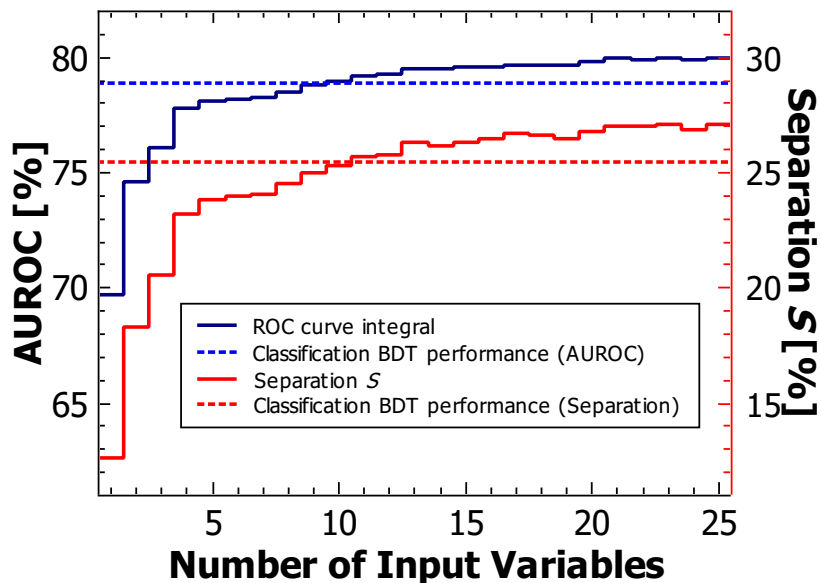


Figure 5.21.: Number of input variables to the (optimised) classification BDT in the dilepton channel, considering all dilepton signal regions, as a function of the performance, measured in AUROC values (blue) and separation values (red).

For the same reason of low statistics, no attempt was made to optimise the classification BDT when taking signal region $SR_2^{\geq 4j}$ out of consideration or when the events are reconstructed with ν -weighting (in some events no solutions can be found for the ν four-momenta, therefore the statistics is further reduced). However, a list of variables that outperform the original classification BDT was obtained directly from the TMVA ranking and it is presented together with the respective information on the optimised BDT in Appendix A.3.

6. The $t\bar{t}(H \rightarrow b\bar{b})$ Process with Modified CP-Odd and CP-Mixed $t\bar{t}H$ Yukawa Couplings

As briefly addressed in the introduction, the CP violating mechanisms within the SM are not sufficient to describe the observed baryon asymmetry in the universe. For this reason, searches for new sources of CP violation are ongoing. Studies in the Higgs sector are particularly of great importance because there are theoretical extensions of the SM that predict multiple Higgs doublets [129] that would introduce CP violating effects through pseudo-scalar Higgs couplings. Despite the fact that the hypothesis of a purely pseudo-scalar 125 GeV Higgs particle is experimentally excluded with a confidence level of 99.98 % [130–132] from studies on Higgs-to-vector-boson decays performed by ATLAS and CMS at $\sqrt{s} = 7$ and 8 TeV, the results still allow for an indefinite CP quantum number through mixing of CP-even and CP-odd components. In fact, measurements related to Higgs-to-vector-boson decays can only project out CP-even components but not a mixed one as no CP-odd tree-level couplings to vector bosons are allowed. Hence, they could only occur through loops and would be suppressed. Measuring the Yukawa couplings between the Higgs boson and the fermions is therefore of prime interest, especially as it would also be possible that the Higgs-to-fermion coupling differs among the fermion flavours [133]. Measurements of the $t\bar{t}H$ vertex are sensitive to the CP properties of the Higgs boson. The corresponding Lagrangian of the $t\bar{t}H$ coupling can be expressed as [125]

$$\mathcal{L} = \kappa Y_t \bar{t} (\cos(\alpha) + i \gamma_5 \sin(\alpha)) t H. \quad (6.1)$$

Thereby, the top quark Yukawa coupling is described by Y_t , whereas α is a CP phase that describes the degree of mixing between CP-even and CP-odd components. The SM scalar Yukawa coupling is then obtained by $|\cos(\alpha)| = 1$, the pure pseudo-scalar case is obtained with $\cos(\alpha) = 0$.

All observables used as inputs to the ATLAS $t\bar{t}(H \rightarrow b\bar{b})$ classification BDT and the angular BDT, as introduced in the previous chapter, were studied regarding their sensitivity to

6. The $t\bar{t}(H \rightarrow b\bar{b})$ Process with Modified CP-Odd and CP-Mixed $t\bar{t}H$ Yukawa Couplings

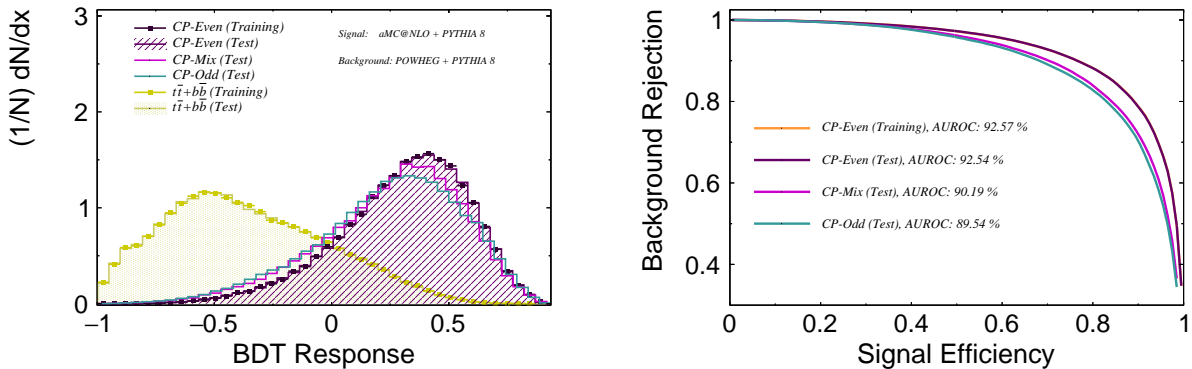
a possible non-SM CP nature of the Higgs boson. Apart from the SM CP-even sample, a CP-mixed ($\cos(\alpha) = 1/\sqrt{2}$) and a purely CP-odd sample, all modelled with aMC@NLO + PYTHIA 8 were studied and compared to the SM $t\bar{t} + b\bar{b}$ background, modelled with POWHEG + PYTHIA 8. Furthermore, the classification and reconstruction BDTs are studied regarding a possible bias towards a SM model Higgs CP value.

6.1. Bias towards Standard Model Expectation

A strong SM bias of important tools for the $t\bar{t}(H \rightarrow b\bar{b})$ search, such as the reconstruction or classification BDTs, would be problematic because possible non-SM signals would be potentially classified as background and in this way, be hidden from observation.

6.1.1. Classification BDT

On MC generator particle level, a small bias towards the SM Higgs CP quantum number was observed in the classification BDTs of the single and dilepton channel, as well as in the optimised BDTs. Thereby, the BDTs were trained with the same settings as described in the previous chapter using the $t\bar{t}(H \rightarrow b\bar{b})$ CP-even sample as signal and the default POWHEG + PYTHIA 8 sample for the $t\bar{t} + b\bar{b}$ background.



(a) Classification BDT response.

(b) Classification BDT ROC curve.

Figure 6.1.: BDT response distribution and ROC curve for the classification BDT in the dilepton channel on MC generator particle level. Distributions related to different Higgs boson CP values are shown. Signal: aMC@NLO + PYTHIA 8 ($t\bar{t}(H \rightarrow b\bar{b})$). Background: POWHEG + PYTHIA 8 ($t\bar{t} + b\bar{b}$).

The trained classifier was then applied to the CP-mixed and CP-odd samples, as visualised

in Figure 6.1 for the case of the dilepton classification BDT. In all studied cases (single and dilepton channel, original and optimised BDTs) the observed discrepancy between the CP-even and CP-odd distribution manifests in a 3-4% AUROC and 8-10% \mathcal{S} difference. In other words, roughly 7.5% (5.8%) fewer events would be classified as signal in the case of the CP-odd (CP-mixed) distribution in the dilepton channel, if a cut was made on the BDT output at the optimal cut value (where the signal efficiency equals the background rejection) and assuming a S/B ratio of 1 before the classification.

While this effect does not appear to be severe on the MC generator particle level, it still should be taken seriously and it needs more in depth studies on the reconstruction level where a performance drop in the order of 3-4% AUROC would be significant.

The CP bias might be reduced by choosing input variables with low sensitivity to the different CP scenarios but rather high separation between signal and background, however this selection is beyond the scope of this analysis.

6.1.2. Reconstruction BDT

A respective bias in the reconstruction BDT would be even more problematic as it would distort event kinematics towards the SM expectation. The ATLAS $t\bar{t}(H \rightarrow b\bar{b})$ reconstruction BDT in the single and dilepton channel was studied in relation to a possible bias towards the SM Higgs CP quantum number on MC generator particle level.

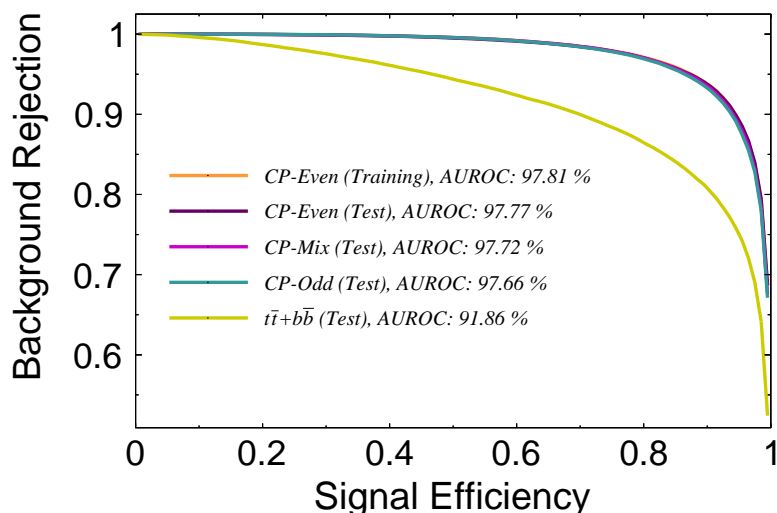


Figure 6.2.: ROC curve for the reconstruction BDT in the dilepton channel on MC generator particle level. Distributions related to different Higgs boson CP values are shown. Signal: Right combination of particles. Background: Wrong combinations of particles.

6. The $t\bar{t}(H \rightarrow b\bar{b})$ Process with Modified CP-Odd and CP-Mixed $t\bar{t}H$ Yukawa Couplings

The reconstruction BDT is trained on certain distributions, as described in Chapter 4.5.1, from the CP-even sample. Thereby, the BDT “signal” uses the top quark, Higgs boson and W boson candidates made from the correct jet and lepton combinations and the “background” is made from all the possible incorrect combinations. Then, the trained classifier is applied to the CP-mixed, CP-odd and to the $t\bar{t} + b\bar{b}$ samples.

Neither in the single lepton nor in the dilepton channel a noteworthy bias was found. As apparent from the ROC curves in Figure 6.2 for the dilepton channel, the change in performance when testing on the CP-mixed or CP-odd sample is in the order of 0.1% AUROC, which is negligible. Similar results were obtained for the single lepton channel. The drop in performance when testing on the $t\bar{t} + b\bar{b}$ samples is actually expected and in fact it is the reason why the respective BDT output, shown in Figure 6.3, can be used to discriminate signal and background, as is done in the classification BDT.

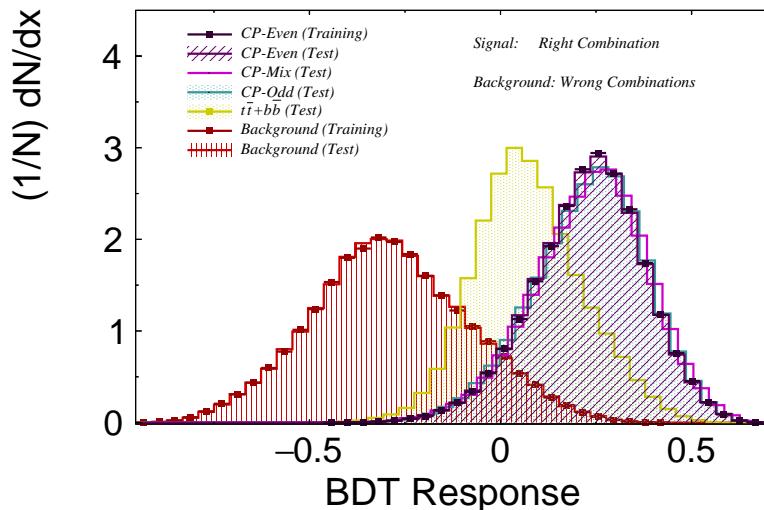


Figure 6.3.: BDT response distribution for the reconstruction BDT in the dilepton channel on MC generator particle level. Distributions related to different Higgs boson CP values are shown. Signal: Right combination of particles. Background: Wrong combinations of particles.

The fact that the reconstruction BDT on particle level is unbiased is promising. The main difference between the particle level and the truth-matched reconstruction level kinematics that are used for the BDT training in the $t\bar{t}(H \rightarrow b\bar{b})$ analysis, are detector resolution effects. These should not distort the BDT responses too much and therefore one would expect the reconstruction BDT, as it is used in the ATLAS $t\bar{t}(H \rightarrow b\bar{b})$ search, to have low CP bias.

6.2. Determination of the Higgs Boson CP Quantum Number in $t\bar{t}H$ Interactions

In order to extract information about the CP nature of the $t\bar{t}H$ coupling, one has to find observables with preferably high separation between CP-even and CP-odd¹ distributions. CP-sensitive observables such as $\beta\omega^{lH}(l^+, l^-)$ or φ_{CP}^* were found to have $\mathcal{S} = 1.0\%$ and $\mathcal{S} = 3.3\%$ ($\mathcal{S} = 2.5\%$) separation between CP-even and CP-odd distributions in the dilepton (single lepton) channel respectively. The double polar distributions of the type $f(\theta_Y^X) \cdot g(\theta_{Y'}^{X'})$ with $f, g \in \{\sin, \cos\}$, as introduced in the previous chapter, showed separation powers of $\mathcal{S} = 0.1\text{--}1.7\%$ in both channels. However, the most sensitive distributions turned out to be the $t\bar{t}$ related angular variables $\Omega_t^{t\bar{t}}$, $\Delta\eta_{t\bar{t}}$ and b_4 with $\mathcal{S} = 12.9\%$ ($\mathcal{S} = 12.5\%$), $\mathcal{S} = 12.1\%$ ($\mathcal{S} = 11.6\%$) and $\mathcal{S} = 8.4\%$ ($\mathcal{S} = 7.7\%$) in the dilepton (single lepton) channel respectively. The former distribution is presented in Figure 6.4. One can see that the angle $\Omega_t^{t\bar{t}}$, in this study applied for the first time to CP-mixed and CP-odd $t\bar{t}H$ events, allows for a clear distinction between the CP-even, CP-mixed and CP-odd cases.

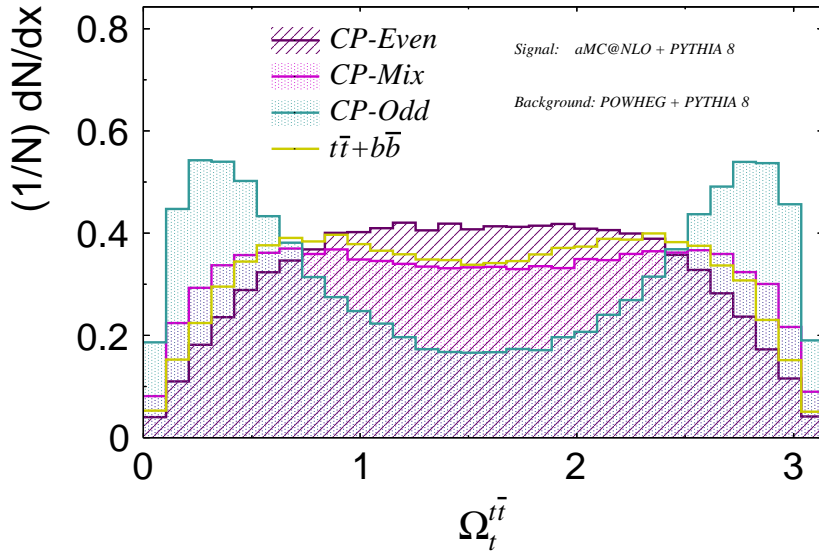


Figure 6.4.: The $\Omega_t^{t\bar{t}}$ distribution for a CP-even (purple), CP-mixed (pink) and CP-odd (cyan) $t\bar{t}(H \rightarrow b\bar{b})$ signal and for the $t\bar{t} + b\bar{b}$ background (yellow) on the MC generator particle level in the dilepton channel. Signal: aMC@NLO + PYTHIA 8 ($t\bar{t}(H \rightarrow b\bar{b})$). Background: POWHEG + PYTHIA 8 ($t\bar{t} + b\bar{b}$).

¹It was found that the shape of CP-mixed distributions is generally “in between” the CP-even and CP-odd distributions and the separation is therefore lower in the case of CP-even and CP-mixed than for CP-even and CP-odd.

6. The $t\bar{t}(H \rightarrow b\bar{b})$ Process with Modified CP-Odd and CP-Mixed $t\bar{t}H$ Yukawa Couplings

The $t\bar{t} + b\bar{b}$ background is thereby found to look similar to the CP-mixed distribution. The observable $\Delta\eta_{t\bar{t}}$ is visualised in Figure 6.5. While the separation between the CP-even and the CP-odd distribution is in the order of 12% in both the single and dilepton channel, the respective separation between the CP-even and the CP-mixed distribution is only 2%. Something similar is observed in the case of the variable b_4 , visualised in Figure 6.6, which shows a separation value of roughly 1% between the CP-even and CP-mixed distributions.

Although the CP-mixed sample is fully mixed with equal CP-even and CP-odd components, the shape of the CP-mixed distributions generally tend to be more similar to the CP-even case than to the CP-odd case.

In order to maximise the sensitivity to possible non-SM CP components in the $t\bar{t}H$ coupling, one can combine several observables with the help of multivariate techniques, in this case a respective BDT was chosen.

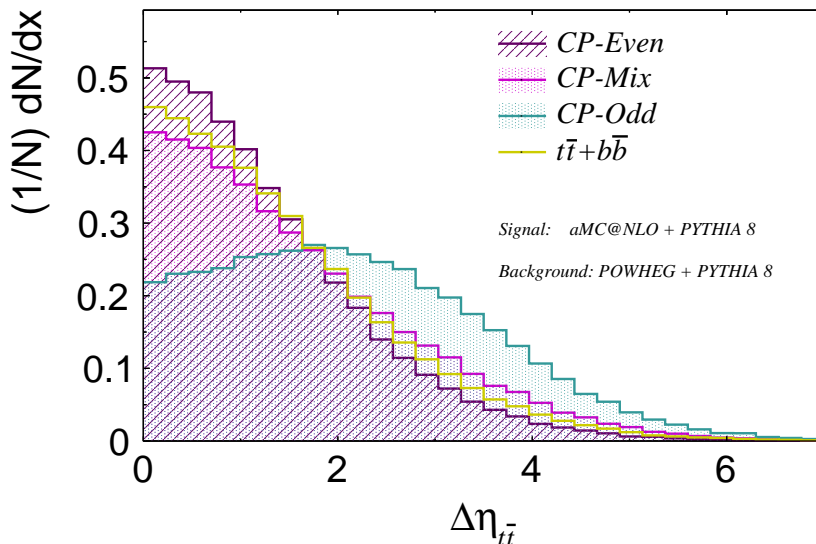


Figure 6.5.: The $\Delta\eta_{t\bar{t}}$ distribution for a CP-even (purple), CP-mixed (pink) and CP-odd (cyan) $t\bar{t}(H \rightarrow b\bar{b})$ signal and for the $t\bar{t} + b\bar{b}$ background (yellow) on the MC generator particle level. Signal: aMC@NLO + PYTHIA 8 ($t\bar{t}(H \rightarrow b\bar{b})$). Background: POWHEG + PYTHIA 8 ($t\bar{t} + b\bar{b}$).

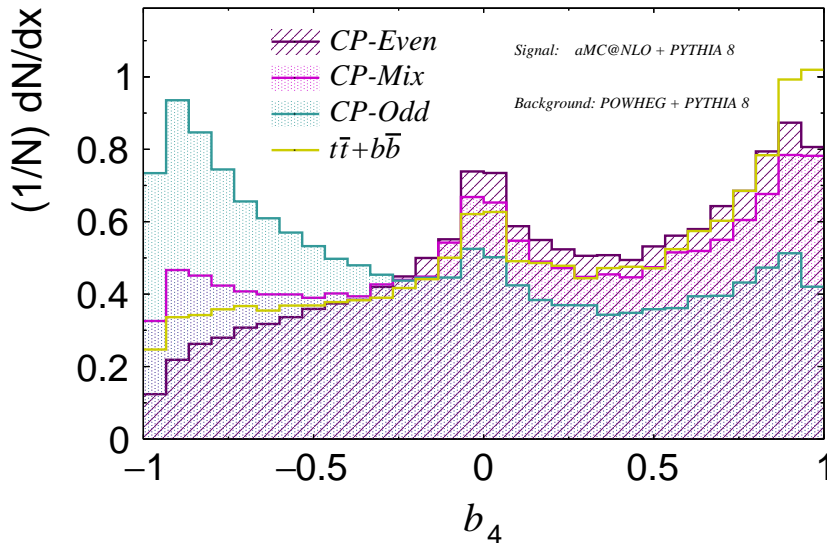


Figure 6.6.: The b_4 distribution for a CP-even (purple), CP-mixed (pink) and CP-odd (cyan) $t\bar{t}(H \rightarrow b\bar{b})$ signal and for the $t\bar{t} + b\bar{b}$ background (yellow) on the MC generator particle level. Signal: aMC@NLO + PYTHIA 8 ($t\bar{t}(H \rightarrow b\bar{b})$). Background: POWHEG + PYTHIA 8 ($t\bar{t} + b\bar{b}$).

6.2.1. CP Determination BDT

Two BDTs, one for the single lepton and one for the dilepton channel, in the following referred to as *CP determination BDTs*, were trained for the purpose of differentiating between the CP-even, CP-mixed and CP-odd hypotheses. First, all studied observables from the angular and also from the classification BDT were used together as input variables for the respective BDT. Then the 20 most important variables were identified from the TMVA rankings and selected for the final list of input variables. The response distributions of the CP determination BDT in the single lepton channel are shown in Figure 6.7. There, the separation between the CP-even and CP-odd distributions is $\mathcal{S} = 21.0\%$, the separation between the CP-even and CP-mixed distributions is $\mathcal{S} = 3.8\%$ and the separation is $\mathcal{S} = 11.1\%$ between the CP-even signal and the $t\bar{t} + b\bar{b}$ background. This would correspond to a signal (CP-even) to background (CP-odd) ratio of roughly 2.3, when cutting on the BDT output at the optimal value.

As expected, the CP-mixed distribution peaks in between the CP-even and CP-odd distributions, with a separation of $\mathcal{S} = 8.2\%$ and $\mathcal{S} = 5.1\%$ with respect to the CP-odd and the $t\bar{t} + b\bar{b}$ distribution respectively. The separation between the CP-odd and the $t\bar{t} + b\bar{b}$ distribution is found to be $\mathcal{S} = 7.6\%$. In the dilepton channel the separation values are slightly higher, with the separation between CP-even and CP-odd distribution

6. The $t\bar{t}(H \rightarrow b\bar{b})$ Process with Modified CP-Odd and CP-Mixed $t\bar{t}H$ Yukawa Couplings

being $\mathcal{S} = 23.5\%$. The list of input variables to CP determination BDTs is given in the Appendix.

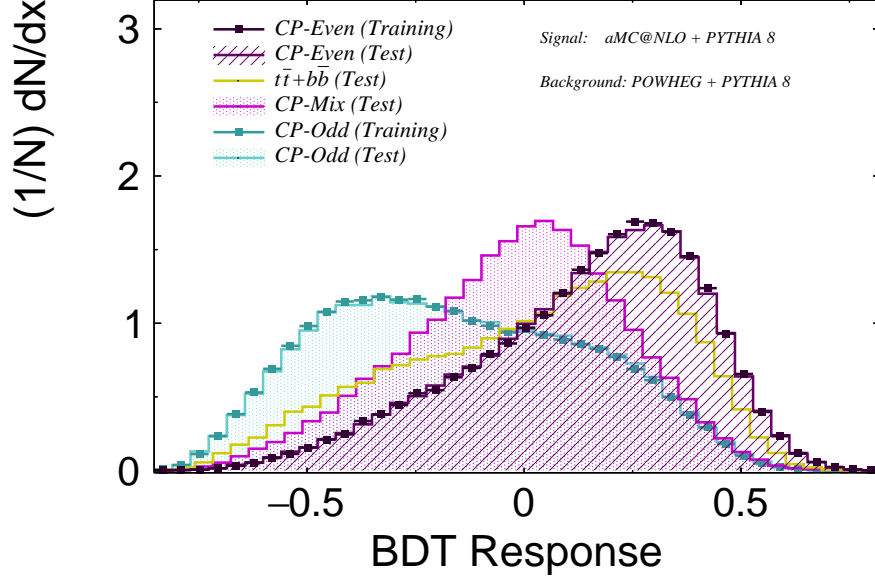


Figure 6.7.: BDT response distribution for the CP determination BDT in the single lepton channel on MC generator particle level. Distributions related to different Higgs boson CP values and the $t\bar{t} + b\bar{b}$ background are shown. Signal: $aMC@NLO + PYTHIA\ 8$ ($t\bar{t}(H \rightarrow b\bar{b})$). Background: $POWHEG + PYTHIA\ 8$ ($t\bar{t} + b\bar{b}$).

7. Results and Outlook

Within this analysis different sets of angular observables were studied on the MC reconstruction level with regard to their potential power to improve the event classification or rather the S/B ratio in the ATLAS $t\bar{t}(H \rightarrow b\bar{b})$ search. In detail, around 200 different angular variables were explored in the $t\bar{t}(H \rightarrow b\bar{b})$ single and dilepton channel each respectively. The variables were joined with the input variables of the original ATLAS classification BDTs into combined BDTs, which were then subtractively optimised (in certain signal regions) in order to obtain the maximum possible separation power from a minimal set of input variables. Thereby, the S/B ratio of the classification BDT output in the single lepton (dilepton) channel was, depending on the chosen signal and phase space regions, enhanced by a factor of up to 1.8 (3.2) when cut on the BDT output distributions at the point of highest signal-to-background difference and assuming a S/B ratio of 1 before the classification BDT. However, as the ATLAS $t\bar{t}(H \rightarrow b\bar{b})$ search does not cut on the classification BDT score, but rather uses it as input for a profile likelihood fit, it is more conclusive to specify the number of variables that can be removed from the original classification BDT, while keeping the same performance. Reducing the number of input variables is preferable over a higher performance, as the reduction leads to a decrease in systematic uncertainties, which are dominating the $t\bar{t}(H \rightarrow b\bar{b})$ search at the moment. Nevertheless, it was found that the optimised BDT in the single lepton channel needs at least 16 variables to perform as well as the original classification BDT with 22 input variables, when considering only the signal regions dominated by the $t\bar{t} + b\bar{b}$ background. Lower modelling uncertainties were observed in the case of the optimised BDT. In the dilepton channel, considering all signal regions, the number of input variables could be reduced from 21 to ten. However, the presented lists of optimised input variables are not to be understood as final sets providing optimal performance, but rather as recommendations for well performing angular observables. How much these help to enhance the sensitivity to the $t\bar{t}(H \rightarrow b\bar{b})$ needs to be analysed in more detail, as the impact of the respective systematic uncertainties on the post-fit performances is left open to future studies. Further, one might enhance the $t\bar{t}(H \rightarrow b\bar{b})$ reconstruction BDTs by including the observable φ_{CP}^* , as it has low correlation with the Higgs candidate mass and it was

7. Results and Outlook

shown to be very sensitive to incorrect jet-parton assignments, especially in case of the $t\bar{t} + b\bar{b}$ background.

Furthermore, $t\bar{t}(H \rightarrow b\bar{b})$ events with non-SM $t\bar{t}H$ Yukawa coupling were studied on MC generator particle level. Thereby, even, mixed and odd Higgs boson CP quantum numbers were considered and compared to the $t\bar{t} + b\bar{b}$ background. It was found that the ATLAS $t\bar{t}(H \rightarrow b\bar{b})$ classification BDT suffers from a small bias towards the SM Higgs boson CP quantum number expectation. Depending on the degree of CP-mixing, between 6% and 8% fewer signal events would be classified as signal by the classification BDT if the respective Higgs boson CP quantum number was of non SM nature, assuming a S/B ratio of 1 before the classification BDT. On the other hand, no CP bias was found in the reconstruction BDTs.

The same angular observables as used in the first part of this analysis, were studied with regard to their sensitivity to CP-even, CP-mixed and CP-odd Higgs CP quantum numbers. It was found that the distributions with highest sensitivity are exclusively related to the $t\bar{t}$ system or the corresponding top quark spin analysers. BDTs were trained to differentiate between the different possible CP hypotheses. Thereby separation values of $\mathcal{S} = 21.0\%$ ($\mathcal{S} = 23.5\%$) between the CP-even and CP-odd BDT response distributions were achieved in the single lepton (dilepton) channel.

In future analyses respective studies have to be performed on the MC reconstruction level in order to estimate the impact of the CP bias of the classification BDT as well as the sensitivity of the CP determination BDT, taking the detector resolution effects and the combinatorial backgrounds from incorrect reconstruction fully into account.

A. Appendix

In the following sections, the input variables to all considered BDTs are presented. Regarding the notation, in the dilepton channel, top quark (anti-top quark) decay products are labelled with a lower index t (\bar{t}). In the lepton + jets channel, the leptonically (hadronically) decaying top quark, anti-top quark or W boson are labelled with a lower index “lep” (“had”), q_1 and q_2 refer to the p_T -ordered light jets from the hadronically decaying W boson. In both channels, b means a b -jet, l means a charged lepton, and b_H^1 as well as b_H^2 are the p_T -ordered decay products from the Higgs boson candidate.

The input variables to the reconstruction BDTs are given in Table A.1. One can see that some minimal or maximal ΔR variables are considered, however over which particles the respective value is minimised or maximised has to be defined in each case individually. For $\Delta R(b(t, \bar{t}), l)$, the minimal or maximal value from all possible lepton and b -jet (originating from the top or anti-top quark) permutations is taken. In the case of $\Delta R(H, l)$ and $\Delta R(H, b(t, \bar{t}))$, the minimal or maximal value over the two leptons or b -jets from the top or anti-top quark decay is taken respectively. In the case of $\min \Delta R(b(t_{\text{had}}), q(W_{\text{had}}))$, the minimal value over the light jets from the hadronically decaying W^\pm boson is taken. The input variables for the classification BDTs are given in Table A.2 for the single lepton channel and in Table A.3 for the dilepton channel. Thereby, check marks are used in order to indicate whether a variable is used in a respective region or not. Check marks denoted with (without) a “*” mean that the information from the reconstruction BDT with (without) additional Higgs information is used and in the case of two stars “**”, the information from both BDTs is used. In the case of variables denoted with “max p_T ”, the vector sum p_T is taken.

Table A.4 shows variables defined in the single lepton channel that are currently not used in the ATLAS $t\bar{t}(H \rightarrow b\bar{b})$ classification BDT, but which are used in this study as additional input variables for the combined BDT, hence (potentially) also for the optimised BDTs.

A.1. Input Variables to the Reconstruction BDTs

BDT	Dilepton channel	Lepton + jets channel
Topological information from $t\bar{t}$	$\Delta R(b_t, l_t)$ $\Delta R(b_{\bar{t}}, l_{\bar{t}})$ $m(b_t, l_t)$ $m(b_{\bar{t}}, l_{\bar{t}})$ $p_T(b_t, l_t)$ $p_T(b_{\bar{t}}, l_{\bar{t}})$ $\Delta R(b_t, b_{\bar{t}})$ $ \Delta R(b_t, l_t) - \Delta R(b_{\bar{t}}, l_{\bar{t}}) $ $\min \Delta R(b(t, \bar{t}), l)$ $\max \Delta R(b(t, \bar{t}), l)$	$m(t_{\text{lep}})$ $m(t_{\text{had}})$ $m(t_{\text{incl}})$ $m(W_{\text{had}})$ $m(W_{\text{had}} + b(t_{\text{lep}}))$ $m(q_1(W_{\text{had}}) + b(t_{\text{lep}}))$ $m(W_{\text{lep}} + b(t_{\text{had}}))$ $\Delta R(W_{\text{had}}, b(t_{\text{had}}))$ $\Delta R(q_1(W_{\text{had}}), b(t_{\text{had}}))$ $\Delta R(W_{\text{had}}, b(t_{\text{lep}}))$ $\Delta R(q_1(W_{\text{had}}), b(t_{\text{lep}}))$ $\Delta R(l, b(t_{\text{lep}}))$ $\Delta R(l, b(t_{\text{had}}))$ $\Delta R(b(t_{\text{lep}}), b(t_{\text{had}}))$ $\Delta R(q_1(W_{\text{had}}), q_2(W_{\text{had}}))$ $\Delta R(b(t_{\text{had}}), q_1(W_{\text{had}}))$ $\Delta R(b(t_{\text{had}}), q_2(W_{\text{had}}))$ $\min \Delta R(b(t_{\text{had}}), q(W_{\text{had}}))$ $\Delta R(l, b(t_{\text{lep}})) -$ $\Delta R(b(t_{\text{had}}), q_1(W_{\text{had}}))$
Topological information from Higgs	m_H $\Delta R(b_H^1, b_H^2)$ $\Delta R(H, t\bar{t})$ $ \Delta R(b_H^1, b_H^2) - \Delta R(b_t, b_{\bar{t}}) $ $\min \Delta R(H, l)$ $\max \Delta R(H, l)$ $\min \Delta R(H, b(t, \bar{t}))$ $\max \Delta R(H, b(t, \bar{t}))$	m_H $\Delta R(b_H^1, b_H^2)$ $\Delta R(b_H^1, l)$ $m(H + q_1(W_{\text{had}}))$ $\Delta R(b_H^1, b(t_{\text{lep}}))$ $\Delta R(b_H^1, b(t_{\text{had}}))$

Table A.1.: The input variables for the reconstruction BDTs of the ATLAS $t\bar{t}(H \rightarrow b\bar{b})$ search.

A.2. Input Variables to the Classification BDTs

Variable	Explanation	Region	
		$\text{SR}_{1,2}^{5j}$	$\text{SR}_{1,2,3}^{\geq 6j}$
General variables			
$\Delta R_{bb}^{\text{avg}}$	Average over ΔR of all pairs of b -tagged jets.	✓	✓
$\Delta R_{bb}^{\text{max } p_T}$	ΔR of a pair of b -tagged jets with maximum p_T .	–	✓
$\Delta \eta_{jj}^{\text{max}}$	Maximum $\Delta \eta$ between any pair of jets.	✓	✓
$m_{bb}^{\text{min } \Delta R}$	Invariant mass of b -jet pair with minimum ΔR .	–	✓
$m_{jj}^{\text{min } \Delta R}$	Invariant mass of jet pair with minimum ΔR .	✓	–
$N_{bb}^{\text{Higgs } 30}$	Number of b -jet pairs with $ m_{bb} - m_H < 30$ GeV.	✓	✓
H_T^{had}	Scalar sum over all jet p_T .	✓	–
$\Delta R_{l,bb}^{\text{min } \Delta R}$	ΔR of lepton and the b -jet pair with minimum ΔR .	✓	–
Aplanarity	$1.5 \lambda_2$, 2 nd eigenvalue of the momentum tensor [134] (jets).	✓	✓
H_1	Second FOX-WOLFRAM moment [135] (jets + lepton).	✓	✓
Reconstruction BDT variables			
BDT score	Output from the reconstruction BDT.	✓*	✓*
$m(b_H^1, b_H^2)$	Invariant mass of the b -jets from the Higgs candidate.	✓	✓
$m(H, b(t_{\text{lep}}))$	Invariant mass of Higgs candidate and the b -jet from t_{lep} .	–	✓
$\Delta R(b_H^1, b_H^2)$	ΔR between the b -jets from the Higgs candidate.	✓	✓
$\Delta R(H, t\bar{t})$	ΔR between the Higgs candidate and the $t\bar{t}$ system.	✓*	✓*
$\Delta R(H, t_{\text{lep}})$	ΔR between the Higgs candidate and t_{lep} .	–	✓
$\Delta R(H, b(t_{\text{had}}))$	ΔR between the Higgs candidate and the b -jet from t_{had} .	✓*	–
B -tagging related variables			
$w_{b\text{-tag}}^{\text{Higgs}}$	Sum of b -tagging discriminants (from b_H^1 and b_H^2).	✓	✓
B_{jet}^3	3 rd largest jet b -tagging discriminant.	✓	✓
B_{jet}^4	4 th largest jet b -tagging discriminant.	✓	✓
B_{jet}^5	5 th largest jet b -tagging discriminant.	✓	✓
Other variables			
LHD	Output from the likelihood discriminant.	✓	✓
MEM_{D1}	Output from the matrix element discriminant.	–	$\text{SR}_1^{\geq 6j}$

Table A.2.: The input variables for the classification BDT of the ATLAS $t\bar{t}(H \rightarrow b\bar{b})$ search in the single lepton channel [69].

A. Appendix

Variable	Explanation	Region		
		SR ₁	SR ₂	SR ₃
	General variables			
m_{bb}^{\min}	Minimum invariant mass of pair of b -tagged jets.	✓	✓	—
m_{bb}^{\max}	Maximum invariant mass of pair of b -tagged jets.	—	—	✓
$m_{bb}^{\min \Delta R}$	Invariant mass of b -jet pair with minimum ΔR .	✓	—	✓
$m_{jj}^{\max p_T}$	Invariant mass of jet pair with maximum p_T .	✓	—	—
$m_{bb}^{\max p_T}$	Invariant mass of b -jet pair with maximum p_T .	✓	—	✓
$\Delta\eta_{bb}^{\text{avg}}$	Average over $\Delta\eta$ of all pairs of b -tagged jets.	✓	✓	✓
$\Delta\eta_{lj}^{\max}$	Maximum $\Delta\eta$ between any lepton and jets.	—	✓	✓
$\Delta R_{bb}^{\max p_T}$	ΔR of b -jet pair with maximum p_T .	—	✓	✓
$N_{bb}^{\text{Higgs } 30}$	Number of b -jet pairs with $ m_{bb} - m_H < 30$ GeV.	✓	✓	—
$N_{\text{jets}}^{p_T > 40}$	Number of jets with $p_T > 40$ GeV.	—	✓	✓
Aplanarity	Same as in Table A.2, but built from b -jets only.	—	✓	—
H_T^{all}	Scalar sum over all p_T .	—	—	✓
	Reconstruction BDT variables			
BDT score	Output from the reconstruction BDT.	✓**	✓**	✓
$m(b_H^1, b_H^2)$	Invariant mass of the b -jets from the Higgs candidate.	✓	—	✓
$\Delta R(H, t\bar{t})$	ΔR between the Higgs candidate and the $t\bar{t}$ system.	✓*	—	—
$\Delta R(H, l)^{\min}$	Minimum ΔR between Higgs candidate and a lepton.	✓	✓	✓
$\Delta R(H, b)^{\min}$	Minimum ΔR between Higgs candidate and a b -jet.	✓	✓	—
$\Delta R(H, b)^{\max}$	Maximum ΔR between Higgs candidate and a b -jet.	—	✓	—
$\Delta R(b_H^1, b_H^2)$	ΔR between the b -jets from the Higgs candidate.	—	✓	—
	B -tagging related variables			
$w_{b\text{-tag}}^{\text{Higgs}}$	Sum of b -tagging discriminants (from b_H^1 and b_H^2).	—	✓	—

Table A.3.: The input variables for the classification BDT of the ATLAS $t\bar{t}(H \rightarrow b\bar{b})$ search in the dilepton channel [69].

Variable	Explanation	Region	
		SR _{1,2} ^{5j}	SR _{1,2,3} ^{≥6j}
	General variables		
Centrality	Scalar sum over all particles p_T divided by sum over energy.	—	—
$p_T^{\text{jet } 5}$	5 th highest jet p_T .	—	—
$m_{bj}^{\max p_T}$	Invariant mass of b -jet, jet pair with maximum p_T .	—	—
$H_T^{t\bar{t}H}$	Scalar sum over t, \bar{t} and H p_T .	—	—

Table A.4.: Additional single lepton input variables, currently not used in the ATLAS $t\bar{t}(H \rightarrow b\bar{b})$ classification BDT.

A.3. Input Variables to the Optimised BDTs

In Table A.5, the input variables for the optimised classification BDT in the regions $\text{SR}_1^{5j} + \text{SR}_1^{\geq 6j} + \text{SR}_2^{\geq 6j}$ are presented. The shown ranking is obtained by the optimisation procedure, as described in Chapter 5.1.4. An explanation of the respective variables is either given in the Table A.2, Table A.4 or, in case of certain angular variables, in Chapter 5.1.

Single lepton channel ($\text{SR}_1^{5j}, \text{SR}_1^{\geq 6j}, \text{SR}_2^{\geq 6j}$)

Ranking	Variable	Region
		$\text{SR}_1^{5j} + \text{SR}_{1,2}^{\geq 6j}$
1	LHD	✓
2	$\Delta R_{bb}^{\text{avg}}$	✓
3	$m_{bb}^{\text{min } \Delta R}$	✓
4	BDT score	✓*
5	Centrality	✓
6	H_1	✓
7	B_{jet}^4	✓
8	$p_T^{\text{jet } 5}$	✓
9	$\Delta R(b_H^1, b_H^2)$	✓*
10	$m(b_H^1, b_H^2)$	✓
11	$m_{bj}^{\text{max } p_T}$	✓
12	$\Delta\eta(l, b_H^1)$	✓
13	$H_T^{t\bar{t}H}$	✓*
14	$\cos(\theta_{l,H})$	✓*
15	$\Delta\eta(l, b_H^2)$	✓*
16	$\Delta\eta(b_{\text{lep}}, b_H^1)$	✓*
17	$\Delta R((t, \bar{t})^{\text{min } \Delta R(H)}, H)$	✓
18	$\cos(\theta_H^{t_{\text{lep}}H}) \cos(\theta_l^H)$ (db)	✓*
19	$m_{jj}^{\text{min } \Delta R}$	✓
20	$\Delta R_{bb}^{\text{max } p_T}$	✓
21	H_T^{had}	✓
22	B_{jet}^5	✓

Table A.5.: The input variables for the optimised classification BDT in the single lepton channel, considering the regions $\text{SR}_1^{5j}, \text{SR}_1^{\geq 6j}, \text{SR}_2^{\geq 6j}$.

A. Appendix

Single lepton channel ($\text{SR}_1^{5j}, \text{SR}_1^{\geq 6j}, \text{SR}_2^{\geq 6j}$) within (BR_1, BR_2)

In Table A.6, the input variables for an enhanced classification BDT in the regions $\text{SR}_1^{5j} + \text{SR}_1^{\geq 6j} + \text{SR}_2^{\geq 6j}$ are presented. Events are required to be in BR_1 or BR_2 . As described in Chapter 5.1.4, the variables are obtained directly from the respective TMVA ranking without further optimisation. An explanation of the respective variables is either given in the Table A.2 or Table A.4 or, in case of certain angular variables, in Chapter 5.1.

Variable	Region
	$\text{SR}_1^{5j} + \text{SR}_{1,2}^{\geq 6j}$ within $\text{BR}_1 + \text{BR}_2$
LHD	✓
$m(b_H^1, b_H^2)$	✓
$\Delta R_{bb}^{\text{avg}}$	✓
$N_{bb}^{\text{Higgs } 30}$	✓
$m_{bb}^{\min \Delta R}$	✓
$\Delta R_{bb}^{\max p_T}$	✓
$\Delta R((t, \bar{t})^{\min \Delta R(H)}, H)$	✓
$\Delta \eta_{jj}^{\max}$	✓
$\Delta R((t, \bar{t})^{\min \Delta R(H)}, b_H^1)$	✓
$\Delta \eta(b(t_{\text{lep}}), b_H^1)$	✓**
$\Delta \eta(b(t_{\text{lep}}), H)$	✓*
$\Delta \eta(l, b_H^1)$	✓
$\Delta R((b(t_{\text{lep}}), b(t_{\text{had}}))^{\min \Delta R(H)}, b_H^1)$	✓
$\Delta \eta((b(t_{\text{lep}}), b(t_{\text{had}}))^{\min \Delta R(H)}, b_H^1)$	✓
$\Delta \eta(b_H^1, b_H^2)$	✓
$\Delta \eta((b(t_{\text{lep}}), b(t_{\text{had}}))^{\min \Delta R(H)}, H)$	✓
$\Delta \eta(t_{\text{lep}}, b_H^1)$	✓
$m(H, b(t_{\text{lep}}))$	✓
BDT score	✓*
$\Delta \eta(t_{\text{lep}}, H)$	✓*
$\Delta R((W_{\text{lep}}, W_{\text{had}})^{\min \Delta R(H)}, H)$	✓

Table A.6.: The input variables for an enhanced classification BDT in the single lepton channel, considering the regions $\text{SR}_1^{5j}, \text{SR}_1^{\geq 6j}, \text{SR}_2^{\geq 6j}$ and requiring the events to be within BR_1 or BR_2 .

Dilepton channel ($\mathbf{SR}_1^{\geq 4j}, \mathbf{SR}_2^{\geq 4j}, \mathbf{SR}_3^{\geq 4j}$)

In Table A.7, the input variables for the optimised classification BDT in the regions $\mathbf{SR}_1^{\geq 4j} + \mathbf{SR}_2^{\geq 4j} + \mathbf{SR}_3^{\geq 4j}$ are presented. The shown ranking is obtained by the optimisation procedure, as described in Chapter 5.2.4. An explanation of the respective variables is given in Table A.3 or, in case of certain angular variables, in Chapter 5.2

Ranking	Variable	Region
		$\mathbf{SR}_{1,2,3}^{\geq 4j}$
1	$\Delta\eta_{bb}^{\text{avg}}$	✓
2	BDT score	✓*
3	$w_{b\text{-tag}}^{\text{Higgs}}$	✓
4	$m_{bb}^{\min \Delta R}$	✓
5	$\Delta R_{bb}^{\max p_T}$	✓
6	m_{bb}^{\min}	✓
7	$\cos(\theta_{b_H^1, b_H^2})$	✓*
8	$\cos(\theta((t, \bar{t})^{\min \Delta R(H)}, H))$	✓
9	$\cos(\theta_{t, \bar{t}})$	✓*
10	$\Delta\eta(l_t, b_H^1)$	✓*
11	H_T^{all}	✓
12	$\Delta\eta(l_t, l_{\bar{t}})$	✓
13	$\Delta R(H, t\bar{t})$	✓
14	$\Delta R(b_H^1, b_H^2)$	✓
15	$m(b_H^1, b_H^2)$	✓
16	$\Delta\eta_{l_j}^{\max}$	✓
17	$\Delta R(t, b_t)$	✓*
18	$\Delta R((b_t, b_{\bar{t}})^{\min \Delta R(H)}, b_H^2)$	✓
19	$\cos(\theta((l_t, l_{\bar{t}})^{\min \Delta R(H)}, H))$	✓
20	$\Delta\eta((l_t, l_{\bar{t}})^{\min \Delta R(H)}, b_H^1)$	✓
21	$m_{bb}^{\max p_T}$	✓

Table A.7.: The input variables for the optimised classification BDT in the dilepton channel, considering the regions $\mathbf{SR}_1^{\geq 4j}, \mathbf{SR}_2^{\geq 4j}, \mathbf{SR}_3^{\geq 4j}$.

Dilepton channel with ν -weighting ($\text{SR}_1^{\geq 4j}, \text{SR}_3^{\geq 4j}$)

In Table A.8, the input variables for an enhanced classification BDT in the regions $\text{SR}_1^{\geq 4j} + \text{SR}_3^{\geq 4j}$ are presented. Events are reconstructed using ν -weighting. As described in Chapter 5.2.4, the variables are obtained directly from the respective TMVA ranking without further optimisation. An explanation of the respective variables is given in Table A.3 or, in case of certain angular variables, in Chapter 5.2.

Variable	Region
	$\text{SR}_1^{\geq 4j}, \text{SR}_3^{\geq 4j}$ with ν -weighting
$\Delta\eta_{bb}^{\text{avg}}$	✓
BDT score	✓*
$w_{b\text{-tag}}^{\text{Higgs}}$	✓
$\cos(\theta_{b_H^1, b_H^2})$	✓*
$\Delta\eta((l_t, l_{\bar{t}})^{\min \Delta R(H)}, b_H^1)$	✓
$m_{bb}^{\min \Delta R}$	✓
$m_{jj}^{\max p_T}$	✓
m_{bb}^{\min}	✓
$\Delta\eta(l_t, H)$	✓*
$\Delta R((l_t, l_{\bar{t}})^{\min \Delta R(H)}, H)$	✓
$\Delta R((b_t, b_{\bar{t}})^{\min \Delta R(H)}, b_H^2)$	✓
$\Delta\eta((b_t, b_{\bar{t}})^{\min \Delta R(H)}, b_H^2)$	✓
$\Omega_t^{t\bar{t}}$	✓*
$\cos(\theta_{t, b_H^2})$	✓*
$\Delta R(H, t\bar{t})$	✓
φ_{CP}^*	✓*
$\Omega_{b_H^1}$	✓*
$\Delta\eta_{lj}^{\max}$	✓
$\Delta R(b_H^1, b_H^2)$	✓*
$m(b_H^1, b_H^2)$	✓
$\Delta\eta(l_t, l_{\bar{t}})$	✓

Table A.8.: The input variables for an enhanced classification BDT in the dilepton channel, reconstructed with ν -weighting and considering the regions $\text{SR}_1^{\geq 4j}, \text{SR}_3^{\geq 4j}$.

A.4. Input Variables to the CP Determination BDTs

In Table A.9, the input variables for the dilepton and single lepton CP determination BDTs on MC generator particle level are presented. In the case of the dilepton (single lepton) observables, an explanation of the respective variables is either given in the Table A.3 (Table A.2 or Table A.4) or, in case of certain angular variables, in Chapter 5.2 (5.1).

BDT	Dilepton channel	Lepton + jets channel
1	$\Delta\eta(t, \bar{t})$	$\Delta\eta(t_{\text{lep}}, t_{\text{had}})$
2	$\Delta R(H, t\bar{t})$	H_T^{jets}
3	H_T^{all}	$\Delta R(H, t\bar{t})$
4	$\Delta\eta(l_t, l_{\bar{t}})$	$\Omega_{t_{\text{lep}}}^{t\bar{t}}$
5	$\Omega_t^{t\bar{t}}$	$\Delta R_{bb}^{\text{avg}}$
6	$\Delta R(l_t, l_{\bar{t}})$	$\Delta\eta(t_{\text{lep}}, b(t_{\text{had}}))$
7	$\Delta\eta_{bb}^{\text{avg}}$	$\Delta R(b_H^1, b_H^2)$
8	$\Delta R(t, \bar{t})$	$\Delta\eta(W_{\text{lep}}, W_{\text{had}})$
9	$\Delta\eta(l_t, H)$	Centrality
10	$\Delta R(H, l)^{\text{min}}$	$\cos(\theta_H^{t_{\text{lep}}H}) \cos(\theta_l^H)$ (db)
11	$\Delta R(b_H^1, b_H^2)$	$\Delta R(t_{\text{lep}}, H)$
12	$\Delta R(t, l_t)$	$\Delta R(b_H^1, H)$
13	$\cos(\theta_{t, l_t})$	$\sin(\theta_H^{t\bar{t}H}) \sin(\theta_{t_{\text{had}}}^{t\bar{t}})$ (db)
14	$\cos(\theta_H^{tH}) \cos(\theta_{l_t}^H)$ (db)	$\Delta\eta(l, W_{\text{had}})$
15	$\sin(\theta_H^{t\bar{t}H}) \sin(\theta_{\bar{t}}^{t\bar{t}})$ (db)	$\Delta R(t_{\text{lep}}, W_{\text{lep}})$
16	$\Delta\eta(t, l_t)$	$m(b_H^1, b_H^2)$
17	$\Delta R(t, H)$	b_4
18	$\sin(\theta_{\bar{t}}^{t\bar{t}H}) \sin(\theta_{b_H^1}^H)$ (sb)	$\Delta R(t_{\text{lep}}, t_{\text{had}})$
19	$N_{\text{jets}}^{p_T > 40}$	$p_T^{\text{jet } 5}$
20	b_4	$\Delta R(b(t_{\text{lep}}), H)$

Table A.9.: The input variables for the CP determination BDTs in the dilepton and in the single lepton channel.

Bibliography

- [1] S. L. Glashow, *Partial-symmetries of weak interactions*, Nucl. Phys. **22**, 579 (1961)
- [2] S. Weinberg, *A Model of Leptons*, Phys. Rev. Lett. **19**, 1264 (1967)
- [3] A. Salam, *Weak and Electromagnetic Interactions*, in N. Svartholm, editor, *Elementary particle theory*, pages 367–377, Almquist & Wiksell (1968)
- [4] H. Fritzsche, M. Gell-Mann, H. Leutwyler, *Advantages of the color octet gluon picture*, Phys. Lett. **B47(4)**, 365 (1973)
- [5] ATLAS Collaboration, *Observation of a new particle in the search for the Standard Model Higgs boson with the ATLAS detector at the LHC*, Phys. Lett. **B716(1)**, 1 (2012)
- [6] CMS Collaboration, *Observation of a new boson at a mass of 125 GeV with the CMS experiment at the LHC*, Phys. Lett. **B716(1)**, 30 (2012)
- [7] ATLAS Collaboration, *Evidence for the spin-0 nature of the Higgs boson using ATLAS data*, Phys. Lett. **B726**, 120 (2013)
- [8] S. Berge, W. Bernreuther, S. Kirchner, *Determination of the Higgs CP-mixing angle in the tau decay channels at the LHC including the Drell-Yan background*, Eur. Phys. J. **C74(11)**, 3164 (2014)
- [9] DØ Collaboration, *Observation of the Top Quark*, Phys. Rev. Lett. **74**, 2632 (1995)
- [10] CDF Collaboration, *Observation of top quark production in $\bar{p}p$ collisions*, Phys. Rev. Lett. **74**, 2626 (1995)
- [11] DONUT Collaboration, *Observation of tau neutrino interactions*, Phys. Lett. **B504**, 218 (2001)
- [12] R. S. Huerfano, M. Khovanov, *A Category for the Adjoint Representation*, J. Alg. **246(2)**, 514 (2001)

Bibliography

- [13] M. Kobayashi, T. Maskawa, *CP-Violation in the Renormalizable Theory of Weak Interaction*, Prog. Theor. Phys. **49(2)**, 652 (1973)
- [14] C. Patrignani, et al. (Particle Data Group), *Review of Particle Physics*, Chin. Phys. **C40(10)**, 100001 (2016)
- [15] S. L. Glashow, J. Iliopoulos, L. Maiani, *Weak Interactions with Lepton-Hadron Symmetry*, Phys. Rev. **D2**, 1285 (1970)
- [16] C. S. Wu, et al., *Experimental Test of Parity Conservation in Beta Decay*, Phys. Rev. **105**, 1413 (1957)
- [17] UA1 Collaboration, *Experimental Observation of Isolated Large Transverse Energy Electrons with Associated Missing Energy at $\sqrt{s} = 540$ GeV*, Phys. Lett. **B122(1)**, 103 (1983)
- [18] UA2 Collaboration, *Observation of Single Isolated Electrons of High Transverse Momentum in Events with Missing Transverse Energy at the CERN $\bar{p}p$ Collider*, Phys. Lett. **B122(5)**, 476 (1983)
- [19] UA1 Collaboration, *Experimental Observation of Lepton Pairs of Invariant Mass Around 95 GeV/c² at the CERN SPS Collider*, Phys. Lett. **B126(5)**, 398 (1983)
- [20] UA2 Collaboration, *Evidence for $Z^0 \rightarrow e^+e^-$ at the CERN $\bar{p}p$ Collider*, Phys. Lett. **B129(1)**, 130 (1983)
- [21] F. Englert, R. Brout, *Broken Symmetry and the Mass of Gauge Vector Mesons*, Phys. Rev. Lett. **13**, 321 (1964)
- [22] P. W. Higgs, *Broken Symmetries and the Masses of Gauge Bosons*, Phys. Rev. Lett. **13**, 508 (1964)
- [23] P. Minkowski, *$\mu \rightarrow e\gamma$ at a Rate of One Out of 10^9 Muon Decays?*, Phys. Lett. **B67**, 421 (1977)
- [24] M. Gell-Mann, P. Ramond, R. Slansky, *Complex Spinors and Unified Theories*, Conf. Proc. **C790927**, 315 (1979)
- [25] R. N. Mohapatra, G. Senjanovic, *Neutrino Mass and Spontaneous Parity Violation*, Phys. Rev. Lett. **44**, 912 (1980)
- [26] T. Yanagida, *Horizontal Symmetry and Masses of Neutrinos*, Prog. Theor. Phys. **64**, 1103 (1980)

- [27] J. Schechter, J. W. F. Valle, *Neutrino Masses in $SU(2) \times U(1)$ Theories*, Phys. Rev. **D22**, 2227 (1980)
- [28] J. Schechter, J. W. F. Valle, *Neutrino Decay and Spontaneous Violation of Lepton Number*, Phys. Rev. **D25**, 774 (1982)
- [29] J. H. Christenson, J. W. Cronin, V. L. Fitch, R. Turlay, *Evidence for the 2π Decay of the K_2^0 Meson*, Phys. Rev. Lett. **13**, 138 (1964)
- [30] S. W. Herb, et al., *Observation of a Dimuon Resonance at 9.5-GeV in 400-GeV Proton-Nucleus Collisions*, Phys. Rev. Lett. **39**, 252 (1977)
- [31] M. Czakon, A. Mitov, *Top++: A Program for the Calculation of the Top-Pair Cross-Section at Hadron Colliders*, Comput. Phys. Commun. **185**, 2930 (2014)
- [32] C. S. Li, R. J. Oakes, T. C. Yuan, *QCD corrections to $t \rightarrow W^+ + b$* , Phys. Rev. **D43**, 3759 (1991)
- [33] Y. Grossman, I. Nachshon, *Hadronization, spin and lifetimes*, JHEP **2008(07)**, 016 (2008)
- [34] G. Mahlon, S. J. Parke, *Spin correlation effects in top quark pair production at the LHC*, Phys. Rev. **D81**, 074024 (2010)
- [35] ATLAS Collaboration, *Analysis of the Wtb vertex from the measurement of triple-differential angular decay rates of single top quarks produced in the t -channel at $\sqrt{s} = 8$ TeV with the ATLAS detector*, JHEP **12**, 017 (2017)
- [36] ATLAS Collaboration, *Probing the Wtb vertex structure in t -channel single-top-quark production and decay in pp collisions at $\sqrt{s} = 8$ TeV with the ATLAS detector*, JHEP **04**, 124 (2017)
- [37] CDF Collaboration, *First Observation of Electroweak Single Top Quark Production*, Phys. Rev. Lett. **103**, 092002 (2009)
- [38] DØ Collaboration, *Observation of Single Top Quark Production*, Phys. Rev. Lett. **103**, 092001 (2009)
- [39] CDF Collaboration, *Observation of Single Top Quark Production and Measurement of $|V_{tb}|$ with CDF*, Phys. Rev. **D82**, 112005 (2010)
- [40] DØ Collaboration, *Measurement of the Top Quark Mass Using Dilepton Events*, Phys. Rev. Lett. **80**, 2063 (1998)

Bibliography

- [41] J. Erdmann, et al., *A likelihood-based reconstruction algorithm for top-quark pairs and the KLFitter framework*, Nucl. Instrum. Meth. **A748**, 18 (2014)
- [42] W. Bernreuther, et al., *Top quark pair production and decay at hadron colliders*, Nucl. Phys. **B690**, 81 (2004)
- [43] W. Bernreuther, et al., *Top-Quark Spin Correlations at Hadron Colliders: Predictions at Next-to-Leading Order QCD*, Phys. Rev. Lett. **87**, 242002 (2001)
- [44] W. Bernreuther, Z.-G. Si, *Distributions and correlations for top quark pair production and decay at the Tevatron and LHC.*, Nucl. Phys. **B837**, 90 (2010)
- [45] DØ Collaboration, *Evidence for spin correlation in $t\bar{t}$ production*, Phys. Rev. Lett. **108**, 032004 (2012)
- [46] CDF Collaboration, *Measurement of $t\bar{t}$ Spin Correlation in $p\bar{p}$ Collisions Using the CDF II Detector at the Tevatron*, Phys. Rev. **D83**, 031104 (2011)
- [47] ATLAS Collaboration, *Observation of spin correlation in $t\bar{t}$ events from pp collisions at $\sqrt{s} = 7$ TeV using the ATLAS detector*, Phys. Rev. Lett. **108**, 212001 (2012)
- [48] CMS Collaboration, *Measurements of $t\bar{t}$ spin correlations and top-quark polarization using dilepton final states in pp collisions at $\sqrt{s} = 7$ TeV*, Phys. Rev. Lett. **112(18)**, 182001 (2014)
- [49] S. Hannestad, *Dark energy and dark matter from cosmological observations*, Int. J. Mod. Phys. **A21**, 1938 (2006)
- [50] S. D. Bass, *Vacuum energy and the cosmological constant*, Mod. Phys. Lett. **A30**, 1540033-321 (2015)
- [51] Y. Fukuda, et al., *Evidence for Oscillation of Atmospheric Neutrinos*, Phys. Rev. Lett. **81**, 1562 (1998)
- [52] M. H. Ahn, et al., *Indications of Neutrino Oscillation in a 250 km Long-Baseline Experiment*, Phys. Rev. Lett. **90**, 041801 (2003)
- [53] KATRIN Collaboration, *The KATRIN Neutrino Mass Experiment*, Nucl. Instrum. Meth. **A623**, 442 (2010)
- [54] R. D. Peccei, *The Strong CP Problem and Axions*, in M. Kuster, G. Raffelt, B. Beltrán, editors, *Axions*, volume 741 of *Lecture Notes in Physics*, Berlin Springer Verlag, page 3 (2008)

- [55] J. Bordes, H.-M. Chan, S. T. Tsou, *A Solution to the Strong CP Problem Transforming the Theta Angle to the KM Cp-Violating Phase*, Int. J. Mod. Phys. **A25**, 5897 (2010)
- [56] ATLAS Collaboration, *Luminosity Determination in pp Collisions at $\sqrt{s} = 7$ TeV Using the ATLAS Detector at the LHC*, Eur. Phys. J. **C71**, 1630 (2011)
- [57] ATLAS Collaboration, *Luminosity determination in pp collisions at $\sqrt{s} = 8$ TeV using the ATLAS detector at the LHC*, Eur. Phys. J. **C76(12)**, 653 (2016)
- [58] F. Maltoni, D. L. Rainwater, S. Willenbrock, *Measuring the top quark Yukawa coupling at hadron colliders via $t\bar{t}H, H \rightarrow W^+W^-$* , Phys. Rev. **D66**, 034022 (2002)
- [59] A. Belyaev, L. Reina, *$pp \rightarrow t\bar{t}H, H \rightarrow \tau^+\tau^-$: Toward a model independent determination of the Higgs boson couplings at the LHC*, JHEP **08**, 041 (2002)
- [60] S. Dittmaier, et al. (LHC Higgs Cross Section Working Group), *Handbook of LHC Higgs Cross Sections: 1. Inclusive Observables* (2011)
- [61] ATLAS Collaboration, *Search for the Standard Model Higgs boson produced in association with top quarks and decaying into $b\bar{b}$ in pp collisions at $\sqrt{s} = 8$ TeV with the ATLAS detector*, Eur. Phys. J. **C75(7)**, 349 (2015)
- [62] ATLAS Collaboration, *Search for $H \rightarrow \gamma\gamma$ Produced in Association with Top Quarks and Constraints on the Yukawa Coupling between the Top Quark and the Higgs Boson using Data taken at 7 TeV and 8 TeV with the ATLAS Detector*, Phys. Lett. **B740**, 222 (2015)
- [63] CMS Collaboration, *Search for the standard model Higgs boson produced in association with a top-quark pair in pp collisions at the LHC*, JHEP **05**, 145 (2013)
- [64] CMS Collaboration, *Search for the associated production of the Higgs boson with a top-quark pair*, JHEP **09**, 087 (2014)
- [65] ATLAS Collaboration, *Evidence for the associated production of the Higgs boson and a top quark pair with the ATLAS detector*, Phys. Rev. **D97(7)**, 072003 (2018)
- [66] ATLAS Collaboration, *Observation of Higgs boson production in association with a top quark pair at the LHC with the ATLAS detector*, Phys. Lett. **B784**, 173 (2018)
- [67] CMS Collaboration, *Observation of $t\bar{t}H$ production*, Phys. Rev. Lett. **120(23)**, 231801 (2018)

Bibliography

- [68] ATLAS Collaboration, *Search for the Standard Model Higgs boson decaying into $b\bar{b}$ produced in association with top quarks decaying hadronically in pp collisions at $\sqrt{s} = 8$ TeV with the ATLAS detector*, JHEP **05**, 160 (2016)
- [69] ATLAS Collaboration, *Search for the standard model Higgs boson produced in association with top quarks and decaying into a $b\bar{b}$ pair in pp collisions at $\sqrt{s} = 13$ TeV with the ATLAS detector*, Phys. Rev. **D97(7)**, 072016 (2018)
- [70] ATLAS Collaboration, *Electron reconstruction and identification efficiency measurements with the ATLAS detector using the 2011 LHC proton-proton collision data*, Eur. Phys. J. **C74(7)**, 2941 (2014)
- [71] ATLAS Collaboration, *Electron efficiency measurements with the ATLAS detector using the 2015 LHC proton-proton collision data*, ATLAS-CONF-2016-024 (2016)
- [72] ATLAS Collaboration, *Muon reconstruction performance of the ATLAS detector in proton-proton collision data at $\sqrt{s} = 13$ TeV*, Eur. Phys. J. **C76(5)**, 292 (2016)
- [73] ATLAS Collaboration, *Reconstruction, Energy Calibration, and Identification of Hadronically Decaying Tau Leptons in the ATLAS Experiment for Run-2 of the LHC*, ATL-PHYS-PUB-2015-045 (2015)
- [74] ATLAS Collaboration, *Topological cell clustering in the ATLAS calorimeters and its performance in LHC Run 1*, Eur. Phys. J. **C77**, 490 (2017)
- [75] M. Cacciari, G. P. Salam, G. Soyez, *FastJet User Manual*, Eur. Phys. J. **C72**, 1896 (2012)
- [76] M. Cacciari, G. P. Salam, G. Soyez, *The Anti- $k(t)$ jet clustering algorithm*, JHEP **04**, 063 (2008)
- [77] ATLAS Collaboration, *Jet energy scale measurements and their systematic uncertainties in proton-proton collisions at $\sqrt{s} = 13$ TeV with the ATLAS detector*, Phys. Rev. **D96(7)**, 072002 (2017)
- [78] ATLAS Collaboration, *Selection of jets produced in 13TeV proton-proton collisions with the ATLAS detector*, ATLAS-CONF-2015-029 (2015)
- [79] ATLAS Collaboration, *Performance of pile-up mitigation techniques for jets in pp collisions at $\sqrt{s} = 8$ TeV using the ATLAS detector*, Eur. Phys. J. **C76(11)**, 581 (2016)

- [80] ATLAS Collaboration, *Performance of b-Jet Identification in the ATLAS Experiment*, JINST **11(04)**, P04008 (2016)
- [81] ATLAS Collaboration, *Optimisation of the ATLAS b-tagging performance for the 2016 LHC Run*, ATL-PHYS-PUB-2016-012 (2016)
- [82] B. Nachman, et al., *Jets from Jets: Re-clustering as a tool for large radius jet reconstruction and grooming at the LHC*, JHEP **02**, 075 (2015)
- [83] S. Biswas, et al., *Enhancing the $t\bar{t}H$ signal through top-quark spin polarization effects at the LHC*, JHEP **07**, 020 (2014)
- [84] ATLAS Collaboration, *Performance of missing transverse momentum reconstruction for the ATLAS detector in the first proton-proton collisions at $\sqrt{s}= 13$ TeV*, Technical Report ATL-PHYS-PUB-2015-027, CERN, Geneva (2015)
- [85] ATLAS Collaboration, *Performance of algorithms that reconstruct missing transverse momentum in $\sqrt{s} = 8$ TeV proton-proton collisions in the ATLAS detector*, Eur. Phys. J. **C77(4)**, 241 (2017)
- [86] ATLAS Collaboration, *The ATLAS Simulation Infrastructure*, Eur. Phys. J. **C70**, 823 (2010)
- [87] S. Agostinelli, et al. (GEANT4), *GEANT4: A Simulation toolkit*, Nucl. Instrum. Meth. **A506**, 250 (2003)
- [88] A. Djouadi, J. Kalinowski, M. Spira, *HDECAY: A Program for Higgs boson decays in the standard model and its supersymmetric extension*, Comput. Phys. Commun. **108**, 56 (1998)
- [89] D. de Florian, et al. (LHC Higgs Cross Section Working Group), *Handbook of LHC Higgs Cross Sections: 4. Deciphering the Nature of the Higgs Sector* (2016)
- [90] R. Raitio, W. W. Wada, *Higgs-boson production at large transverse momentum in quantum chromodynamics*, Phys. Rev. **D19**, 941 (1979)
- [91] W. Beenakker, et al., *NLO QCD corrections to t anti- t H production in hadron collisions*, Nucl. Phys. **B653**, 151 (2003)
- [92] S. Dawson, et al., *Associated Higgs production with top quarks at the large hadron collider: NLO QCD corrections*, Phys. Rev. **D68**, 034022 (2003)

Bibliography

- [93] Y. Zhang, et al., *QCD NLO and EW NLO corrections to $t\bar{t}H$ production with top quark decays at hadron collider*, Phys. Lett. **B738**, 1 (2014)
- [94] S. Frixione, et al., *Electroweak and QCD corrections to top-pair hadroproduction in association with heavy bosons*, JHEP **06**, 184 (2015)
- [95] P. Nason, *A New method for combining NLO QCD with shower Monte Carlo algorithms*, JHEP **11**, 040 (2004)
- [96] S. Frixione, P. Nason, C. Oleari, *Matching NLO QCD computations with Parton Shower simulations: the POWHEG method*, JHEP **11**, 070 (2007)
- [97] S. Alioli, et al., *A general framework for implementing NLO calculations in shower Monte Carlo programs: the POWHEG BOX*, JHEP **06**, 043 (2010)
- [98] J. M. Campbell, et al., *Top-Pair Production and Decay at NLO Matched with Parton Showers*, JHEP **04**, 114 (2015)
- [99] T. Sjöstrand, et al., *PYTHIA*, Comput. Phys. Commun. **135**, 238 (2001)
- [100] T. Sjöstrand, et al., *An Introduction to PYTHIA 8.2*, Comput. Phys. Commun. **191**, 159 (2015)
- [101] ATLAS Collaboration, *ATLAS Run 1 Pythia8 tunes*, Technical Report ATL-PHYS-PUB-2014-021, CERN, Geneva (2014)
- [102] R. D. Ball, et al. (NNPDF), *Parton distributions for the LHC Run II*, JHEP **04**, 040 (2015)
- [103] P. Artoisenet, et al., *Automatic spin-entangled decays of heavy resonances in Monte Carlo simulations*, JHEP **03**, 015 (2013)
- [104] D. J. Lange, *The EvtGen particle decay simulation package*, Nucl. Instrum. Meth. **A462**, 152 (2001)
- [105] J. Alwall, et al., *The automated computation of tree-level and next-to-leading order differential cross sections, and their matching to parton shower simulations*, JHEP **07**, 079 (2014)
- [106] J. Bellm, et al., *Herwig 7.0/Herwig++ 3.0 release note*, Eur. Phys. J. **C76(4)**, 196 (2016)

- [107] C. Degrande, et al., *UFO - The Universal FeynRules Output*, Comput. Phys. Commun. **183**, 1201 (2012)
- [108] F. Demartin, et al., *Higgs characterisation at NLO in QCD: CP properties of the top-quark Yukawa interaction*, Eur. Phys. J. **C74(9)**, 3065 (2014)
- [109] M. Cacciari, et al., *Top-pair production at hadron colliders with next-to-next-to-leading logarithmic soft-gluon resummation*, Phys. Lett. **B710**, 612 (2012)
- [110] M. Czakon, A. Mitov, *NNLO corrections to top-pair production at hadron colliders: the all-fermionic scattering channels*, JHEP **12**, 054 (2012)
- [111] M. Czakon, A. Mitov, *NNLO corrections to top pair production at hadron colliders: the quark-gluon reaction*, JHEP **01**, 080 (2013)
- [112] M. Czakon, P. Fiedler, A. Mitov, *Total Top-Quark Pair-Production Cross Section at Hadron Colliders Through $O(\hat{\Gamma} \pm \frac{4}{5})$* , Phys. Rev. Lett. **110**, 252004 (2013)
- [113] ATLAS Collaboration, *Studies on top-quark Monte Carlo modelling for Top2016*, ATL-PHYS-PUB-2016-020 (2016)
- [114] T. Gleisberg, et al., *Event generation with SHERPA 1.1*, JHEP **02**, 007 (2009)
- [115] F. Cascioli, P. Maierhofer, S. Pozzorini, *Scattering Amplitudes with Open Loops*, Phys. Rev. Lett. **108**, 111601 (2012)
- [116] H.-L. Lai, et al., *New parton distributions for collider physics*, Phys. Rev. **D82**, 074024 (2010)
- [117] T. Sjöstrand, S. Mrenna, P. Z. Skands, *PYTHIA 6.4 Physics and Manual*, JHEP **05**, 026 (2006)
- [118] A. Hoecker, et al., *TMVA: Toolkit for Multivariate Data Analysis*, PoS **ACAT**, 040 (2007)
- [119] R. Frederix, et al., *Scalar and pseudoscalar Higgs production in association with a top-antitop pair*, Phys. Lett. **B701**, 427 (2011)
- [120] A. Brandenburg, Z. G. Si, P. Uwer, *QCD corrected spin analyzing power of jets in decays of polarized top quarks*, Phys. Lett. **B539**, 235 (2002)
- [121] M. Jezabek, *Top quark physics*, Nucl. Phys. Proc. Suppl. **37B(2)**, 197 (1994)

Bibliography

- [122] M. Baumgart, B. Tweedie, *A New Twist on Top Quark Spin Correlations*, JHEP **03**, 117 (2013)
- [123] W. Bernreuther, et al., *Production of heavy Higgs bosons and decay into top quarks at the LHC. II: Top-quark polarization and spin correlation effects*, Phys. Rev. **D95(9)**, 095012 (2017)
- [124] S. P. Amor dos Santos, et al., *Angular distributions in $t\bar{t}H(H \rightarrow b\bar{b})$ reconstructed events at the LHC*, Phys. Rev. **D92(3)**, 034021 (2015)
- [125] D. Azevedo, et al., *CP tests of Higgs couplings in $t\bar{t}h$ semileptonic events at the LHC*, Phys. Rev. **D98(3)**, 033004 (2018)
- [126] S. Amor Dos Santos, et al., *Probing the CP nature of the Higgs coupling in $t\bar{t}h$ events at the LHC*, Phys. Rev. **D96(1)**, 013004 (2017)
- [127] J. F. Gunion, X.-G. He, *Determining the CP nature of a neutral Higgs boson at the LHC*, Phys. Rev. Lett. **76**, 4468 (1996)
- [128] F. Boudjema, et al., *Lab-frame observables for probing the top-Higgs interaction*, Phys. Rev. **D92(1)**, 015019 (2015)
- [129] D. Fontes, et al., *Large pseudoscalar Yukawa couplings in the complex 2HDM*, JHEP **06**, 060 (2015)
- [130] ATLAS Collaboration, *Study of the spin and parity of the Higgs boson in diboson decays with the ATLAS detector*, Eur. Phys. J. **C75(10)**, 476 (2015)
- [131] CMS Collaboration, *Constraints on the spin-parity and anomalous HVV couplings of the Higgs boson in proton collisions at 7 and 8 TeV*, Phys. Rev. **D92(1)**, 012004 (2015)
- [132] CMS Collaboration, *Combined search for anomalous pseudoscalar HVV couplings in $VH(H \rightarrow b\bar{b})$ production and $H \rightarrow VV$ decay*, Phys. Lett. **B759**, 672 (2016)
- [133] D. Fontes, et al., *The C2HDM revisited*, JHEP **02**, 073 (2018)
- [134] V. D. Barger, J. Ohnemus, R. J. N. Phillips, *Event shape criteria for single lepton top signals*, Phys. Rev. **D48**, R3953 (1993)
- [135] G. C. Fox, S. Wolfram, *Observables for the Analysis of Event Shapes in e^+e^- Annihilation and Other Processes*, Phys. Rev. Lett. **41**, 1581 (1978)

Acknowledgements

I would like to thank Prof. Dr. Arnulf Quadt for being the first referee of this thesis. He gave me the opportunity to write my Master's thesis in particle physics. I would like to thank Prof. Dr. Stan Lai for being the second referee. I would like to thank Dr. Clara Nellist for being my supervisor and for proofreading parts of this thesis.

I would like to expressly thank Dr. Thomas Peiffer for helpful discussions and for proofreading this thesis.

I would like to thank Dr. Andrea Knue for providing the MC samples with modified Yukawa couplings and I would like to thank Jannik Geisen for helping me with these samples.

Erklärung

nach §17(9) der Prüfungsordnung für den Bachelor-Studiengang Physik und den Master-Studiengang Physik an der Universität Göttingen:

Hiermit erkläre ich, dass ich diese Abschlussarbeit selbständig verfasst habe, keine anderen als die angegebenen Quellen und Hilfsmittel benutzt habe und alle Stellen, die wörtlich oder sinngemäß aus veröffentlichten Schriften entnommen wurden, als solche kenntlich gemacht habe.

Darüberhinaus erkläre ich, dass diese Abschlussarbeit nicht, auch nicht auszugsweise, im Rahmen einer nichtbestandenenen Prüfung an dieser oder einer anderen Hochschule eingereicht wurde.

Göttingen, den 25. März 2019

(Paul Konstantin Krug)